Icarus 287 (2017) 229–260

Contents lists available at ScienceDirect

Icarus

journal homepage: www.elsevier.com/locate/icarus

Physical state and distribution of materials at the surface of Pluto from New Horizons LEISA imaging spectrometer☆

B. Schmitt[a,*], S. Philippe[a], W.M. Grundy[b], D.C. Reuter[c], R. Côte[a], E. Quirico[a], S. Protopapa[d], L.A. Young[e], R.P. Binzel[f], J.C. Cook[e], D.P. Cruikshank[g], C.M. Dalle Ore[g], A.M. Earle[f], K. Ennico[g], C.J.A. Howett[e], D.E. Jennings[c], I.R. Linscott[h], A.W. Lunsford[c], C.B. Olkin[e], A.H. Parker[e], J.Wm. Parker[e], K.N. Singer[e], J.R. Spencer[e], J.A. Stansberry[i], S.A. Stern[e], C.C.C. Tsang[e], A.J. Verbiscer[j], H.A. Weaver[k], the New Horizons Science Team

[a] Université Grenoble Alpes, CNRS, IPAG, F-38000 Grenoble, France
[b] Lowell Observatory, Flagstaff, AZ 86001, USA
[c] NASA Goddard Space Flight Center, Greenbelt, MD 20771, USA
[d] Department of Astronomy, University of Maryland, College Park, MD 20742, USA
[e] Southwest Research Institute, Boulder, CO 80302, USA
[f] Massachusetts Institute of Technology, Cambridge, MA 02139, USA
[g] NASA Ames Research Center, Space Science Division, Moffett Field, CA 94035, USA
[h] Stanford University, Stanford CA 94305, USA
[i] Space Telescope Science Institute, Baltimore, MD 21218, USA
[j] Department of Astronomy, University of Virginia, Charlottesville, VA 22904, USA
[k] Johns Hopkins University Applied Physics Laboratory, Laurel, MD 20723, USA

ARTICLE INFO

Article history:
Received 15 May 2016
Revised 20 December 2016
Accepted 20 December 2016
Available online 24 December 2016

Keywords:
Pluto
Surface – ices
IR spectroscopy – infrared observations

ABSTRACT

From Earth based observations Pluto is known to be the host of N2, CH4 and CO ices and also a dark red material. Very limited spatial distribution information is available from rotational visible and near-infrared spectral curves obtained from hemispheric measurements. In July 2015 the New Horizons spacecraft reached Pluto and its satellite system and recorded a large set of data. The LEISA spectro-imager of the RALPH instruments are dedicated to the study of the composition and physical state of the materials composing the surface. In this paper we report a study of the distribution and physical state of the ices and non-ice materials on Pluto's illuminated surface and their mode and degree of mixing. Principal Component analysis as well as various specific spectral indicators and correlation plots are used on the first set of 2 high resolution spectro-images from the LEISA instrument covering the whole illuminated face of Pluto at the time of the New Horizons encounter. Qualitative distribution maps have been obtained for the 4 main condensed molecules, N2, CH4, CO, H2O as well as for the visible-dark red material. Based on specific spectral indicators, using either the strength or the position of absorption bands, these 4 molecules are found to indicate the presence of 3 different types of ices: N2-rich:CH4:CO ices, CH4-rich(:CO:N2?) ices and H2O ice. The mixing lines between these ices and with the dark red material are studied using scatter plots between the various spectral indicators. CH4 is mixed at the molecular level with N2, most probably also with CO, thus forming a ternary molecular mixture that follows its phase diagram with low solubility limits. The occurrence of a N2-rich – CH4-rich ices mixing line associated with a progressive decrease of the CO/CH4 ratio tells us that a fractionation sublimation sequence transforms one type of ice to the other forming either a N2-rich – CH4-rich binary mixture at the surface or an upper CH4-rich ice crust that may hide the N2-rich ice below. The strong CH4-rich – H2O mixing line witnesses the subsequent sublimation of the CH4-rich ice lag left behind by the N2:CO sublimation (N spring-summer), or a direct condensation of CH4 ice on the cold H2O ice (S autumn). The weak mixing line between CH4-containing ices and the dark red material and the very sharp spatial transitions between these ices and this non-volatile material are probably due to thermal incompatibility. Finally the

☆ All surface feature names mentioned in this paper are informal and are mapped in Moore et al. (2016).

* Corresponding author.
E-mail address: bernard.schmitt@univ-grenoble-alpes.fr (B. Schmitt).

http://dx.doi.org/10.1016/j.icarus.2016.12.025

occurrence of a H2O ice – red material mixing line advocates for a spatial mixing of the red material covering H2O ice, with possibly a small amount intimately mixed in water ice. From this analysis of the different materials distribution and their relative mixing lines, H2O ice appears to be the substratum on which other ices condense or non-volatile organic material is deposited from the atmosphere. N2-rich ices seem to evolve to CH4-dominated ices, possibly still containing traces of CO and N2, as N2 and CO sublimate away. The spatial distribution of these materials is very complex.

The high spatial definition of all these composition maps, as well as those at even higher resolution that will be soon available, will allow us to compare them with Pluto's geologic features observed by LORRI panchromatic and MVIC multispectral imagers to better understand the geophysical processes in action at the surface of this astonishingly active frozen world.

1. Introduction

Pluto is the largest Trans-Neptunian Object (TNO), located at the inner edge of the Kuiper disk. It is probably not a first generation TNO, and resulted from a giant impact between two older progenitors. This impact also may have formed its five satellites: Charon, Styx, Nix, Kerberos and Hydra (Stern et al., 2006). Pluto has a differentiated structure with a refractory core and an icy mantle, and an active surface as well. The surface has complex interactions with its tenuous atmosphere controlled by climatic cycles. The composition of Pluto's surface is a major issue because it is the only way to infer its bulk composition. Its determination is however a challenging issue. The uppermost volatile layer deposited onto the water ice bedrock is heterogeneous and time-dependent, due to sublimation-condensation cycles controlled by the local and global seasonal evolution of illumination (see e.g. Spencer et al., 1997). Complicating the picture, secondary species are formed from simple volatile molecules. The atmosphere is the place of photochemical processes that form organic aerosols that eventually fall and settle into dark-red coatings on the surface. The surface is also chemically and physically processed by Galactic Cosmic Rays (Madey et al., 2002).

CH_4 was the first molecule detected on the surface of Pluto (Cruikshank et al., 1976), followed by CO and N_2 (Owen et al., 1993). These three molecules form a molecular mixture with variable geographic and stratigraphic abundances. Douté et al. (1999) found evidence for the presence of two methane phases: diluted methane (~0.5%) in solid nitrogen, along with 0.1–0.2% CO, coexisting with a CH_4-rich phase that contains small amounts of diluted N_2 and CO. These phases are distributed as segregated patches across the surface or as a segregated layer on top of the CH_4-poor phase, or a combination of both (Douté et al., 1999; Olkin et al., 2007; Merlin et al., 2010; Merlin, 2015). Interestingly, the CH_4-poor phase predominates at the surface of Triton (Quirico et al., 1999) while on other large KBOs (e.g. Makemake, Eris) large amounts of methane are detected, and spatially segregated as well (Licandro, 2006; Merlin et al., 2009; Guilbert et al., 2009; Alvarez-Candal, 2011).

Disk-integrated observations with increasing spectral resolution have continuously revealed new molecules. Water ice is known to be the bedrock on Triton (Cruikshank et al., 1993, 2000; Grundy et al., 2010) but it has eluded identification on Pluto up to New Horizons (Grundy and Buie, 2002) although its signature was indeed present in several ground based near-infrared observations, albeit as a faint spectral modulation between the strong CH4 bands (Philippe et al., 2015). Ethane (C_2H_6) which is one of the main byproducts resulting from methane photolysis, has been tentatively detected (Lara et al., 1997; Krasnopolsky and Cruikshank, 1999; Moore and Hudson, 2003). This identification is not firm because most of the absorption bands of ethane ice are located in spectral regions dominated by CH_4 absorption and the observed features are weak (Cruikshank et al., 1999; Sasaki et al., 2005; Cruikshank et al., 2006; DeMeo et al., 2010; Merlin et al., 2010; Holler et al., 2014). It should be noted that C_2H_6 has also been tentatively identified on the KBO 50,000 Quaoar (Dalle Ore et al., 2009; Barucci et al., 2015). Species expected to arise from N_2:CH_4 photochemistry, such as C_2H_2, C_4H_2, HC_3N and HCN, have not been detected. CO_2, which was firmly identified at the surface of Triton, has not been detected on Pluto (Cruikshank et al., 1993; Douté et al., 1999; Grundy and Buie, 2002; Grundy et al., 2013). The presence of non-icy components is inferred from a red visible slope and low-reflectance terrains. They have been so far interpreted as organic solids, because the red slope could be fitted with so-called Tholins that are polymeric hydrogenated carbon nitride used to simulate Titan's aerosols (see e.g. Cruikshank et al., 2015). This is however not a firm identification, as the red slope cannot be interpreted unequivocally and no signatures of those analogs have been detected in the near-infrared range. But their contribution to the spectra is probably indiscernible in hemispheric averaged spectra at near-infrared wavelengths.

Our knowledge about the spatial distribution of the materials on Pluto come from the visible and infrared spectral light curves as Pluto rotates in 6.4 days. The monitoring with sub-Earth longitude of the band strength of CH4, N2 and CO, as well as the position of the CH4 bands and the visible slope, allowed to mapping longitudinally these materials on Pluto. In particular the anti-Charon hemisphere shows the strongest CO and N2 absorptions, but intermediate strength and strongly shifted CH4 bands lead to the conclusion that more N2-rich ice with diluted CH4 and CO should be present (Grundy and Buie, 2001, 2002; Grundy et al., 2013; Lorenzi et al., 2016) where HST observed the bright patch (Buie et al., 1992) now known as *Sputnik Planitia* (All names are informal).

Deciphering potential secular changes appears tricky as Pluto's viewing geometry strongly changes with time due to the rapid evolution of Pluto's sub-Earth latitude (±60°). A static distribution of the ices with more CO and N2 in equatorial/tropical regions and concentration of CH4 at the northernmost latitudes may explain most of the spectral and photometric changes, but there are hints of secular changes, either in spatial distribution or in texture of the ices possibly triggered by ice differentiation upon sublimation (Grundy et al., 2013, 2014). A detailed comprehensive review of the knowledge of the composition of the surface of Pluto prior to New Horizons flyby can be found in Cruikshank et al. (2015).

In July 2015, the New Horizons spacecraft reached Pluto and its satellites and collected a large set of data. The Ralph instrument, comprising a visible-near-infrared camera (MVIC) and an imaging spectrometer (LEISA), was designed to characterize the composition and the physical state of the surface of Pluto. First results on the composition and distribution of ices from preliminary analysis of the Ralph instrument have been reported in Stern et al. (2015) and in Grundy et al. (2016). They mostly revealed a complex distribution of the volatile ices with CH4 widely distributed across planet's surface but with especially strong absorption bands at high northern latitudes (*Lowell Regio*) where N2 is absent, in

Tartarus Dorsa (east), at the fringes of the southern winter hemisphere, and particularly in *Sputnik Planitia* where the strongest N2 bands and only CO signatures are also found. On the other hand CH4 is particularly depleted in mountains west of *Sputnik Planitia* and in the low-albedo equatorial regions (*Cthulhu Regio* and *Krun Macula*), while it is patchy at northern mid-latitudes in relation with topography (crater rims, ridges …). In addition to *Sputnik Planitia*, a patchy distribution of N_2 absorption was also found at these northern mid-latitudes, but with a distribution distinct from CH_4.

While LEISA did not detected any exposed CO2 ice, H2O ice was discovered in several small area, in almost pure state in one place (vicinity of *Pulfrich Crater*), but with a distinctly red/orange color at most other places, corresponding to fossa (*Virgil Fossa* …) or valleys between individual mountain peaks (in *Viking Terra, Baré Montes, al-Idrisi, Hillary*, and *Zheng He Montes*, …). Some shallow H2O absorption has been also detected along most N, E and S sides of *Cthulhu Regio*, probably mixed with the dark red non-ice material that largely covers this area.

Following this work, the aim of this paper is to study in more detail the distribution and physical state of the ices and non-ice materials at the surface of Pluto, and in particular their mode and degree of mixing. For this a Principal Component analysis (PCA) as well as various specific spectral indicators have been calculated on the first set of 2 high resolution spectro-images from the LEISA instrument and covering the whole illuminated face of Pluton.

A companion papers in this issue is devoted to quantitative studies of the distribution of CH4:N2 ice abundance and texture (Protopapa et al., 2017) at the surface of Pluto.

2. Instrument and data

2.1. LEISA instrument

The LEISA component of the Ralph instrument is a wedged filter spectral imager fabricated by placing a narrow band near-IR filter directly over the 256×256 pixel HgCdTe near-IR detector array at the focal plane of the system (Reuter et al., 2008). The transmission band pass of this filter varies along the in-track direction, which is aligned with the rows on the array. The 1.25–2.5 μm spectrum of a target is obtained by scanning its image along the in-track dimension. To first order, the pixels in a given column of the array (the cross-track direction) are "seeing" different points of the target at the same wavelength. However, due to mis-alignment and compositional variability inherent in the filter deposition process, there is a spectral "smile" of 2–3 spectral elements along the 256 cross-track pixels. The spectral response of every pixel in the array has been measured, however for the initial results presented in this paper the average wavelength along a column has been used, meaning there may be offsets of 1–2 spectral resolution elements as a function of pixel position.

The spectral and radiometric response of each LEISA pixel was calibrated prior to launch. However, to account for a known position dependent scattering effect and possible response changes during the nearly 10 year cruise to the Pluto system, stellar radiometric calibration along-track scans were obtained during annual checkouts and other specified periods. The signal from the stellar scans being localized to only a few pixels around the target, an additional "flat-field" observation was carried out at the Pluto system. In this observation, the image of Pluto was scanned rapidly in the cross-track direction (i.e. 90° from the normal direction) so that each pixel in a column had nearly the same smeared view of the surface. After correction for the spectral smile, these scans, along with the stellar data, have been used to produce an updated radiometric calibration field that appears to be more accurate than the pre-launch data. This is somewhat of an ongoing process, because of observational noise and scattering, and improvements will probably be made as more spectral data from Pluto and Charon are downlinked and become available. The possible impact of calibration changes has been considered in the results presented here. The photometric calibration of the data analyzed in this paper used flat field version '3b'.

With this instrument configuration LEISA creates spectral maps in the 1.25–2.5 μm infrared spectral range where most of the molecular materials known or expected at the surface of Pluto have spectral signatures. The spectrometer has two segments: (1) 1.25–2.5 μm with an average spectral resolving power ($\lambda/\Delta\lambda$) of 240 and (2) 2.1–2.25 μm with average spectral resolving power of 560 (Reuter et al., 2008). Only the low resolution segment is used in this paper.

LEISA has a single pixel IFOV of $62 \times 62\,\mu rad^2$ and forms a spectral map by scanning the $0.91° \times 0.91°$ FOV across the scene while the spacecraft slowly rotates around the Z axis so as to sweep LEISA's field of view across the target scene in the wavelength dispersion direction. Images are recorded each time the scene has shifted by approximately one pixel on the focal plane. The coordination between frame rate and scan rate is not exact because the spacecraft attitude and motion is controlled by hydrazine thrusters. A thruster is fired automatically whenever the spacecraft's attitude drifts beyond a specified dead band limit, imparting an impulse that is brief compared with the interval between LEISA frames. During the run-up to a LEISA scan, the spacecraft is commanded to spin up to the intended scan rate, and then thrusters are inhibited from applying further corrections in the scan direction to minimize rate changes. But they still fire in the cross track direction if needed to keep the scan on target. These impulses impose a zigzag motion as the instrument pointing bounces back and forth within the cross-track dead band. This zigzag structure is visible in some images and data products with low S/N ratio (see e.g. Fig. 3.11, 7a and 11) due to remaining flat field artifacts. Although these corrections are predominantly perpendicular to the scan direction, they are not perfectly orthogonal to it, so they also cause small changes in the scan rate. During LEISA scans, spacecraft attitude is measured and recorded at a 1 Hz rate as part of the standard housekeeping data.

2.2. Data reduction

New Horizons scanned the LEISA imaging spectrometer across the planet several times on the closest approach date 2015 July 14. So far, two of the five highest spatial resolution scans have been calibrated, obtained from spacecraft slant distances of 112,045 km (#029,917,2014 at 9:33 UTC) and 99,856 km (#029,917,2889 at 9:48 UTC). The resulting sub-spacecraft spatial resolutions are 6.95 and 6.2 km/pixel, respectively. In combination, the two images cover the visible disk of Pluto and slightly overlap in the middle. The sub-solar latitude was 51.55° N and the sub-solar longitudes 133.16° and 132.57° E, respectively. The phase angle was 22.0° and 22.8°, respectively, at the sub-spacecraft point.

The spectra of each data cube were reconstructed using the Integrated Software for Imagers and Spectrometers (ISIS) software provided by the United States Geological Survey (USGS). It uses the spacecraft attitude history and reconstructed trajectory along with its LEISA camera model to determine where each LEISA pixel falls on Pluto. The two cubes were both projected to a common orthographic viewing geometry on a sphere of Pluto's size and at location relative to the spacecraft appropriate for the mid-time between the two scans. The re-projection was done to an oversampled target grid with a spatial scale of about 2 km/pixel at the center of the image, a higher resolution than the native LEISA pixel scales, in order to minimize degradation of spatial information as a result of the nearest neighbor re-sampling. Comparison of

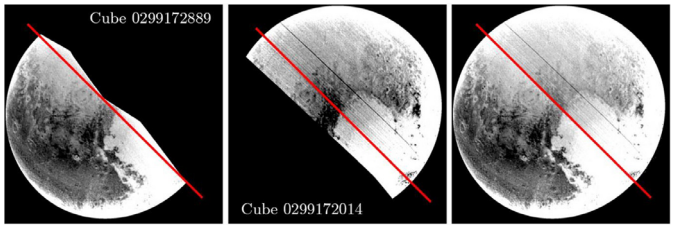

Fig. 1. Images at 2 μm of the two LEISA data cubes (same orthographic projection) and the final cube used in this study. The two LEISA images have been cut in their overlapping region along the red line in order to remove the part of the first cube with incomplete spectral coverage, to reduce the side areas with strongest spectral smile and to minimize the striped area. The final cube is obtained after both parts are glued' side-by-side'. (For interpretation of the references to colour in this figure legend, the reader is referred to the web version of this article.)

the LEISA cube with the much higher resolution LORRI base map projected to the same geometry showed mismatches between them (of the order of a few LEISA pixels), but consistently across LEISA wavelengths. Geometric corrections were then performed by globally shifting the LEISA data and "warping" them on the LORRI base map (Fig. 1) based on a control network constructed using features that were recognizable in both LEISA and LORRI data. These corrections resulted in LEISA cubes estimated to be geometrically accurate to a little better that a single LEISA pixel. The mid-time between the 2 scans was taken as a reasonable approximation of the illumination and viewing geometry for each pixel. Pluto's rotation at 6.4 days period and spacecraft motion along its trajectory at approximately 14 km/s relative to the Pluto system means that the geometry is not perfectly static over the course of the two LEISA scans, spanning about 26 min in total.

For this paper we cut the 2 images in their overlapping region along the same geographic line and glued them side-by-side without merging (Fig. 1). We choose this strategy to remove the parts with incomplete spectral coverage (relatively large on the right side of image #0299172889 which was acquired with several thrusters firings), to reduce as much as possible the areas with strongest spectral smile (slight wavelength shifts towards the edges of each scan, more pronounced in the lower left parts of both images) and edge effects in the currently available LEISA flat field. The spectral smile effect being asymmetric with a more pronounced spectral shift on the left side of the images we decided to remove the incomplete right part of the lower image and as much as possible of the left part of the upper image, also the most altered by striping. This line is clearly visible in some of our spectral indicators due to small remaining photometric and/or spatial calibration misfits along this line. As we will see all along our data analysis, although there are still remaining calibration and instrumental issues (photometric calibration, spectral calibration and smile, …), the quality of the data and the current state of calibration is already very good to perform statistical and spectral parameters analyses.

In order to remove the strong effect of solar incidence on the reflected radiance and keep only the intrinsic photometric properties of the surface materials, we converted the I/F radiance into reflectance factor (REFF, as defined by Hapke (2012)) by dividing by the cosine of the incidence angle on the reference ellipsoid of Pluto (currently a sphere). However this correction is at first order as it does not yet take into account the topography of the surface. Small projection or topographic errors in incidence angles may induce strong photometric effects in REFF close to the terminator (dark blue line in Fig. 2). The rotation of Pluto by about 1° from the start of recording of the first image to the end of the second can also induce deviations in incidence angle by up to ±1.5° relative to the average value considered.

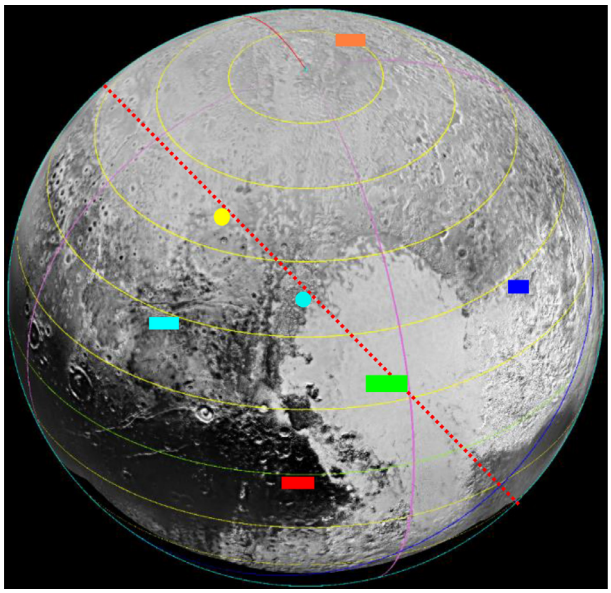

Fig. 2. LORRI base image (orthographic projection) on which the LEISA data are projected. The 2 LEISA images have been cut in their overlapping region and glued along the red dotted line. The main geodesic and observation geometry elements are added (Latitudes, every 15°: yellow (equator in green); longitudes: magenta (sub-Charon 0° is in red); limb: cyan; terminator: dark blue). 'Sol' is the sub-solar point, 'Spa' is the sub-spacecraft point at the mid-time of the two LEISA observations of this paper. The rectangular boxes are the location of the average spectra extracted in Fig. 4. (For interpretation of the references to colour in this figure legend, the reader is referred to the web version of this article.)

3. Data analysis

3.1. Preliminary exploration of the data with PCA analysis

In order to assess the spectral content of the data set and as a first try to separate the different chemical or physical components present on the surface and map their spatial distribution, we run a Principal Component Analysis with the ENVI© software (Jolliffe, 1986). We excluded the spectels #1, 2 and 198 (the last one) because they have strong photometric calibration caveats. We also excluded all pixels with incidence angles larger than 85° as the reflected signal is noisier in this weakly illuminated and strongly shadowed area and the uncertainty on the incidence angle has strong effects on REFF photometry at these grazing angles.

The result of this analysis is 9 Principal Components containing significant physical information and accounting for 94.1% of the variance. The first PC dominated by noise and instrumental effects is PC#6 where 93.6% of the variance is already accounted for, which assesses the high quality of the data, even at the current stage of the data calibration. This will be further demonstrated in the paper. The first 12 Principal Components are shown in Fig. 3. The most striking point is the sharp spatial definition of the first 5 PC axes. They contain information with high spatial contrast. The other physically meaningful PC axes (#7, #8, #10 and #12) contain more subtle or more localized spectral information and are partly contaminated by noise and instrumental effects, especially in the central part of the image along the line (clearly seen in PC#1) where the 2 observations are glued. Striping along the along-track direction (SE-NW) is also evidenced from PC#4 and above, more markedly in the upper right part of the maps. PC#6 and #9 have even more subtle information mixed with instrumental effects. PC#11 and all PC above #12 contain mostly noise and instrumental effects. However PC axes are not physically meaningful *per se* and need to be correlated to specific spectral indicators to understand

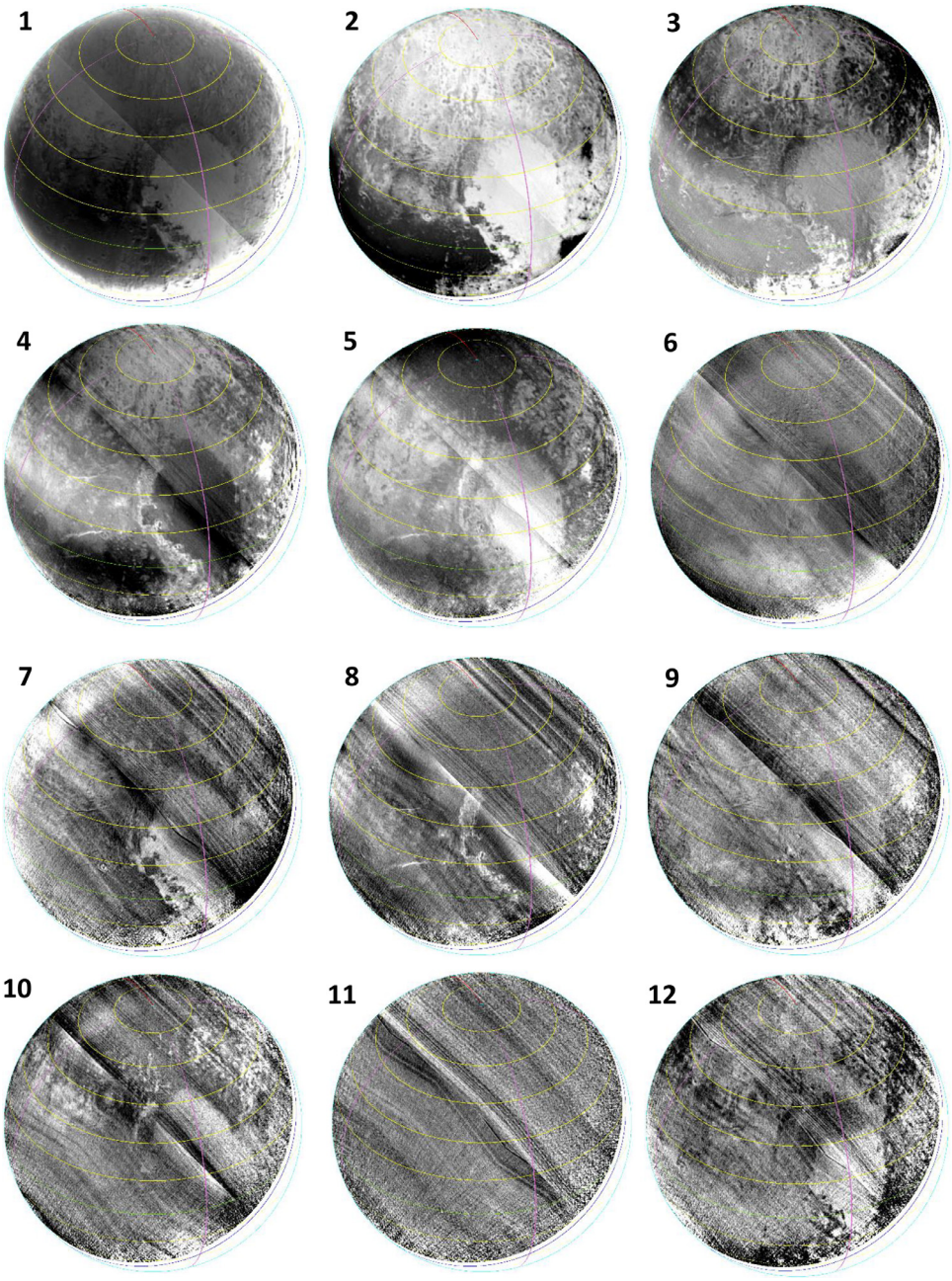

Fig. 3. The 12 first Principal Component axes (PC) of the PCA of the LEISA REFF spectro-image, in order of decreasing weight. PC#6, #9, #11 and above #12 are dominated by noise and instrumental effects, but subtle physical information is still discernible in the first two.

to which physical parameter each PC is the proxy: specific species or material, physical state, photometric parameter… However they are frequently the mix of several variable parameters and fail to separate weak and localized features, but strongly help to pinpoint some hidden variability in the data, to localize end-members and to define more efficient spectral indicators.

The combined spectro-image of the whole illuminated disk displays large spectral diversity and spatial heterogeneity. Before the detailed analysis of its physical content we have extracted typical spectra and spectra at the extreme values of each PC axis in order to assess the major spectral variability over the spectro-image and to identify the main components present on this side of Pluto (Fig. 4).

We can recognize the long series of CH4 bands, the N2 band at 2.15 µm, and the CO band at 1.58 µm already identified from ground based observations (Owen et al., 1993; Douté et al., 1999), as well as the broad bands around 1.5 and 2 µm of water ice recently identified on Pluto and a component corresponding to the dark-red material (Grundy et al., 2016). The sharp CO band at 2.35 µm is not discernible at the resolution of the instrument because blended between the two strongest CH4 bands.

3.2. Reduced noise cube reconstruction

A useful tool provided by PCA is the reconstruction of a reduced noise cube. If we consider that most of the physically

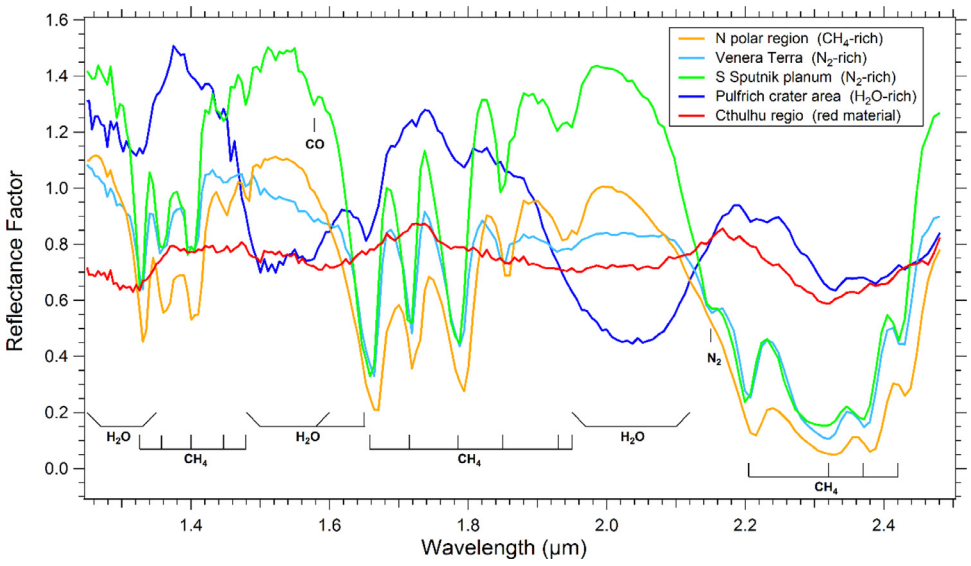

Fig. 4. Local average reflectance factor (REFF) spectra of the surface of Pluto extracted for a few typical areas and some of the extreme values of the physically meaningful PCs. Their location are plotted in Fig. 2. Positions and identification of the main bands of ices are displayed. (For interpretation of the references to colour in this figure legend, the reader is referred to the web version of this article.)

significant signal is contained in the first PC axes (more than 94% of the variance) we can reconstruct a reduced noise spectro-image cube by an inverse PC rotation on a selected number of axes. Several tests were realized using the 12–30 first axes and run the inverse PC rotation using forward noise statistics.

The result is a very clear enhancement of the sharpness of the spectro-image due to the removal of most of noise and instrumental effects. As an illustration, Fig. 5 displays the PCA reduced noise REFF images (using the first 16 PCs) in a CH4 band (spectel #106, 1.788 μm,) as well as local zooms, compared to the initial LEISA image. The improvement is particularly strong at continuum wavelengths where noise dominates the variability of the reflectance. Fig. 6 compares the original and reduced noise REFF LEISA images (spatial resolution ~6.2 km/pixel, spatial re-sampling ~2 km/pixel at image center) with the LORRI base map image (spatial resolution 890 m/pixel (Moore et al., 2016), spatial re-sampling ~200 m/pixel) around *Elliot crater* (lat/long: 12.5°N/138.5°E). The rim, floor and central peak of the crater are much better defined in the reduced noise image, as well as many smaller geologic features that are indiscernible in the original image. This comparison also further demonstrates the quality of the LEISA data. This noise reduction process will allow us to provide multi-spectral images and materials distribution maps derived from LEISA for detailed geological comparison with LORRI panchromatic images and MVIC_4-channel images and their derived geological maps. It will also help to improve the georeferencing process of the LEISA spectro-images on the LORRI images at LEISA sub-pixel accuracy.

For this paper it will allow us to calculate cleaner and sharper maps of spectral indicators, especially those sensitive to noise (weak and narrow bands …). However we first need to verify that the spectra are correctly reconstructed and thus can be used to derive band parameters.

3.3. Test of reduced noise image cube

In addition to spatial improvement the PC reduced noise data should improve the single pixel spectra while retaining most of the spectral physical information. We compared the original and reduced noise spectra (using first 16 PCs) for a large set of single pixel spectra and a set of large average of pixels (500–10,000 pixels), taken in particular in the same area than that presented in Fig. 2, corresponding to extremes values of the different PC axes. Fig. 7 shows a couple of examples of comparison of spectra with large averages of pixels and with one single pixel taken in the middle of the pixel average. It shows that the reduced noise data strongly reduce the noise level of the spectra for single pixels (Fig. 7A) and very well reproduce (i.e., within the noise level) the major bands of CH4, H2O and the dark-red material. However the reduced noise cube fails to reproduce the strength of the N2 band at 2.15 μm (Fig 7B). For the 1.58 μm CO band the evidence of the reconstruction is more subtle as this spectral range is noisier, so the noise-removed CO band sometimes appears weaker (typically by 30–50%), mainly when the CO band is the strongest (Fig. 7B). However comparing with the reconstruction of other average spectra we see that the band shape is more consistently the same. In addition, the weak 1.48 and 1.50 μm CH4 bands are reconstructed with the same position, width and band depth relative to the other CH4 bands despite the different noise that affect the original spectra. So we consider that the reconstruction of the CO band is good and that apparent differences are mostly due to noise.

This demonstrates that most of the spectral energy, and thus physical information contained in the spectra, is conserved with the exception of the 2.15 μm N2 band. Increasing the number of PCs to 30 only slightly improves the reconstruction of the N2 band, while significantly increasing the noise in the reconstructed spectra. The weak spectral energy of N2 (weak band in a narrow spectral range) seems to be dispersed and mixed with noise over several PCs with low weight, while that of CH4, H2O and the non-volatile material are predominantly concentrated in the very first PCs with high weight.

One application of the reduced noise data cube will be to derive maps of specific spectral indicators (i.e. calculated individually for each single pixel of the image) with a much higher accuracy and spatial sharpness than with the original LEISA data. This is particularly exemplified with the calculation of the integrated relative band depth map of CH4 in the 1.90–2.00 μm range (covering the 1.937 + 1.955 μm CH4 band doublet, Quirico et al., 1997a). Despite the large spectral integration over 15 spectral bands the S/N ratio improvement is striking (Fig. 8A,B). The histograms of band depth values of the image show that it transforms from a Gaussian shape,

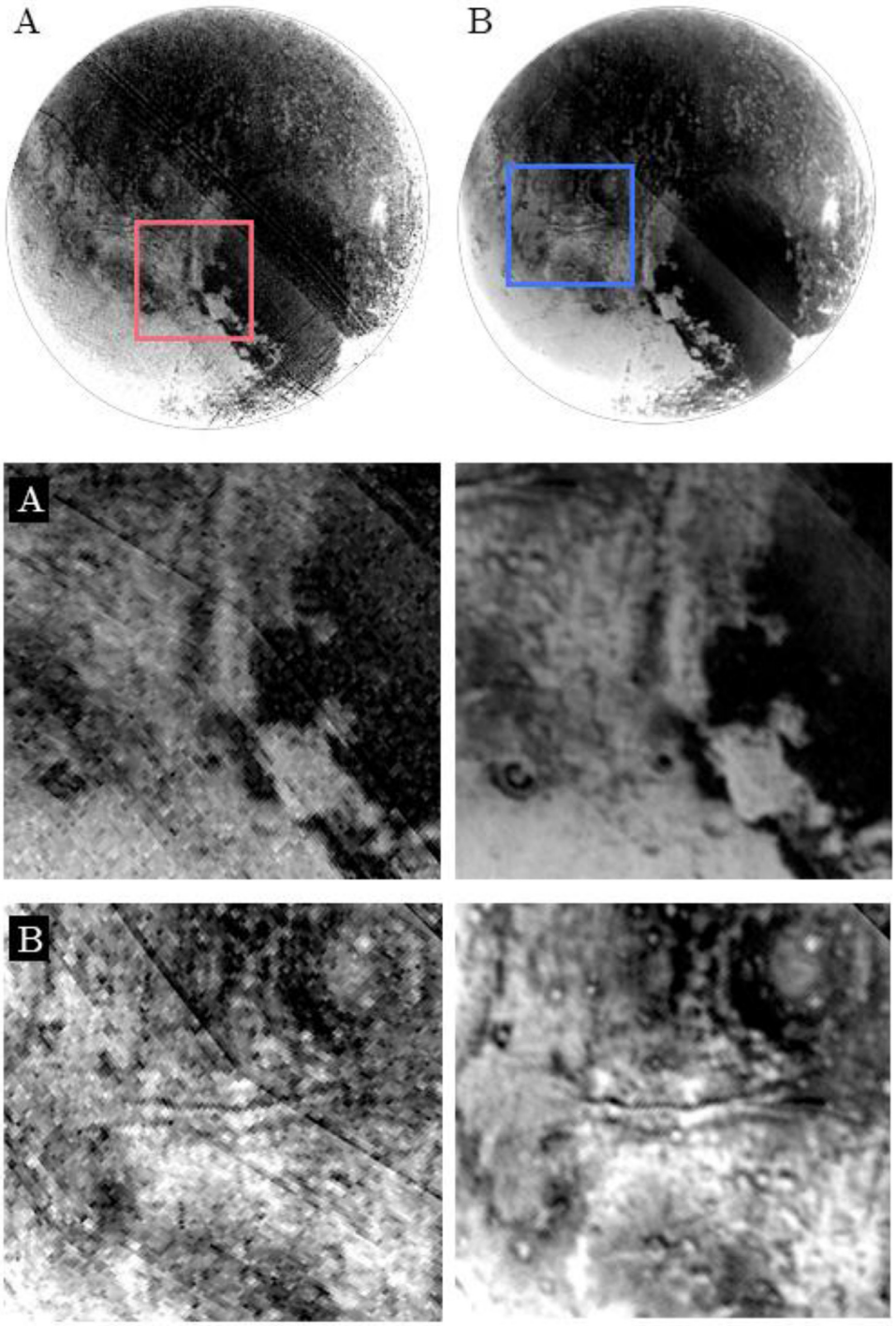

Fig. 5. Comparison between (A) original and (B) PCA reduced noise LEISA REFF images at 1.788 μm (spectel #106). The local zoom corresponding to the red and blue boxes in the full image are displayed at lines 2 and 3, respectively. Look in particular at *Elliot crater* near the lower left corner of image A (see details in Fig. 6). (For interpretation of the references to colour in this figure legend, the reader is referred to the web version of this article.)

dominated by noise, in the original band depth map to a two times narrower and more structured shape (double peak with shoulders) indicating a sharper definition of different types of area (Fig. 8C,D). This reduced noise spectro-image cube will be used to calculate all spectral indicators for the rest of our analysis, except for N2.

For N2, which is not well reconstructed in this full spectrum PCA, we ran PCAs over limited spectral ranges (typically over 40 spectral bands) centered on the 2.15 μm absorption band of N2. The N2-PCA gives three PCs (#4, #5 and #9) that clearly contain the N2 information, in addition to three first PCs similar to that of the global PCA. The reduced noise local spectra obtained from the inverse rotation of the first 5 PCs+ PC#9 now very well reproduce the N2 absorption band of the original data, while removing part of the noise (Fig. 9A).

For the 1.58 μm CO band we also ran several PCAs over limited spectral ranges but the reconstruction of the band was not better than with the global PCA on large averages of spectra. However on individual pixels the CO band appear to be less noisy than with the global PCA reconstruction (Fig. 9B). We also ran a PCA around the 2.35 μm CO band but it did not allowed us to extract this fully

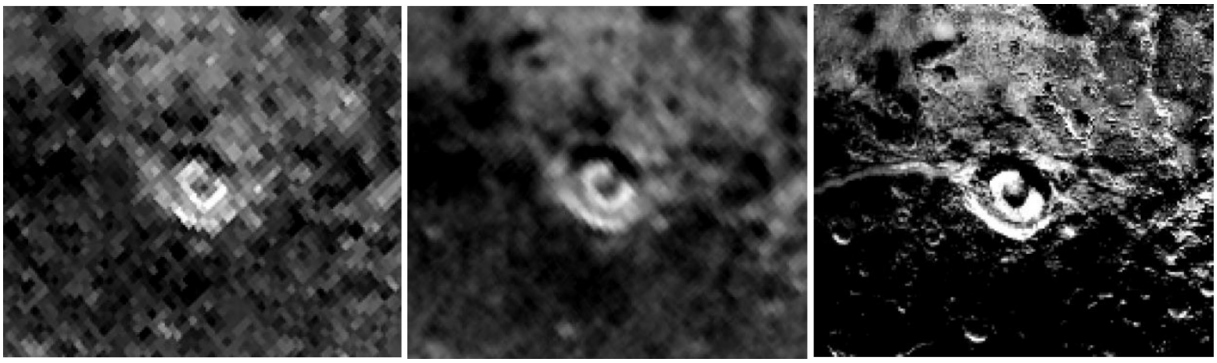

Fig. 6. Comparison between original (left) and PCA reduced noise LEISA REFF images (center) at 2.00 µm (spectel #137) and the LORRI image convolved at 10 times better resolution (right). The image is centered on *Elliot crater* at about 12.5° N Lat. – 138.5°E Long.

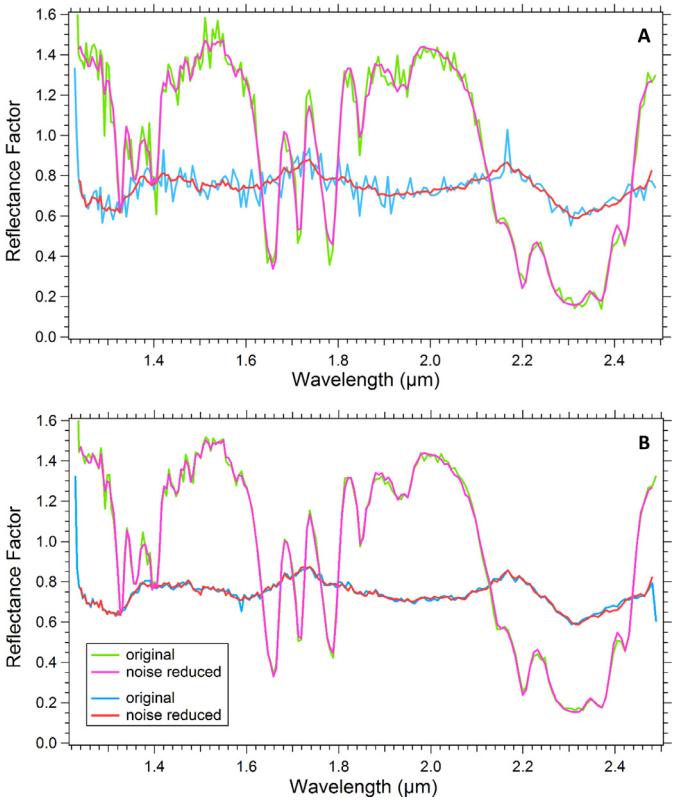

Fig. 7. (A) Comparison of original and reduced noise LEISA REFF spectra of Pluto for one single pixel taken in the center of two of the large pixel averages shown in Fig. 4. It shows the strong reduction in noise level of individual spectra. (B) Comparison of original and reduced noise LEISA REFF spectra of Pluto for two of the large averages of pixels (~500–1500 pixels) presented in Fig. 4. It demonstrates the conservation of the spectral energy, except in the weak N2 band at 2.15 µm (circle). (For interpretation of the references to colour in this figure legend, the reader is referred to the web version of this article.)

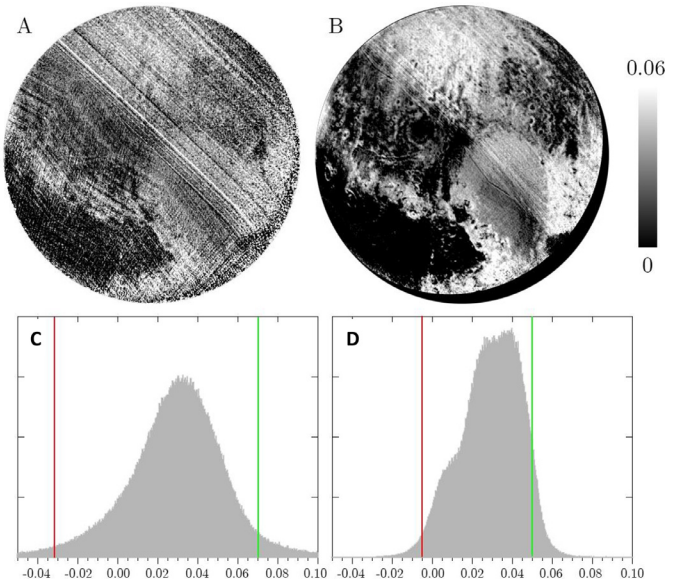

Fig. 8. Comparison of the relative band depth map of CH4 integrated over the 1.90–2.00 µm range calculated with (A) the raw, and (B) PC reduced noise LEISA REFF data. The evolution of the histogram of the values of the CH4 band depth from raw (C) to PC reduced noise data (D) clearly illustrates the sharpening of the image. The vertical lines correspond to 2% (red) and 98% (green) of the values. (For interpretation of the references to colour in this figure legend, the reader is referred to the web version of this article.)

blended band at LEISA spectral resolution. In the following we will use the reconstructed localized spectra from the N2-PCA and CO-PCA to calculate the integrated band area maps of N2 and CO, respectively.

4. Analysis of the data

Based on the first insight on material distribution and diversity we obtained from the PCA analysis we performed a deeper analysis of the data by defining 'classical' integrated band depths and specific spectral indicators in order to map the distribution of the different materials or some of their properties. The comparison of these band depths and indicators, using correlation plots, allowed us to determine the end-members of the different materials and their mixing lines (a mixing line is a straight or curved line of points connecting two end-members in the 2D scatter plot of two band depths or indicators. Along this line the properties described by these depths/indicators varies progressively from one end-member to the other as a result of progressive end-members mixing of one of the four types: spatial, intimate, stratification, molecular). Distribution maps visualizing the progressive evolution from one material to another have been plotted by defining typically 3–5 classes along each mixing lines (1 class around each end-member plus 1–3 intermediate classes). They are only qualitative.

4.1. Albedo and photometry

The near-IR continuum wavelength of CH4 ice (1.522 µm) appears to be well correlated with the NIR channel (780–975 nm) of the MVIC multispectral data converted in REFF (Fig. 10). The

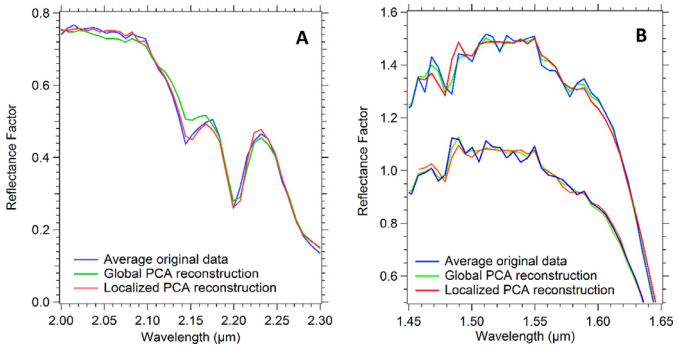

Fig. 9. PCA reconstruction of the weak N2 and CO bands. Comparison of the original LEISA REFF spectrum (blue) of one of the N2-rich large pixel averages of Fig. 4 with the global PCA reconstruction (green) that fails to reproduce the N2 band, and (A) with the local N2-PCA reconstruction (red). This demonstrates the conservation of the spectral energy in the weak N2 band at 2.15 μm. (B) For CO the evidence of the 1.58 μm band reconstruction using the global (green) and the local CO-PCA reconstruction (red) is more subtle as this spectral range is noisier and the band weaker. However comparing with the reconstruction of other averages we can see that the weak 1.48 and 1.50 μm CH4 bands are reconstructed in both red spectra with the same position and same intensity relative to the other bands despite the different noise that affect the two original spectra. (For interpretation of the references to colour in this figure legend, the reader is referred to the web version of this article.)

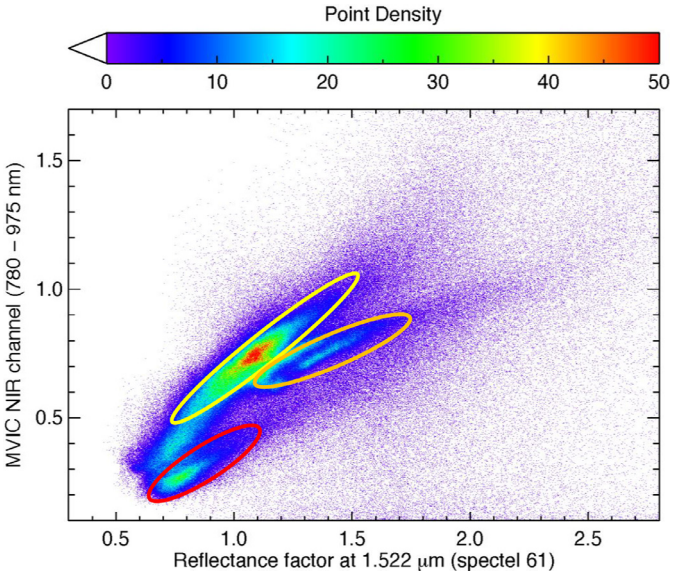

Fig. 11. Correlation plot of the reflectance factor at 1.522 μm (spectel #61) in the CH4 continuum correlated with the NIR channel (780–975 nm) of the MVIC multispectral data converted in REFF. The blue-green-red colors depict increasing density of points. The 3 ellipses show the three different main regions: *Cthulhu Regio* (red), *Sputnik Planitia* (orange) and the rest of the surface (yellow). (For interpretation of the references to colour in this figure legend, the reader is referred to the web version of this article.)

correlation is good (Fig. 11) but displays three major tendencies, the 2 first being well localized at the surface of Pluto: the darkest correlation (red ellipse in Fig. 11) perfectly fits the dark red *Cthulhu Regio*, the lower branch of the main correlation (orange ellipse) mainly corresponds to the bright near-infrared region of *Sputnik Planitia* plus a number of much smaller area mostly dispersed in the NE quadrant and finally the upper correlation branch contains the remaining of the surface (yellow ellipse). These 3 correlation appear to map 3 major types of terrain as we will see in the following. Strong photometric effects are observed at high illumination-observation angles (at phase angle ~22°) near the south and east limbs (the bright fringe at bottom right in Fig. 10A) but they can be partly due to the uncertainties in incidence angle described before. Note that MVIC observation has been recorded at a different phase angle (38.7° at sub-spacecraft point) and with a slightly different sub-spacecraft point (shifted by about −11.5° lat. and +9.5° long.).

4.2. CH4

Methane is the major absorber, with numerous bands, in the global spectrum of Pluto. So it is not surprising that PC#2 (Fig. 3.2) closely depicts the distribution of CH4 as the second source of spectral variability. We defined an integrated band depth over each of the four main groups of CH4 bands (Fig. 13):

$$BD_{\lambda 1,\lambda 2}(CH4) = 1 - \frac{\int_{\lambda 1}^{\lambda 2} RF(\lambda)\, d\lambda}{\int_{\lambda 1}^{\lambda 2} Cont(\lambda)\, d\lambda} \quad (1)$$

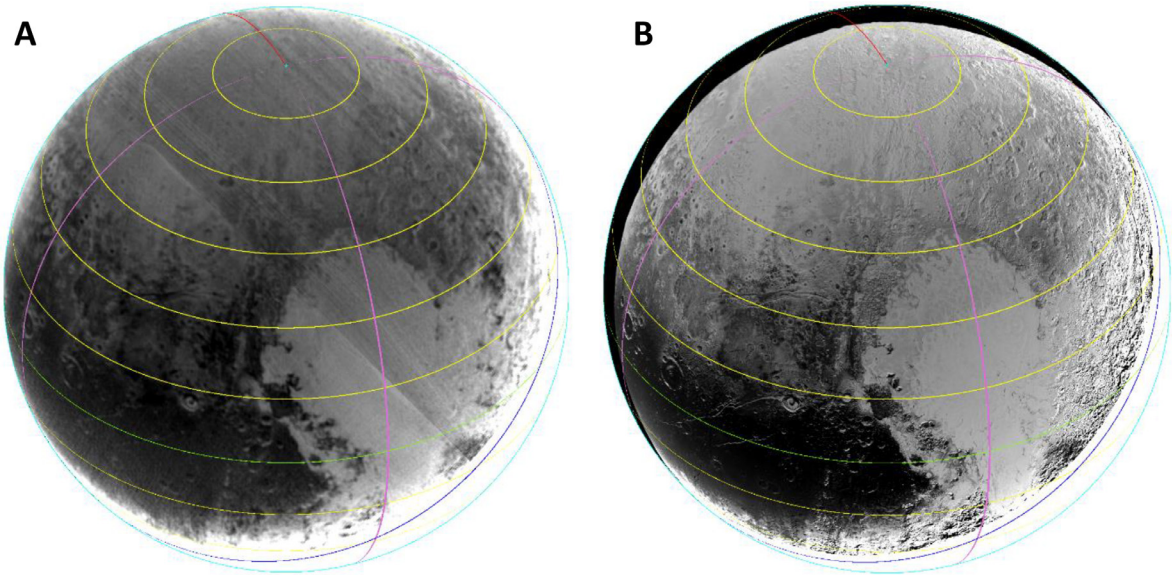

Fig. 10. Reflectance map. Comparison of (A) the reflectance factor REFF of LEISA at 1.522 μm, with (B) the MVIC NIR channel (780–975 nm) in reflectance factor, with same projection. It highlights the current small misfit in absolute calibration between the 2 combined LEISA images (oblique seam in the center).

where λ_1, λ_2 are the integration limits of the bands, RF(λ) the reflectance factor inside the band, and Cont(λ) a linear interpolation of the continuum between λ_1, and λ_2. The integration ranges are the following: between 1.302 and 1.431 µm for group 1, between 1.589 and 1.833 µm for group 2, between 1.90 and 2.00 µm for group 3, and between 2.09 and 2.48 µm for group 4 (Fig. 12). The maps of these integrated band depths are plotted in Fig. 13.

From these maps CH4 appears to be present in various amounts over most of this side of Pluto, except in the central part of *Cthulhu Regio* and *Krun Macula* covered by the dark-red material (see part 4.7) and in a number of smaller places such as *Pulfrich Crater* or *Baré Montes* dominated by water ice (see part 4.6). However the different bands provide relatively different distribution maps of band intensity depending on their strength. In particular the maps from the weakest (1.9–2.0 µm) and strongest bands (2.09–2.48 µm) are markedly different with, in particular, *Sputnik Planitia* displaying the strongest depth for the strongest bands but the weakest depth for the weakest bands. When these integrated band depths are plotted one against each other's (2 of these plots are shown in Fig. 14) a good correlation is found for most CH4, except for *Sputnik Planitia* which is slightly offset (circles in Fig. 14) but differently from one band to another, with the shift relative to the main correlation trend moving from the weakest to the strongest bands. This may depict a somewhat different environment for CH4 such as its dilution state, or the texture of the material (see part 4.4). The strongest bands between 2.3 and 2.4 µm tend to saturate and thus become insensitive to the abundance of CH4 (and grain size) and thus only sensitive to the fractional area covered by CH4-containing ices. We have chosen the second group of CH4 bands, the best compromise between signal-to-noise and saturation, to monitor CH4 on Pluto. The 3.2 µm saturated CH4 band will be used to infer the material locally spatially segregated with CH4-containing ices and its abundance (see part 4.6.2).

The lower left cloud of points in these correlation plots mostly corresponds to the dark red material and water ice which appear to be rather well separated from CH4 in most of these band depths (except for the weakest bands around 1.9–2.0 µm).

In the rest of the paper we choose to use the band depth integrated over the 1.7 µm band group (1.58–1.83 µm) to map CH4 on Pluto, and compare it to other indicators, as it is the best compromise between S/N ratio, band saturation and false positive detections. This integration range well separates water ice from CH4 as it will give a negative value for water dominated terrains (see for example the blue spectrum between 1.58 and 1.85 µm in Fig. 4). Any contribution of water ice will rather minimize the CH4 band depth. The same occurs with the red material. So we found that weak CH4 bands are still present between the broad spectral structures of water or red material, down to values of −0.05. So we set the detection threshold of CH4 at this value for this integrated 1.7 µm-band depth.

4.3. N2 ice

The distribution of N2 ice at the surface of Pluto, can be studied using the integrated area of its 2.15 µm band (Fig. 15):

$$BD(N2) = 1 - \frac{\sum_{2.136\ \mu m}^{2.160\ \mu m} (RF)}{\sum (RF(2.1207\,\mu m) + RF(2.1285\,\mu m) + RF(2.1676\,\mu m) + RF(2.1756\,\mu m))} \quad (2)$$

We determined a detection threshold of the N2 band of 0.005 for this integrated band depth. This integrated band depth has strong values in the area of *Sputnik Planitia* (below 30°N) and in a number of more localized area at mid-latitudes in the northern hemisphere, such as, from W to E, *Venera Terra, Burney crater*, N of *al-Idrisi Montes, Pioneer Terra* and *Hayabusa Terra*. The N2 band depth appears weaker in the northern (above 30°N) and NW

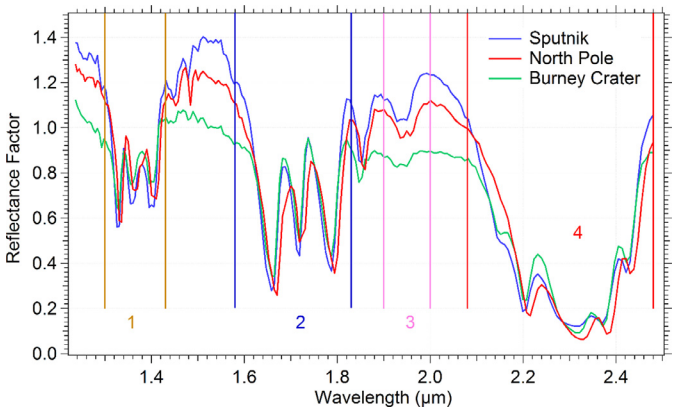

Fig. 12. The four spectral zones of integration defined to calculate the four relative band depth maps of CH4: 1) 1.30–1.43 µm (medium bands); 2) 1.59–1.83 µm (medium-strong bands); 3) 1.90–2.00 µm (weak bands); 4) 2.09–2.48 µm (strong bands). The three spectra illustrate the spectral diversity of CH4-containing ice terrains: CH4-rich ice (North Pole), N2-rich ice (*Sputnik Planitia*), N2-rich ice with water ice (*Burney crater*).

parts of *Sputnik Planitia* as well as along its SW border behind the mountain ranges.

The physical significance of this band depth is not straightforward as the 2.15 µm N2 band is weak and situated on the wing of the very strong 2.20 µm CH4 band. In addition N2 being the major component, its abundance is always in the 95–100% range in the N2-rich:CO:CH4 molecular phase (according to the N2:CH4 phase diagram, Prokhvatilov and Yantsevich, 1983) and thus its abundance in this phase did not play a significant role, only its fractional sub-pixel area. Its grain size, however, partly controls the absolute band depth, but on the other side an increase in amount of CH4 dissolved in N2-rich ice tends to decrease the N2 band depth relative to its 'local continuum' (Fig. 16).

We ran a number of simulations of N2-rich ice spectra using our radiative transfer model (Douté and Schmitt, 1998) and the optical constants of CH4 diluted in N2-rich phase (Quirico and Schmitt, 1997a, 1998a, Quirico et al., 1999) and of N2 ice at 38 K (Grundy et al., 1992, 1993) (Fig. 16). After convolution to LEISA spectral resolution and sampling we calculated the evolution of the N2 band depth (the same way as for Pluto's data) as a function of both N2 grain size (from 100 µm to 75 cm) and amount of CH4 in the N2-rich phase (from 0.1% to 5%, its saturation concentration at 40 K) (black-blue-green curves in Fig. 17 and Fig. 18). We also ran the model for pure crystalline CH4 ice at 40 K with a series of grain sizes (from 10 µm to 3 cm) using the optical constants of Grundy et al. (1995, 2002) (red curve in Figs. 17 and 18). Finally in order to asses any possible interference of water ice the model was run for pure crystalline H2O ice at 40 K with a the same series of grain sizes using the optical constants of Grundy and Schmitt (1997, 1998) (magenta curve in Fig. 18). All these laboratory data come from the GhoSST database (http://ghosst.osug.fr).

Fig. 17 shows that the N2 band depth follows a quite complex pattern with the abundance of CH4, but generally increasing with grain size, except for high CH4 contents (>1%) where it gets negative values for grain sizes up to 3 cm. Calculations made for pure CH4 ice show that false N2 band depth signal can occur if coarse CH4-rich ice grains (>2 mm) are present. Fortunately, from the modeling results of N2:CH4 ices on Pluto

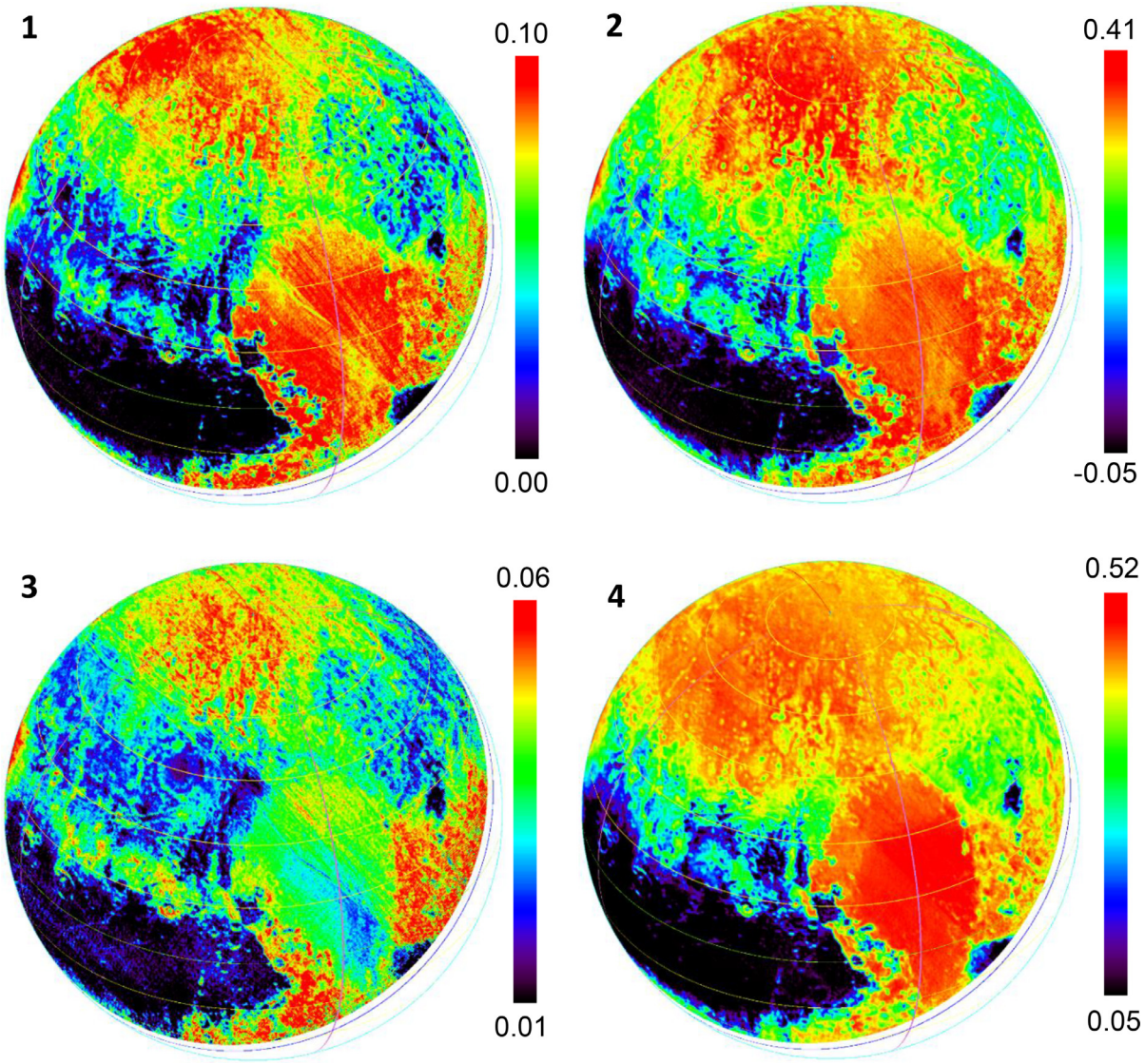

Fig. 13. CH4-containing ices maps. Comparison of maps obtained from the four spectral zones of integration of CH4 band depth defined in Fig. 12: 1) 1.30–1.43 μm (medium bands); 2) 1.58–1.83 μm (medium-strong bands); 3) 1.90–2.00 μm (weak bands); 4) 2.09–2.48 μm (strong bands). The ranges of the scales cover from the detection threshold to the value at 98% of the pixels with positive detection.

(Protopapa et al., 2017) we estimated that pixels containing a significant fraction (>25%) of such coarse grained CH4-rich ice cover less than 3% of Pluto's surface. And less than 0.3% of the pixels in which we detect N2 ice corresponds to these area, where possibly both phases can be mixed. From our CH4 state indicator (see Fig. 20) we can confirm that none of these remaining pixels (<0.01%) contains mostly CH4-rich ice. Thus our Pluto N2 band depth map (Fig. 15) appears not biased by the occurrence of coarse grained CH4-rich ice.

The scatter plot of the CH4 band depth (1.7-μm group) versus the N2 ice band depth over Pluto (Fig. 18A) displays 3 trends: (1) a vertical trend with strongly variable CH4 band depth and negative values of the N2 band depth (blue ellipse), (2) a negative correlation trend, i.e. stronger N2 band depth for weaker CH4 bands depth (orange ellipse), and (3) a horizontal trend which has high and constant CH4 band depth but highly variable N2 ice band depth (red ellipse).

Looking at the same plot drawn with our set of simulated spectra of CH4 in N2-rich ice, CH4 ice and H2O ice with various grain sizes (Fig. 18B) we can see that the first trend corresponds to pure CH4 (or CH4-rich) ice with very small to coarse grains (but <2 mm), but may also contain N2-rich ice with high amount of CH4 (>1%) with relatively large grains (but less than a few cm). The coarsest grained of these ices (dark blue in Fig. 18C) are mostly located in the N polar region but are also dispersed NE, E and SW of *Sputnik Planitia*, while the finer grained ones (light blue) are concentered in a 10–30°N latitude band. The second trend is also well depicted by the models and corresponds to very large N2-rich ice grains (>10 cm) with small to medium amount of CH4 (0.1–1%: yellow to orange in Fig. 18C). It covers most of the 30–60°N latitude band (*Venera, Voyager, Pioneer* and *Hayabusa Terra*, and *Burney crater*). Finally the last trend (red in Fig. 18C) corresponds to very large N2 ice grain sizes (>20 cm) with CH4 concentrations around 1% or higher. It is mostly found in *Sputnik Planitia*, in its W and SW sides and in E *Tombaugh Regio* and *Tartarus Dorsa*, but also dispersed around the N polar region. It seems also that only limited area on Pluto (mostly in N *Vega Terra* and *Piri Planitia*) have both medium N2 grain size (< few cm) and low CH4 content (<1%) (green in Fig. 18C).

This "grain size-CH4 content" classification, based only on direct modeling of pure end-members, is quite qualitative and

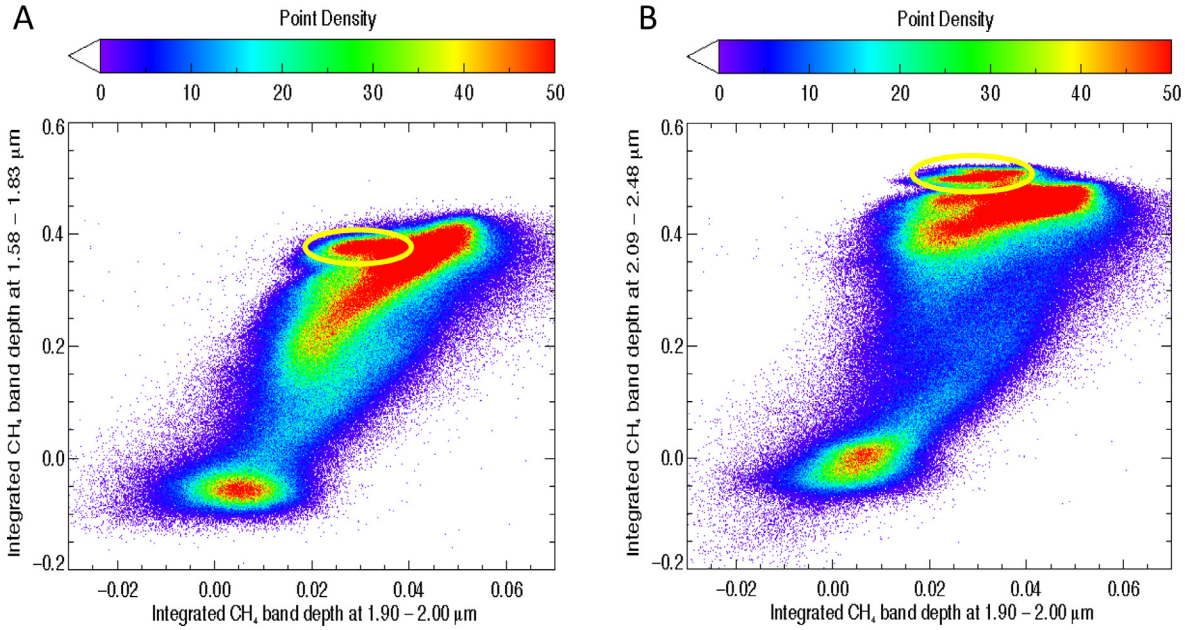

Fig. 14. Correlation plot between the CH4 integrated band depth maps as defined in Fig. 12. (A) 1.58–1.83 µm versus 1.90–2.00 µm, and (B) 2.09–2.48 µm versus 1.90–2.00 µm. The blue-green-red colors depict increasing density of points. A correlation is found for most CH4 (upper half of the curve), except *Sputnik Planitia* which is slightly offset in both plots (yellow ellipse). (For interpretation of the references to colour in this figure legend, the reader is referred to the web version of this article.)

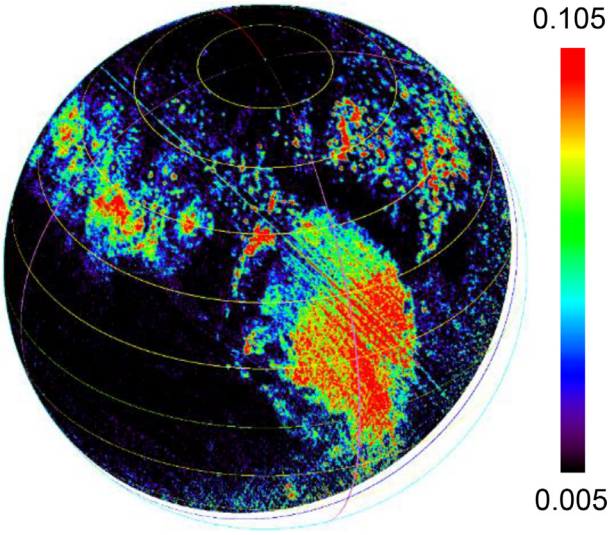

Fig. 15. N2 ice map: integrated band depth of the 2.15 µm N2 band.

need more complete modeling and parameter inversion to extract quantitative values (see Protopapa et al., 2017).

From Fig 18B it should be noted that water ice may produce 'false positive' N2 band depth values for large grain sizes (above about 500 µm). However water ice always gives strongly negative integrated CH4 band depths, so it cannot be confused with N2:CH4 ices.

It is also clear that from this scatter plot that both CH4 and N2 band depths did not allow us to separate CH4-rich ice and centimetric/sub-centimetric grains of N2-rich ice containing large amounts of CH4 (which have no detectable N2 band). Such situation may occur, for example, in the process of differential sublimation of CH4:N2 ice that will concentrate CH4 in N2 grains up to saturation (5% CH4 at 40 K). It is thus necessary to found a spectral indicator that can distinguish between these two major phases. The N2 band depth behavior is quite complex and is not directly correlated with its abundance and only partly with its grain size (for grains >1 cm) with strong interferences from the concentration of CH4. Its modeling together with CH4 is thus requisite to decipher these various effects and extract quantitative information (Protopapa et al., 2017).

4.4. CH4-rich ice vs N2-rich ice

According to the N2:CH4 binary phase diagram that shows that CH4 and N2 are only partly miscible in the solid phase, β-N2-rich:CH4 and CH4(I)-rich:N2 crystalline phases may coexist at Pluto's surface temperature (−40 K) (Prokhvatilov and Yantsevich, 1983). At 40 K they should contain 5% CH4 and 3.5% N2 respectively. These abundances of the minor molecule diluted within the major crystal increase with temperature (up to 34% N2 in CH4 I ice at 60 K). If not enough molecules of one species are available locally at a given place their concentration can be lower than the saturation value, but in such a case only the phase dominated by the major molecule exists. In the following 'CH_4–rich ice' refers to the CH_4-dominant phase of the molecular mixture N_2:CH_4 and 'N2-rich ice' to the N2-dominated phase.

From ground-based hemispheric observations methane has been found at the surface of Pluto in two different solid states: diluted in β-N2-rich ice (together with CO) and as CH4(I)-rich ice (Douté et al., 1999). Thanks to spectral spectroscopic measurements in the laboratory (Quirico et al., 1996; Quirico and Schmitt, 1997a) CH4 diluted in nitrogen ice can be discriminated from CH4-rich ice by two ways: (1) the presence of the 1.69 µm band ($\nu_1+\nu_3$ mode), which is active only for pure and CH4-rich ices and is absent for CH4 diluted in α- and β-N2 ices, and (2) the positions of the CH_4 bands that are strongly shifted towards lower wavelength when CH_4 is diluted in N_2, compared to their positions in pure and CH4(I)-rich ices (Quirico et al., 1996; Quirico and Schmitt, 1997a; Grundy et al., 2002; Protopapa et al., 2015).

Radiative transfer models showed that CH4-rich ice could be present either as separate deposits, and/or as a thin upper layer on top of N2-rich:CH4:CO ice, and/or intimately mixed with N2-rich ice as a binary phase mixture (Douté et al., 1999; Merlin et al., 2010). The relative abundance of these two phases is quantitatively analyzed by spectral modeling in a companion paper

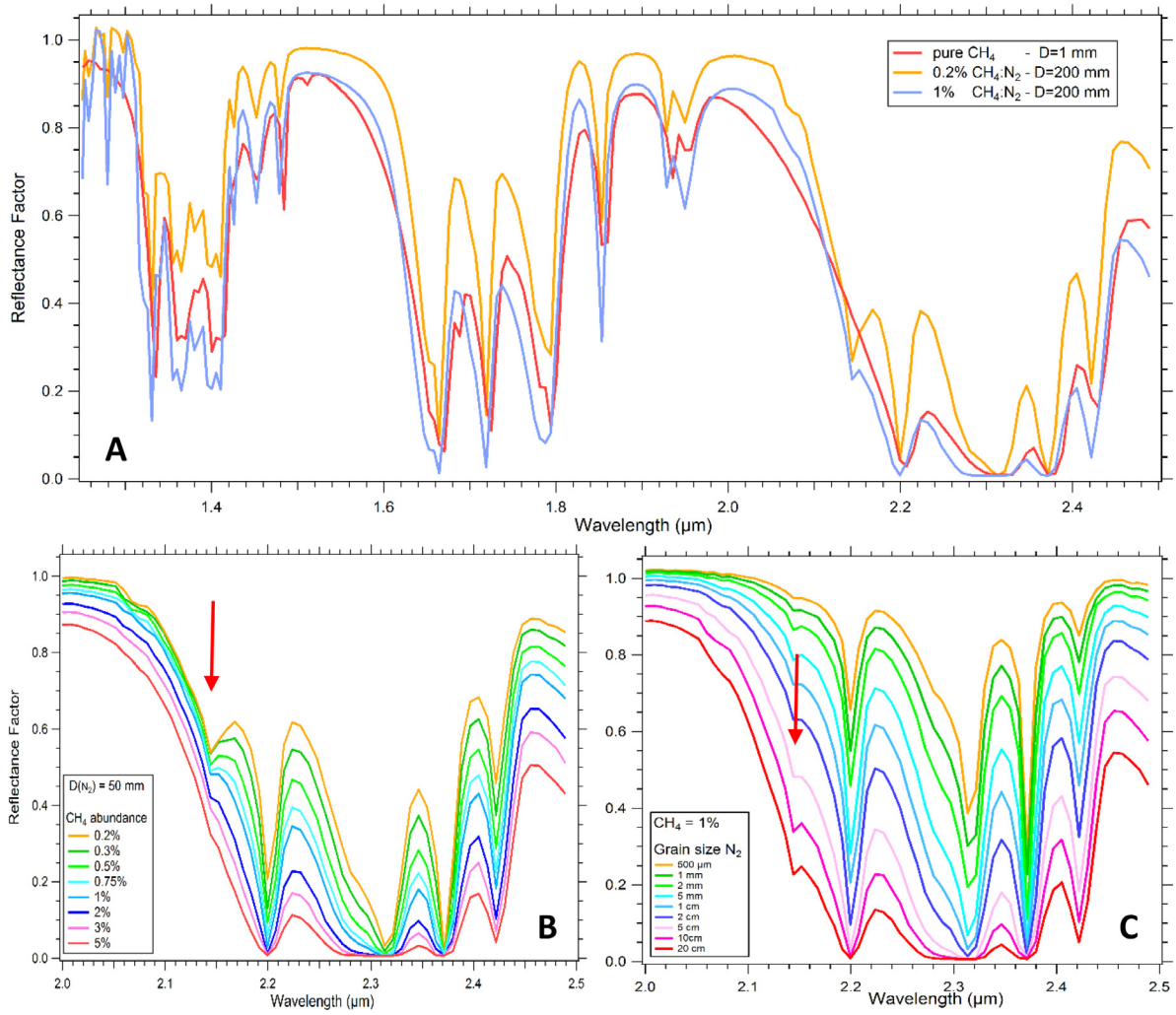

Fig. 16. Simulated spectra of pure CH4 and N2-rich ices. (A) Comparison of band shapes and positions between pure CH4 and N2-rich ices. (B, C) Expanded views of the 2–2.5 μm range for N2-rich ice: (B) with varying amounts of CH4 (grain size: 50 mm) and (C) with varying N2 grain sizes (CH4 = 1%). The disappearance of the N2 band at 2.15 μm (red arrow) with increasing CH4 content is clearly seen (but N2 varies only from 99.8 to 95%). Spectra are convolved at about LEISA resolution. (For interpretation of the references to colour in this figure legend, the reader is referred to the web version of this article.)

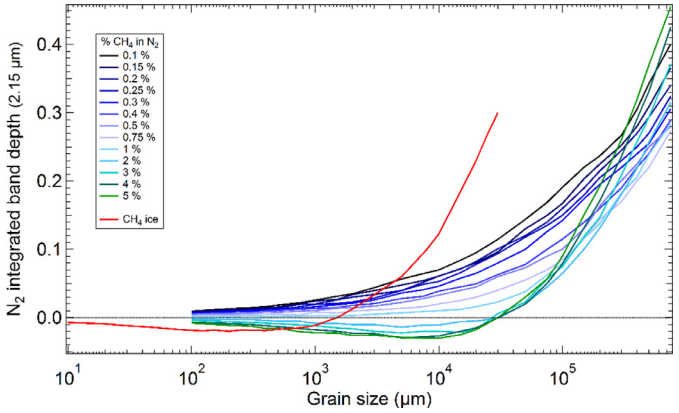

Fig. 17. Evolution of the calculated 2.15 μm N2 band depth as a function of N2 grain size for various amounts of CH4 in the N2-rich phase, as determined from radiative transfer simulations convolved at LEISA spectral resolution. Calculations for pure crystalline CH4 ice are also shown. (For interpretation of the references to colour in this figure legend, the reader is referred to the web version of this article.)

(Protopapa et al., 2017). Here we try to decipher the relative distributions of CH4-rich and N2-rich ice phases and their modes of mixing using specific spectral indicators developed for this aim.

CH_4–rich ice indicators:

The presence of CH_4-rich phases is investigated in the LEISA data by 3 different ways:

- the band shift caused by CH_4 dilution in N_2
- the anti-correlation between CH_4-rich zones determined with the previous criterion and N_2-rich zones as determined by the N2 band depth
- the presence of the 1.69 μm band, indicative of the CH_4-rich phase

4.4.1. Band shift

To assess the possible shift of CH_4 bands on LEISA data, a specific index was created. The minimum position of seven CH_4 bands (around 1.33, 1.36, 1.40, 1.67, 1.72, 1.79 and 2.20 μm) is automatically determined at sub sampling resolution using the spectel with the minimum local value and the ratio of the slopes with its two neighbor spectels to interpolate a more accurate band peak position. The spectral ranges used for each band are indicated in Fig. 19. A value of 1 is given to the spectel at the lowest wavelength for each of these ranges. The addition of these minimum positions (in relative spectel unit) provides an index of the overall CH_4 bands shift for a given pixel (varying typically between 20 and 52). The higher the index, the purer the CH_4.

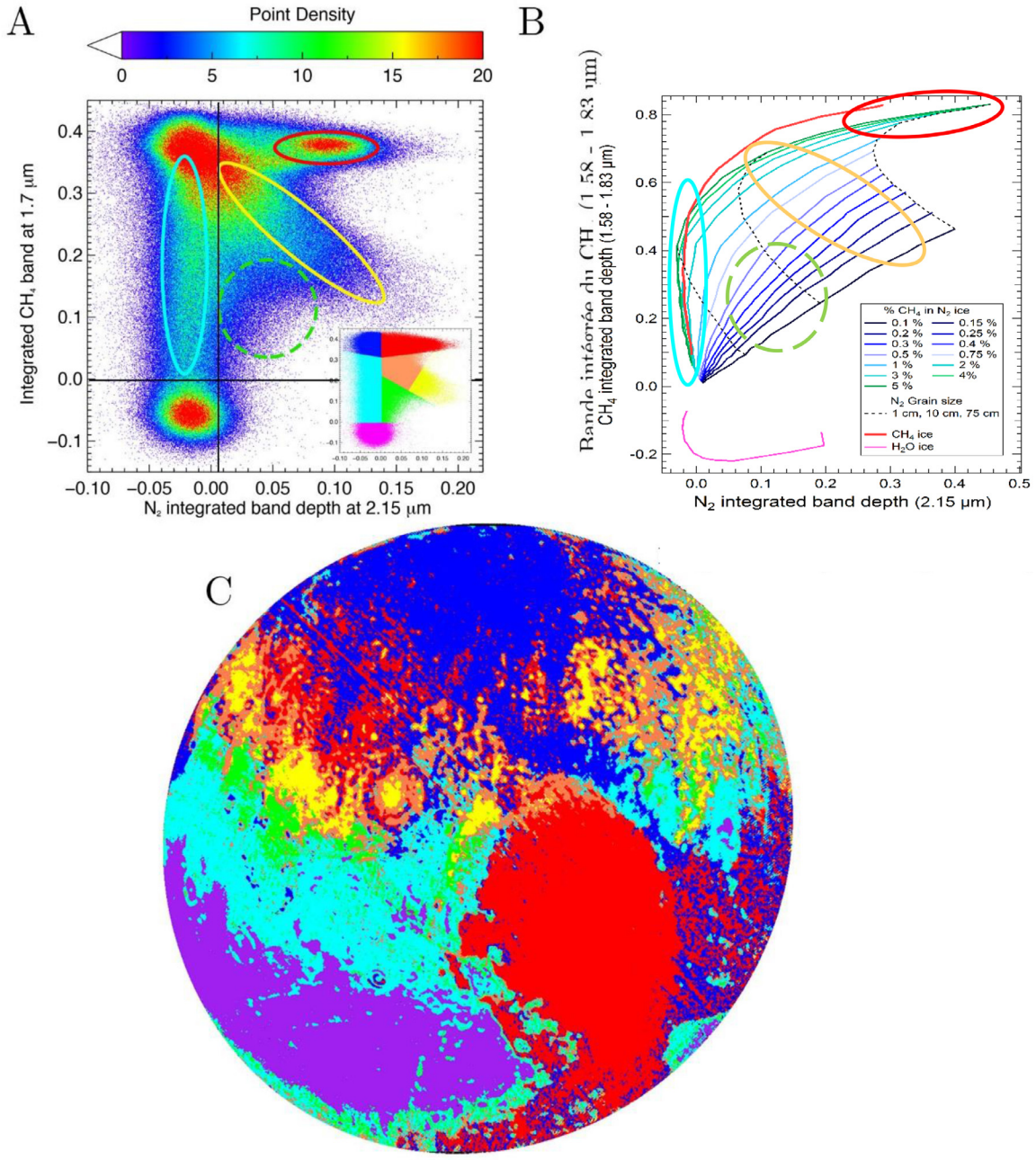

Fig. 18. CH4 versus N2 band depths. (A) Scatter plot of the 1.7-µm CH4 integrated band depth versus the 2.15 µm N2 integrated band depth. The ellipses correspond to the 3 trends described in the text and the black lines are the detection thresholds of the CH4 and N2 bands. (B) Same for spectra generated by radiative transfer modeling of pure CH4 ice and N2-rich ice containing various amounts of CH4 for a series of grain sizes (increasing from the origin of the graph to the top right dotted curve (75 cm) for N2-rich ices, and up to 3 cm for pure CH4 ice. The clearly separated 'false detection' values for H2O ice are also plotted (grain size increases from left (10 µm) to right (3 mm) of its curve). (C) Map of the distribution of the materials sampled by the 7 classes defined in the scatter plot (insert in (A)). Trend #1: pure CH4 (or CH4-rich) ice, or N2-rich ice with grains < few cm and high amount of CH4 (> 1%) (light blue and blue). Trend #2: large N2-rich ice grains (>10 cm) with small to medium amount of CH4 (0.1–1%: yellow to orange). Trend #3 (red): very large N2 ice grain sizes (>20 cm) with CH4 concentrations around 1% or higher. There is only little N2-rich ice on Pluto with both medium N2 grain size (< few cm) and low CH4 content (<1%: green). (For interpretation of the references to colour in this figure legend, the reader is referred to the web version of this article.)

From the laboratory data of Quirico and Schmitt (1997a) we determine that the band shifts from highly diluted CH4 to pure CH4 ice (around 40 K) vary from 3.3 to 5.8 nm for these 7 bands, corresponding to 0.65–0.95 LEISA spectels with an average shift of 0.75 spectel per band. So our CH4 indicator will shift by 5.25 units (from ~36.5 to 42) between these 2 extreme states. However when N2-rich ice reaches saturation (start of the two phase system N2-rich + CH4-rich), ~5% CH4 can be diluted in N2 ice leading to an average band shifts of 0.35 nm (calculated from Protopapa et al., 2015), i.e. ~0.4 unit in our index. On the other side the ~3.5–34% of N2 that can be incorporated in CH4 ice between 40 and 60 K respectively, leads to a negligible band shift at 40 K (~0.06 nm), i.e., less than −0.1 index unit relative to pure CH4, but to a measurable shift if CH4 is saturated with N2 at 60 K (0.5 nm, −0.6 index unit). However, as we will see, the current spectral calibration and smile effect in Pluto's spectro-images preclude detection of such subtle spectral shifts.

The map of this index, presented in Fig. 20, displays the CH_4-rich ice zones in red-to-green colors and the N_2-rich ices zones in light-to-dark blue. Areas without CH4 and N2 are in black, mostly

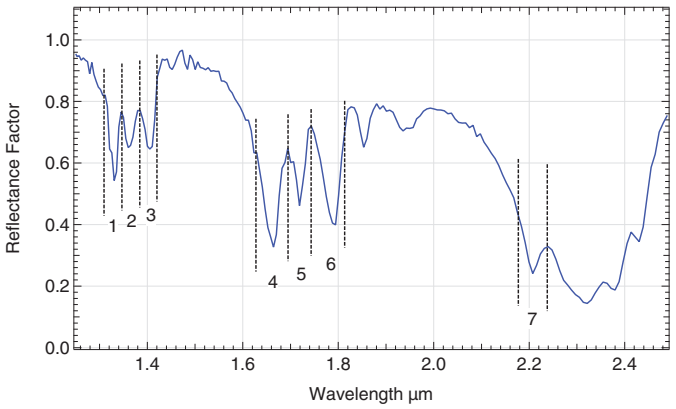

Fig. 19. Spectral ranges used to determine the position of the minimum for each selected CH4 band.

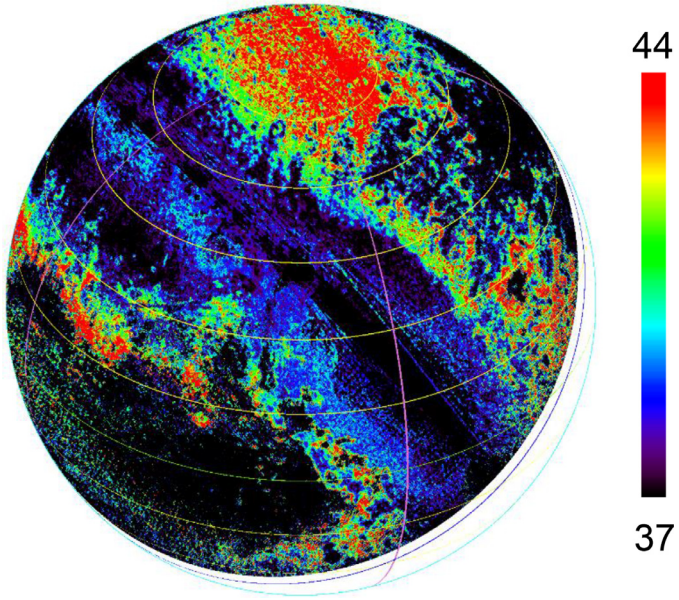

Fig. 20. Map of the state of CH4 as determined by the CH4 bands position index. The red to green colors indicate CH4 bands positions toward CH4-rich ice phase (nominal index value = 42) while light to dark blue indicate shifts toward N2-rich ice phase (lower wavelengths, nominal index value = 36.5). Black is for no CH4, nor N2 ices. This figure has to be compared with the N2 ice band depth map in Fig. 15. (For interpretation of the references to colour in this figure legend, the reader is referred to the web version of this article.)

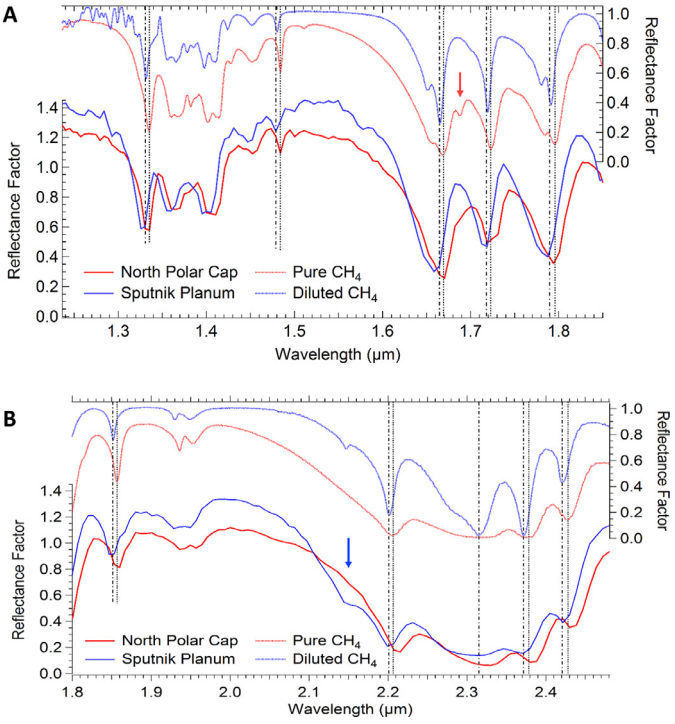

Fig. 21. Comparison of typical Pluto spectra of N2-rich (*Sputnik Planitia*) and CH4-rich ices (*North Polar Region*) in the spectral regions: A) 1.24–1.85 µm, and B) 1.80–2.48 µm dominated by several CH4 bands. The CH4 band positions are marked with dotted (pure) and dash-dotted lines (diluted). The N2-rich ice spectrum displays the 2.15 µm N2 band (blue arrow) and the CH4-rich ice spectrum displays a shoulder near 1.69 µm (red arrow) due to the activated µ1 + µ3 CH4 mode (Quirico and Schmitt, 1997a). (For interpretation of the references to colour in this figure legend, the reader is referred to the web version of this article.)

Ctlulhu and a few water ice rich spots (see part 4.6 and 4.7). With this index there is a transition from materials without N2-ice to N2-rich ice in the range between values 34 and 36 (see Fig. 22) so we set a conservative threshold at index >37. The NW-SE strip of dominated by N2-rich ice has index values very close to this threshold so it appears mostly very dark blue in Fig. 20. This map can be directly compared to the N_2 map calculated earlier (Fig. 15) to see their complementarity. The CH_4–rich ice zones are mostly located in the N polar region (above ~60°N), NE of *Sputnik Planitia* and in the E and SW parts of *Tombaugh Regio*, as well as along the northern (~15–35°N) border of *Cthulhu Regio*, dominated by red material.

The sharpness of the map validates the sensitivity of the method. However part of this global band shift could be related to the smile effect that affects LEISA data. The smile effect translates into a global wavelength shift of the spectrum as we move from the center to the edges of the original image (before geographic projection). Typically, on Pluto's map, the smile effect is along a NE-SW axis and increases from about the center of each two constituting images toward their edges (but slightly asymmetrically shaped). However, the strong regional and local variations observed throughout Pluto indicate that our criterion is valid and that the smile effect, even if present and superimposed, plays a smaller and smoother role in the measured band shift. It should be noted here that in the process of cutting and gluing the 2 original images we attempted to eliminate as much as possible the areas with the largest smile effect.

To illustrate the sensitivity of the method we extracted two spectra from two different areas that both exhibit CH4 absorptions but different CH4 band positions (Fig. 21). We selected their location to be at about the same distance from the center column of the original image to avoid any smile effect. The differences in the band positions are clearly visible.

4.4.2. Anti-correlation between CH_4–rich and N_2–rich areas

Both maps of N2 and CH4 integrated band depths, previously determined (Fig. 15 and 13.2), should be compared to this CH4 band position index in order to assess how it can allow to separate N2-rich and CH4-rich icy terrains. In Fig. 22A the N_2 ice band depth at 2.15 µm is plotted versus the CH4 bands position index, while Fig. 22B shows the correlation plot between CH4 integrated band depth and this same position index. In Fig. 22A zones that are characterized by the strongest N_2 ice band depths have a low value (~34–39) of the CH4 band positions index, while zones with low values of N_2 band depth (<0.03) extend to higher values (~41–45) of CH4 band position index. All the pixels with high index have only strong CH4 band depths (Fig. 22B), confirming they should be covered with CH4-rich ice. Pixels with index below this range have a much wider range of CH4 band depths, pointing

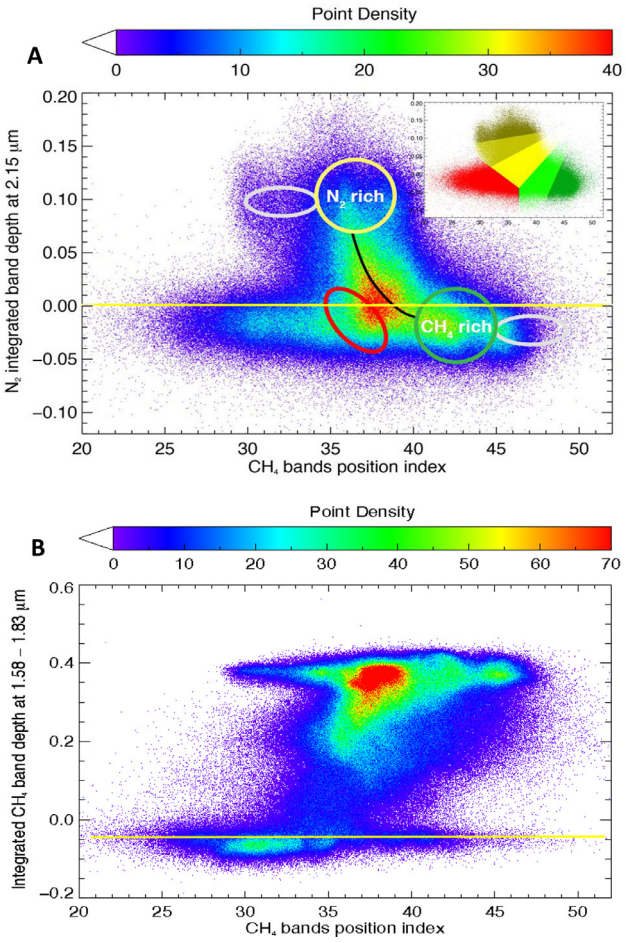

Fig. 22. Correlation plots of N2 and CH4 ice band depths versus the CH4 bands position index. (A) N2 ice band depth at 2.15 µm. (B) integrated CH4 band depth around 1.7 µm. The yellow horizontal lines gives the threshold of N2 and CH4 detection with their band depths (0.005 and −0.05 respectively). The position of CH4 diluted in N2 ice is at value 36.5 ± 2.5 (yellow circle). N2 saturated CH4 ice phase (~3.5% N2) and pure CH4 ice are at value 42 ± 2.5 (green circle). The grey ellipses show the index shifts due to the spectral smile effect (mostly along the seam of the 2 images). The red ellipse locates CH4 at high concentration in centimeter/sub-centimeter grained N2-rich ice. All other points with both low N2 band depth and low CH4 band depth are from the other materials (H2O ice and the dark-red material). The black line materializes the progressive transition from N2-rich to CH4-rich ice. The insert depicts the classes defined along this transition and that will be plotted in Fig. 40. (For interpretation of the references to colour in this figure legend, the reader is referred to the web version of this article.)

to N2-rich ice containing varying amounts of CH4. Points with both low N2 band depth and very low CH4 index (<~34) have also negative integrated CH4 band depths and are thus from the other materials (H2O ice and the dark-red material). A small number of the pixels covered by these materials have higher index values (up to ~41), mostly due to noise on top of their broad spectral structures, but they can be easily discriminated thanks to their negative integrated CH4 band depths (Fig. 22B). In Fig. 22A they contribute very little to the high concentration of points with low index (<40) that have slightly negative values of N2 band depth, at about the same level as CH4-rich ice. Most of these points have medium to high CH4 band depth (Fig. 22B). These pixels are most probably covered with centimetric/sub-centimetric grained N2-rich ice containing CH4 at high concentration that cannot be distinguished from CH4-rich ice on the basis of both CH4 and N2 band depths, as demonstrated by our simulations (Figs. 17 and 18). Thanks to the CH4 bands position index this type of N2-rich ice can now be readily distinguished from CH4-rich phases. Indeed the laboratory data show that the shift for CH4 diluted at saturation (5%) in N2 ice relative to CH4-rich ice is still −4.85 units in our index, giving an index of 37, so clearly away from the CH4-rich ice pole (nominal index value = 42).

Finally, the effect of spectral smile is seen on the plot as a dispersion of points on both sides of the N2-rich pole and on the right side of the CH4-rich pole (merged with data on the other side). It accounts for a maximum ±3 index points, i.e. a total spectral shift of less than the LEISA spectral sampling. The future correction of this smile effect will sharpen this correlation plot and allow an even better separation between the different types of materials and phases.

The progressive L-shaped transition (dark blue line) taking place from N2-rich ice to CH4-rich ice in the correlation plot is due to the binary phase diagram of solid N2-CH4 with reciprocal low saturation limits in each phases (Prokhvatilov and Yantsevich, 1983) which constrain the coexistence of both phases over most of the global composition range. This well populated transition line points to an evolution process involving a progressive change (at subpixel scale) of the relative abundances of N2-rich and CH4-rich ice phases by preferential removing of the most volatile component, N2, and converting CH4 diluted in N2-rich ice to a CH4-rich phase. However this plot cannot discriminate between the three possible microphysical evolution scenarios: a simple subpixel spatial segregation of both phases, a phase segregation at the crystal level, a vertical segregation of both phases or some combination of them. Douté et al. (1999) evidenced the presence of a vertical segregation of CH4-rich ice over N2-rich ice with differential shift of the weak and strong CH4 bands followed by the radiative transfer simulation of the spectra. If we had higher spectral resolution and better wavelength precision (no smile effect …) it could be possible to search for differential shifts between strong and weak bands, and so different states at different depths. But this is not the case with the current state of LEISA calibration. Future detailed modeling of well selected series of spectra may be able to provide some constraints on this question in the future. This will be discussed in some more details later (in part *5.1.5*) when the 5 classes drawn along this line in Fig. 22 (insert) will be plotted on a map (Fig. 40).

4.4.3. The 1.69 µm shoulder

When individual spectra are collected at the place where the most CH4-rich ices are detected by the previous CH4 index they almost always show a small shoulder around 1.69 µm between the two strong CH4 bands at ~1.67 and ~1.72 µm (Fig. 21A), while this band is always absent in areas of N2-rich ice. This shoulder is clearly present in large averages (Fig. 23). However it was not possible to design a spectral indicator that satisfactorily probe this shoulder without being affected by the strong spectral shift of the surrounding two CH4 bands dominating the signal. However the visual inspection of the data and the examples shown provide an additional demonstration that the CH4-rich area are indeed dominated by pure or almost pure CH4 ice phases. It should also be noted that this 1.69 µm band strongly decreases in intensity with increasing temperature, being 3.5 times weaker at 60 K than at 40 K at high spectral resolution (Grundy et al., 2002). So given the lower spectral resolution of LEISA, patches of pure CH4 at high temperature (~60 K) may not display this shoulder, as for N2-rich ice. Unfortunately the spectral resolution of LEISA is not high enough to resolve it and use it as a CH4 ice thermometer. However the presence of this shoulder may tell that the CH4-rich ice is not hot. In addition most of the CH4-rich ice bands are T sensitive (width and intensity) but spectral resolutions at least 4–8 nm are required (W. Grundy et al., 2002), which is within the range of LEISA SWIR resolution (5–10 nm) and especially its high spectral resolution channel (4 nm) from 2.10 to 2.25 µm. However width and intensity being strongly dependent on the radiative

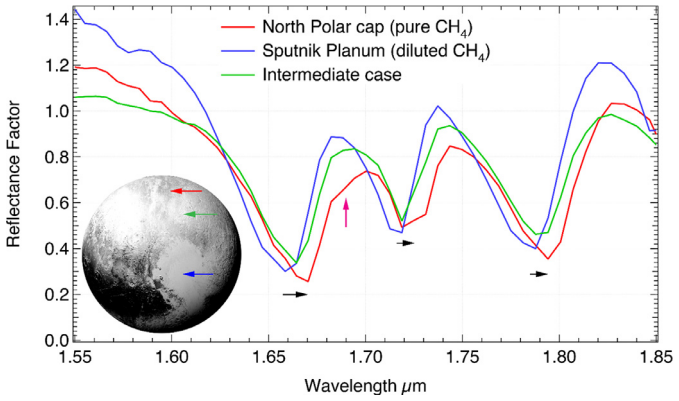

Fig. 23. Comparison of typical large average spectra (1400–2300 pixels) of N2-rich ice (*Sputnik Planitia*: blue), CH4-rich ice (*North Polar Region*: red) and an intermediate case (which also contains spatially mixed H2O ice: green) in the spectral region 1.55–1.85 μm, collected using the CH4 bands position index map (Fig. 20). The band shifts are indicated by black arrows and the 1.69 μm shoulder by a red arrow. The insert shows the position of the 3 areas on the CH4 bands position index map with same colors. (For interpretation of the references to colour in this figure legend, the reader is referred to the web version of this article.)

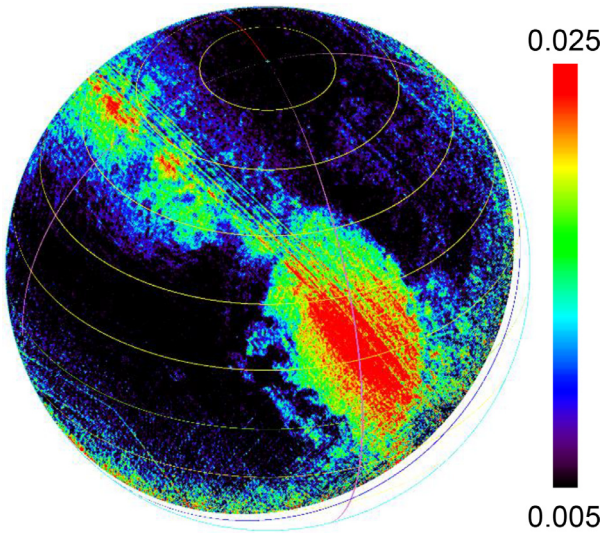

Fig. 24. Integrated band depth of the weak CO band at 1.58 μm calculated on the CO-PCA reduced noise cube centered on this band. To be conservative we set a detection threshold at 20% of the near-maximum value, i.e. 0.005.

transfer this will need a full spectral modeling to possibly provide some temperature constraints on the CH4-rich ice phase.

4.5. CO

The CO band around 1.58 μm being weak and very narrow, typically covering only three LEISA spectels, the definition of the 'integrated' area is very sensitive to various instrumental effects such as imperfectly calibrated spectel response and spectral smile. A large number of tests have been devoted to this band in order to choose the best spectels defining the CO band and the continuum. Thanks to the reduction of noise (which has about the same intensity than the CO band) by the PCA the continuum anchor point's levels are much more stable than in the raw spectra. We defined the 'integrated' band depth of CO as:

$$BD(CO) = 1 - \frac{RF(1.572\,\mu m) + RF(1.578\,\mu m) + RF(1.583\,\mu m)}{1.5*[RF(1.566\,\mu m) + RF(1.589\,\mu m)]} \quad (3)$$

The continuum anchor point on the high wavelength side (at 1.589 μm) of the CO band, situated at the beginning of the wing of the 1.66 μm CH4 band, is somewhat sensitive to the intensity of this band and to the type of CH4 present (CH4-rich or diluted in N2-rich ice) as a result of the spectral shift of the band. Both modulate the level and curvature of the 'CH4 continuum' below the CO band, and thus also partly the CO band depth as defined in Eq. (3).

When Eq. (3) is applied on the raw data the main structure of the CO band depth map can be barely determined only after spatial binning to 12 × 12 pixels (see Fig. 1C in Grundy et al., 2016). The full spatial resolution integrated CO band depth map calculated on the CO-PCA reduced noise data cube is presented in Fig. 24. In order to take into account the uncertainties on the continuum we have set a conservative detection threshold at 20% of the near-maximum value (95% of the values), i.e. BD(CO) >0.005. As discussed before it is also possible that the reduction of noise has altered the strength of the CO band, but from the comparison of a series of large pixel spectral averages before and after noise reduction (see 2 examples in Fig. 9B) it seems that this process mostly affect the strongest CO bands but preserve the intensity hierarchy.

The integrated CO band depth map shows the strongest signature in center and south *Sputnik Planitia* (green spectrum in Fig. 4), and in the 40–60° latitude band of the W part of the N hemisphere (South *Venera Terra, Burney crater,* S *Voyager Terra)*, as well as in a few spots in E *Tombaugh Regio.* It has also a 'relatively strong' band where N2 displays a weak band (e.g. NW of *Sputnik Planitia*) but, on the other hand, it has only weak band depth in most places of the northern hemisphere where strong N2 band depth has been found (N *Vega Terra, Pioneer* and *Hayabusa Terra*). The *North Polar Region* as well as several large area (such as the area bordering NE of *Sputnik Planitia,* N *Viking Terra…*) appear devoid of CO, where N2 is also absent. However, despite these differences in relative intensity, when looking globally the extent of CO distribution appears relatively well correlated with that of N2 (Fig. 15).

The scatter plot of the CO band depth versus the N2 band depth (Fig. 25A) displays a good but wide correlation between both spectral indicators (red line). It also shows a second trend with N2 occurring with weak or no CO (orange line, along the CO detection threshold). This trend exactly corresponds to N *Vega Terra, Pioneer* and *Hayabusa Terra.* The correlation plot of CO band depth with the CH4 bands position index (Fig. 25B) is very similar to the one of N2 band depth versus this same index (Fig. 22A) and quite clearly shows that there is virtually no CO detectable in area dominated by CH4-rich ice and that most, if not all, CO is located in area where N2-rich ice is present.

The scatter plot between Pluto's CO 1.58 μm band depth and CH4 1.7-μm group integrated band depth (Fig. 25C) shows no clear global correlation, only the maximum of CO seems correlated with the amount of CH4 (yellow line). Otherwise a wide range of CO band depth is found for the same CH4 band depth, in particular for strong CH4 band depths where it goes from no CO in the *North Polar Region* (blue ellipse), consistently with its absence in CH4-rich ice, to the deepest CO band depth in central and S parts of *Sputnik Planitia* (white ellipse).

The range of variation of the relative amount of CO and CH4 is better seen in the plot of Pluto's CO/CH4 band depth ratio as a function of the CH4 1.7-μm band depth (Fig. 25D). This ratio is mapped in Fig. 26A. Its shows particularly strong CO/CH4 ratios in two small area (S *Voyager Terra* and SW *Venera Terra*) and in central parts of *Sputnik Planitia.* There is also possibly another area with strong CO/CH4, just emerging along the east limb of Pluto at N mid-latitude in the Eastern part of *Hayabusa Terra.*

Using the plot in Fig. 25D we defined 7 classes (in the insert) which are reported in the map of Fig. 26B. The classes mostly separate the 4 concentrations of points (red spots) seen in Fig. 25C/D

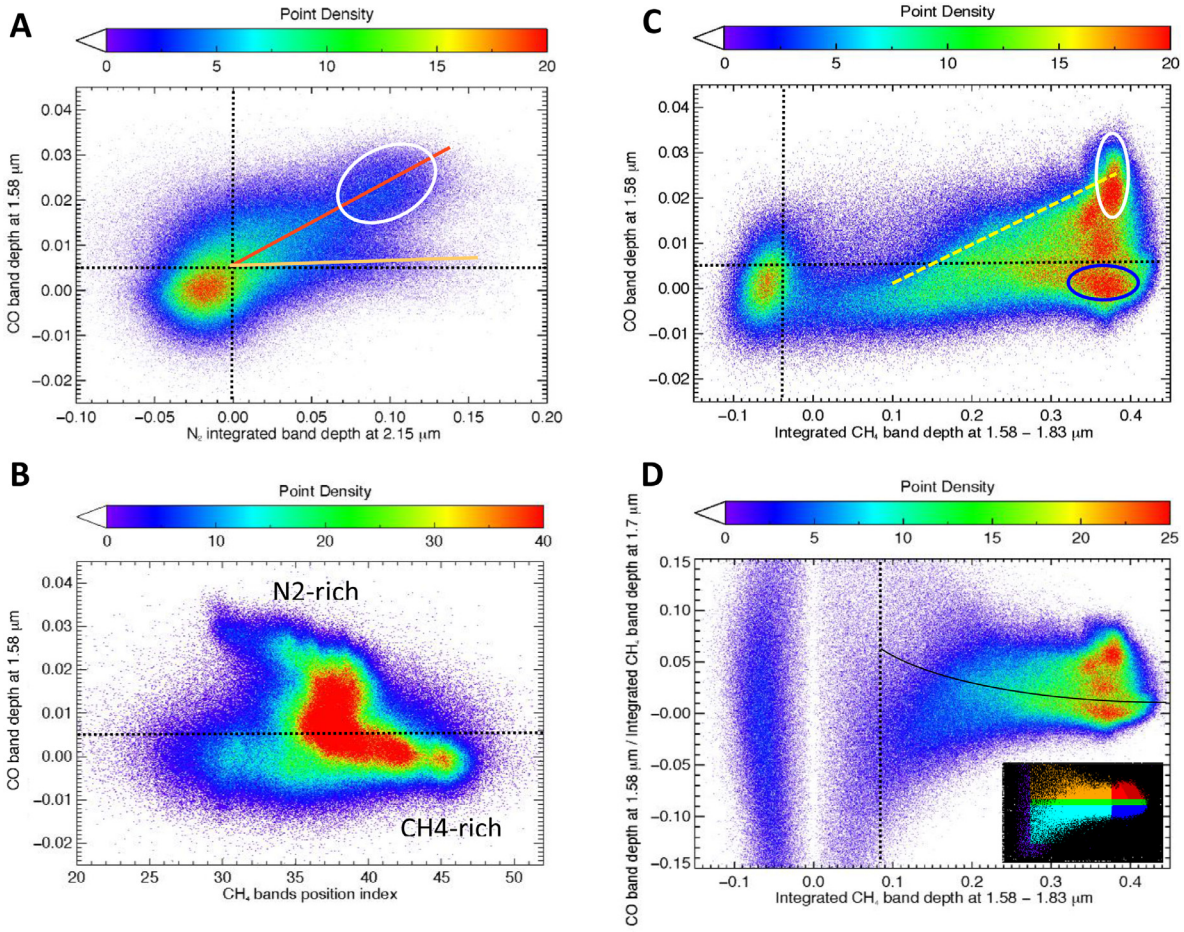

Fig. 25. (A) Scatter plot of the 1.58 µm CO band depth versus the integrated depth of the 2.15 µm N2 band. The white ellipse mainly corresponds to *Sputnik Planitia*. The vertical line is the detection threshold of N2 (0.005) and the horizontal lines in all graphs are the detection threshold for CO (0.005). (B) Plot of the CO band depth versus the CH4 bands position index. CO is clearly absent in CH4-rich ice. (C) Scatter plot of the 1.58 µm CO band depth versus the CH4 1.7 µm-group integrated band depth. The white ellipse shows the increased amount of CO in *Sputnik Planitia* and SW *Tombaugh Regio* relative to the general trend. The blue ellipse corresponds to the *North Polar Region*. The yellow dotted line shows the correlation between maximum of CO and CH4. The vertical line is the detection threshold of CH4 (−0.05). (D) Plot of the CO/CH4 band depth ratio versus the CH4 1.7 µm-group band depth. The horizontal curved line is the detection threshold of CO/CH4 and the vertical line is a CH4 band depth threshold under which the CO/CH4 ratio is very inaccurate and which is applied in Fig. 26A. The 7 classes defined in the insert are plotted in the distribution map of Fig. 26B. They mostly separate the 4 concentrations of points seen in Fig. 25C with high CH4 abundance and with strong CO (dark red, and red), medium CO depth (dark green) and without detectable CO (dark blue), on which 3 classes are added for the low CH4 abundances, with high (orange) and low CO (light green) and without CO (light blue). (For interpretation of the references to colour in this figure legend, the reader is referred to the web version of this article.)

with large CH4 band depth and with the strongest CO (dark red, and red), medium CO band depth (dark green) and without detectable CO (dark blue), on which we added 3 classes to map the area with low CH4 abundances and with high (orange) and low CO (light green) and without CO (light blue). This map shows that the main area that has both a large CH4 band depth and a large CO/CH4 ratio is again *Sputnik Planitia* (with a decreasing gradient in its Northern part), but also in the S and SW parts of *Venera Terra* and in a large number of localized spots in E and SW *Tombaugh Regio*. However, the two areas which display the strongest CO/CH4 ratio (Fig. 26A) have rather medium (SW *Venera Terra*) to low CH4 band depth (S *Voyager Terra*) according to the CH4 band depth map (Fig. 13.2). On the opposite, areas with no or undetectable CO correspond either to places with strong to medium CH4 bands and dominated by CH4-rich ice (*North Polar Region*, dark blue, but also in many spots in East *Tombaugh Regio* and *Tartarus Dorsa*, as well as S *Vega Terra* along the NW fringe of *Cthulhu Regio*. Compare Fig. 26B with Fig. 20) or to areas classified as N2-rich ice but with both undetectable N2 band and small CH4 band depth that well correspond to the areas we suspected to have both relatively small N2 grain size (< few cm) and large amount of CH4 (>1%). The small grain size may thus also explain why the CO band is not detected. So, despite this non-detection, these areas (most of the light blue class in Fig. 36B, but excluding the purest CH4-rich area as determined in Fig. 20) have good chance to contain CO in solid solution in small N2 grains. They cover most of the latitude band between 25° and 40° on the W part of the N hemisphere but occur in many dispersed spots between 30 and 65° latitudes in the Eastern part.

All these results show a global latitudinal trend in the CO/CH4 distribution (with the obvious exception of *Sputnik Planitia*), modulated by local topography, with decreasing values both towards the *North Pole* and the equator, pointing towards a differentiation process of CO occurring during the N2-rich to CH4-rich ice transition driven by N2 sublimation. At this point it is not possible to determine if some differentiation between CO and N2 also occurs. Due to the similar dependency of the CO and CH4 band depths to parameters (their abundance and the N2 grain size) the CO/CH4 band depth ratio is representative of the CO/CH4 abundance ratio in N2-rich ice. However this is not the case for the CO/N2 ratio, as for CH4/N2, due to the fact that the N2 band depth also depends on the CH4 abundance (see Section 4.3).

Quantifying and mapping the abundances of CO and CH4 in N2-rich ices and their ratio require a full radiative transfer

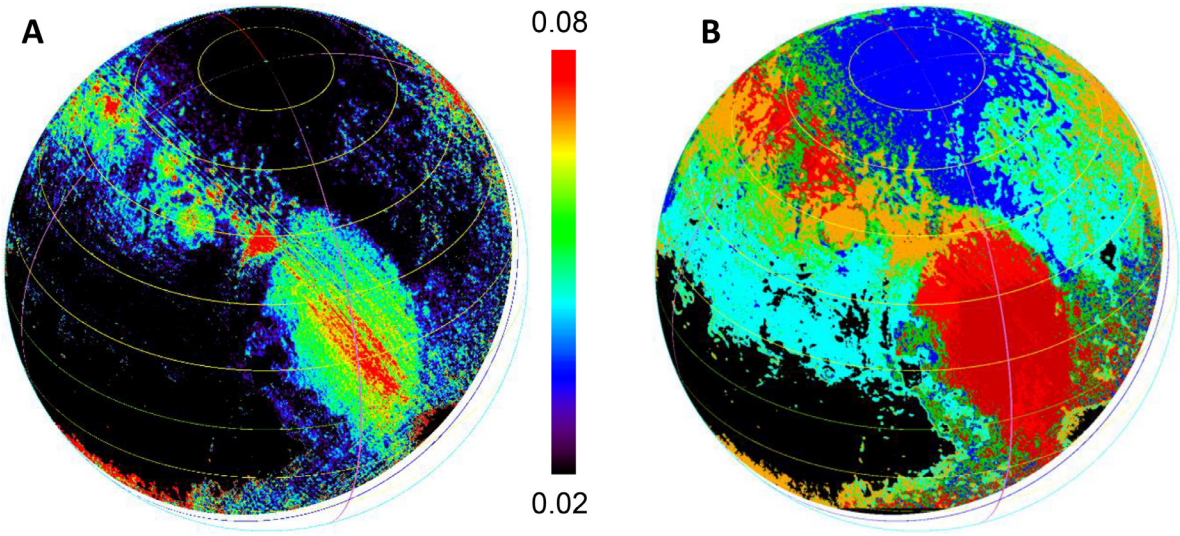

Fig. 26. (A) Distribution map of the CO/CH4 band depth ratio. The two spotty red areas along the South limb (S of *Cthulhu Regio* and in *Krun Macula*) are most probably due to noise. (B) Classification of the CO/CH4 ratio in the 7 classes defined in the insert of Fig 25D: dark red to orange: High CO/CH4 ratio, for decreasing CH4 band depth. Dark to light green: Low CO/CH4 ratio, for decreasing CH4 band depth. Dark to light blue: No or below detection threshold CO band (very low to negative CO/CH4 ratio), for decreasing CH4 band depth. These maps have to be compared with Fig. 20 (map of CH4 state). (For interpretation of the references to colour in this figure legend, the reader is referred to the web version of this article.)

modeling of the spectra. A first determination of the CH4/N2 ratio in N2-rich ices as well as the relative proportions of CH4-rich and N2-rich ices have been obtained by global modeling of these same observations and are presented in a companion paper (Protopapa et al., 2017).

4.6. Water ice

Water ice has been discovered on Pluto in a limited number of places (Grundy et al., 2016). We defined two 'classical' integrated band depths of H2O ice over its 1.5 and 2 μm bands by choosing continuum anchor points at wavelengths near local maxima of reflectance for water ice but also situated near the peak of CH4 bands, or on their wing, in order to clearly separate H2O ice from the ubiquitous methane ice. They are calculated by integrating the band area using the same equation than for CH4 (Eq. 1) over the 1.40–1.72 and 1.85–2.18 μm ranges, respectively (Fig. 27), and are presented in Fig. 28A,B.

The counterpart of this unavoidable choice of continuum wavelengths is that water ice may still be present while the calculated 'band depth' has already negative values. The problem is to define down to which negative threshold water ice can still be positively detected when mixed with CH4-containing ices. Note that other choices of continuum wavelengths could be done, at least for the 1.5 μm band, that will give only positive band depths, but at the cost of a very poor separation between H2O and CH4 absorptions and false contributions by CH4. Fig. 28C shows the same 2-μm band depth but with its detection threshold set to −0.23 (typical ranges of values for CH4-dominated ices are [−0.30, −0.45] over *Sputnik Planitia* and [−0.25, −0.30] over the *North Polar Region*). This point will be further addressed below.

The maps display distinctly the occurrence of water ice in the eastern part of *Tombaugh Regio* around *Pulfrich Crater*, in *Al-Idrisi, Baré* and *Hillary Montes*, in the northern parts of *Viking Terra*, in *Virgil Fossa*, and in *Vega Terra*, as well as in the western part of *Krun Macula*, near the south limb. Water ice signature appears particularly strong in the first place.

The integrated depths of the 1.5-μm and 2-μm bands give very similar distributions of water ice, and quite similar band intensities for high H2O ice band depths. On the other hand the two

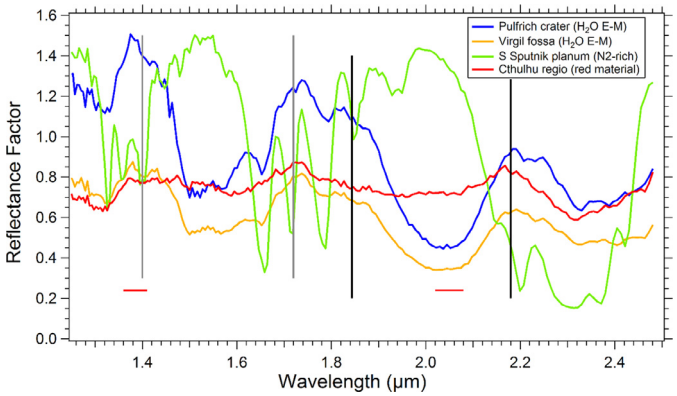

Fig. 27. The two H2O ice end-members identified in the scatter plot of Fig. 31: the '*Pulfrich crater* end-member' (dark blue) and the '*Virgil Fossa* end-member' (orange). They are both the average of the 35 most extreme pixels from Fig. 31. The green spectrum is a typical CH4-rich spectrum from *Sputnik Planitia*, and the red one is the end-member of the red material (from *Cthulhu Regio*). The H2O band depth integration ranges are drawn with the grey (1.5 μm) and black vertical lines (2 μm) while the ranges of wavelengths used for our H2O spectral indicator are drawn as small red horizontal bars. (For interpretation of the references to colour in this figure legend, the reader is referred to the web version of this article.)

band depth maps display different relative behaviors over the red material covered *Cthulhu Regio*. We can note that our 2-μm map is very similar to the one obtained by correlating Pluto's spectra with a Charon-like H2O ice spectrum (Fig. 2 of Grundy et al., 2016). However there is a strong spectral similarity between water ice and the red material over this range of wavelengths (Fig. 27). The difference between the two maps thus raises the question whether or not, and how, water ice is mixed with the dark red material or if their spectral similarity (due to water of hydration in the red material, for example) makes difficult to separate them.

4.6.1. End-members and mixing lines

In order to disentangle the occurrence of H2O ice with both the red material and CH4-containing ices, and to look into more detail at their mixing state we designed a spectral indicator that best separate them. This spectral indicator is the depth of the

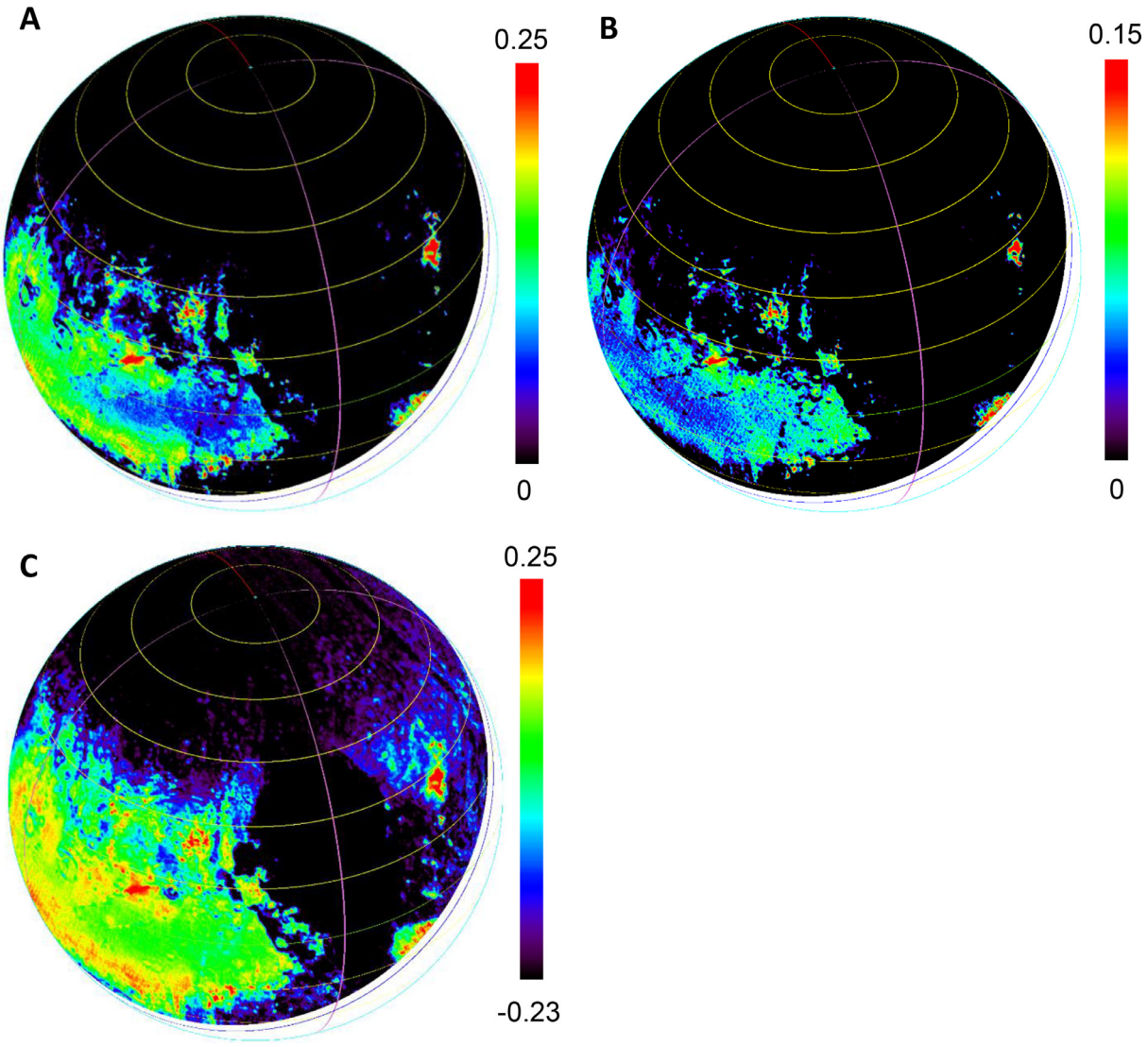

Fig. 28. H2O ice maps. Integrated band depth over (A) the 2 µm and (B) 1.5 µm bands of H2O ice with the minimum threshold set to 0. (C) Same as (A) but with the minimum threshold set to −0.23. The 'rainbow color table' is set between the minimum threshold and the maximum value on the map. (For interpretation of the references to colour in this figure legend, the reader is referred to the web version of this article.)

2-µm H2O peak (around 2.05 µm) relative to its continuum around 1.38 µm (Fig. 27), the two wavelength ranges that are found the most sensitive along the H2O-Red material mixing line (Fig. 29, see 4.7) and also maximizing the contrast with CH4 ice (1.36 and 1.40 µm bands versus its continuum around 2 µm).

The spectral indicator (SI) for water ice is defined as:

$$\mathrm{SI(H2O)} = 1 - -\frac{\sum_{2.090\mu m}^{2.022\mu m}(RF)}{\sum_{1.410\mu m}^{1.365\mu m}(RF)} \quad (4)$$

The map of this spectral indicator (Fig. 30A) displays the same strong water ice spots, as well as a similar distribution over the whole *Cthulhu Regio* as the 1.5-µm band depth map (with threshold set to −0.23, Fig. 28C), but with relatively smaller values. There is a clear hint toward a widespread mixing between both materials. On the side of the negative values there are large area (mostly in *Hayabusa, Pioneer* and also *Voyager Terra*) with moderately low values of our indicator (> -0.25) which may not be compatible with CH4-containing ices. Before considering this point we will look at the positive values of our H2O spectral indicator.

The correlation plot of our H2O spectral indicator versus the 2-µm H2O ice band (Fig. 31A) displays three branches in the

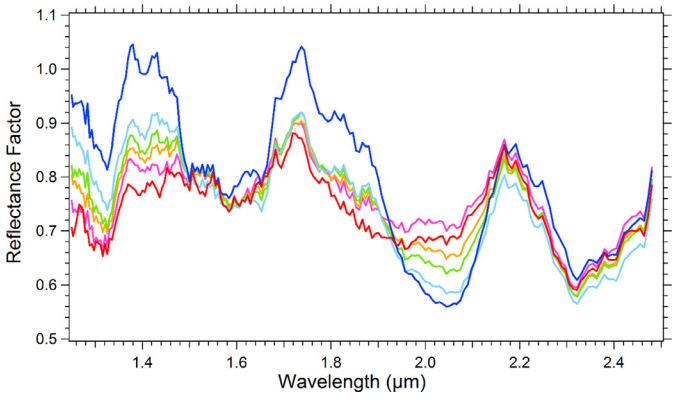

Fig. 29. Evolution of the spectra along the mixing line between the red material and H2O ice, evidenced in Fig. 31 (within *Cthulhu Regio*, red ellipse),. The red spectrum is the end-member of the red material (red point in Fig. 31B). The dark blue is the 'Vigil Fossa end-member' (orange point in Fig. 31B). (For interpretation of the references to colour in this figure legend, the reader is referred to the web version of this article.)

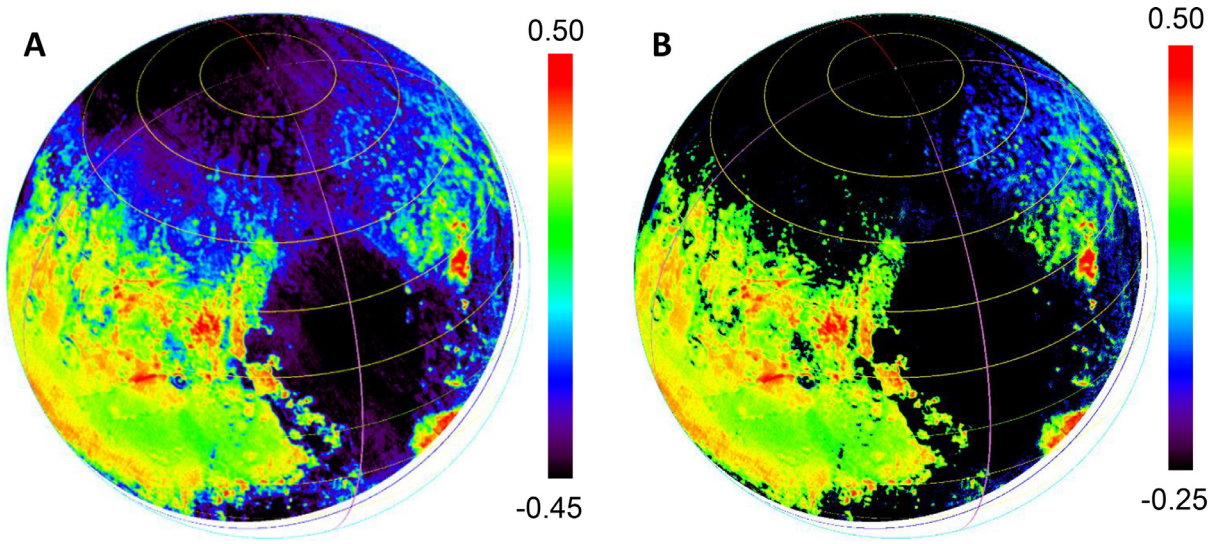

Fig. 30. H2O ice. Map of the spectral indicator of H2O ice defined to optimize the separation from the red material signature and from CH4-containing ices. (A) Raw indicator. (B) Indicator filtered for positive values (green-to-red), except for high blue MVIC slopes (< -2) where the minimum threshold is set to −0.25 (blue tints) (see text and Fig. 31). (For interpretation of the references to colour in this figure legend, the reader is referred to the web version of this article.)

direction of both strong H2O ice band depth and spectral indicator (upper right) pointing to 3 different types of end-members or mixing lines. The first one (orange point in Fig. 31B) mostly occurs in a few spots around *Cthulhu Regio* (15°N–30°S latitude), in particular in *Virgil Fossa*, and has a continuous mixing transition with the red material covering most of Cthulhu Regio (red ellipse). The second end-member (blue point) is mostly concentrated near *Pulfrich Crater*, in connection with surrounding CH4-containing ices and with a sharp transition in spatial distribution. On the other hand it has no local connection with red materials (Fig. 31B).

Fig. 27 shows the two end-members spectra (averaged over the most extreme 35 pixels). The *Virgil Fossa* end-member clearly displays a different shape compared to the *Pulfrich Crater* end-member, mainly in the 1.65 µm band which is much weaker. Its lower reflectance and its red visible color (from MVIC data, Grundy et al., 2016) is indicative of some contamination by the dark red material, in agreement with its position on the line linking the dark red material end-member (from *Cthulhu Regio*) and the *Pulfrich Crater* end-member (bluish in the visible, so probably quite pure) in the scatter plot (Fig. 31B). This points to a well-defined 'H2O ice – red material' mixing line. The spectra regularly collected along this line (Fig. 29) indeed show a progressive spectral change from the red material end member spectrum to almost the *Virgil Fossa* intermediate 'dirty H2O end-member'.

From this scatter plot (Fig. 31) there are clearly at least two types of mixing lines: the 'H2O ice - red material' mixing line described above and a mixing line between the relatively pure H2O ice 'Pulfrich end-member' and CH4-containing ices. A possible weaker mixing line seems to occur between H2O ice contaminated with red material and CH4-containing ices (purple in Fig. 31). It is mostly located almost all along the fringe of the dark red *Cthulhu Regio*.

4.6.2. Distributed water ice in bluish terrains

From the classes map (Fig. 31D) defined along the mixing lines in the scatter plot (Fig. 31C) we infer a possible extended distribution of water ice at low concentration (with moderately negative values of our H2O spectral indicator, typically > -0.25), mixed spatially or intimately with CH4-containing ices. This area extends over the southern part of *Venera Terra* (between about 40°−50°N lat.), *Burney crater, Voyager, Pioneer* and *Hayabusa Terra*. Over most of these regions N2-rich ices have been detected (Fig. 15). According to our model calculations, only CH4:N2 ices with a very low product of CH4 concentration * N2 grain size can reproduce moderately low negative values of our H2O spectral indicator (larger products give strongly negative values). However we found that these area have rather large grain sizes with low to high CH4 concentrations (yellow, orange, to red classes in Fig. 18). Instead, the coexistence of another material, namely H2O ice or red material, is suspected here.

An additional independent indicator that confirms the presence of another material in these area is the reflectance factor in the deepest, mostly saturated, CH4 band at 2.32 µm. When CH4-rich or N2-rich ices are 'red material-free' this reflectance factor, dominated by the first external reflection on grains, should be very small (see Fig. 16), only in the range 0.01–0.05 for CH4-rich grain sizes ≥100 µm and for N2-rich grain sizes ≥1–25 mm according to our models (for CH4 concentration in the range 5%−0.2% respectively; and for low to moderate incidence and emergence angles). However values as high as 0.1–0.2 are measured, with almost saturated 2.32 µm band shape (Fig. 32), in several places where our indicator has moderately negative values. Indeed, the distribution map of the 2.32 µm reflectance factor is very similar to the one of our spectral H2O indicator outside the area of the red material. In most cases this increase of reflectance at 2.32 µm cannot be attributed to small N2 grain size or low CH4 concentration because a narrow unsaturated band will result. In the series of spectra collected in Fig. 32 the increase of reflectance at 2.32 µm is clearly correlated with a decreasing reflectance at 1.5 and 2 µm due to H2O ice, although the shape of the corresponding absorption bands cannot yet be clearly distinguished.

Indeed, up to 20–30% of very fine grained H2O ice (typically <50 µm in size), which has a high 2.32 µm reflectance, can create an increase in reflectance at this wavelength while keeping difficult to detect it spectrally in the 1.5 or 2 µm ranges (Fig. 33). Such H2O ice may be spatially mixed at the sub-pixel level with CH4-containing ices but it may be also present as a thin upper layer or as intimately mixed (at granular level). Similar effects can be obtained with the red material, although needing more material to significantly absorb at 1.5 and 2 µm (Fig. 34). However this material will create a red slope in the visible range that can be detected by the color channels of the MVIC instrument.

To check the extent to which water ice and red material effectively contribute to the different areas of Pluto we plotted our H2O

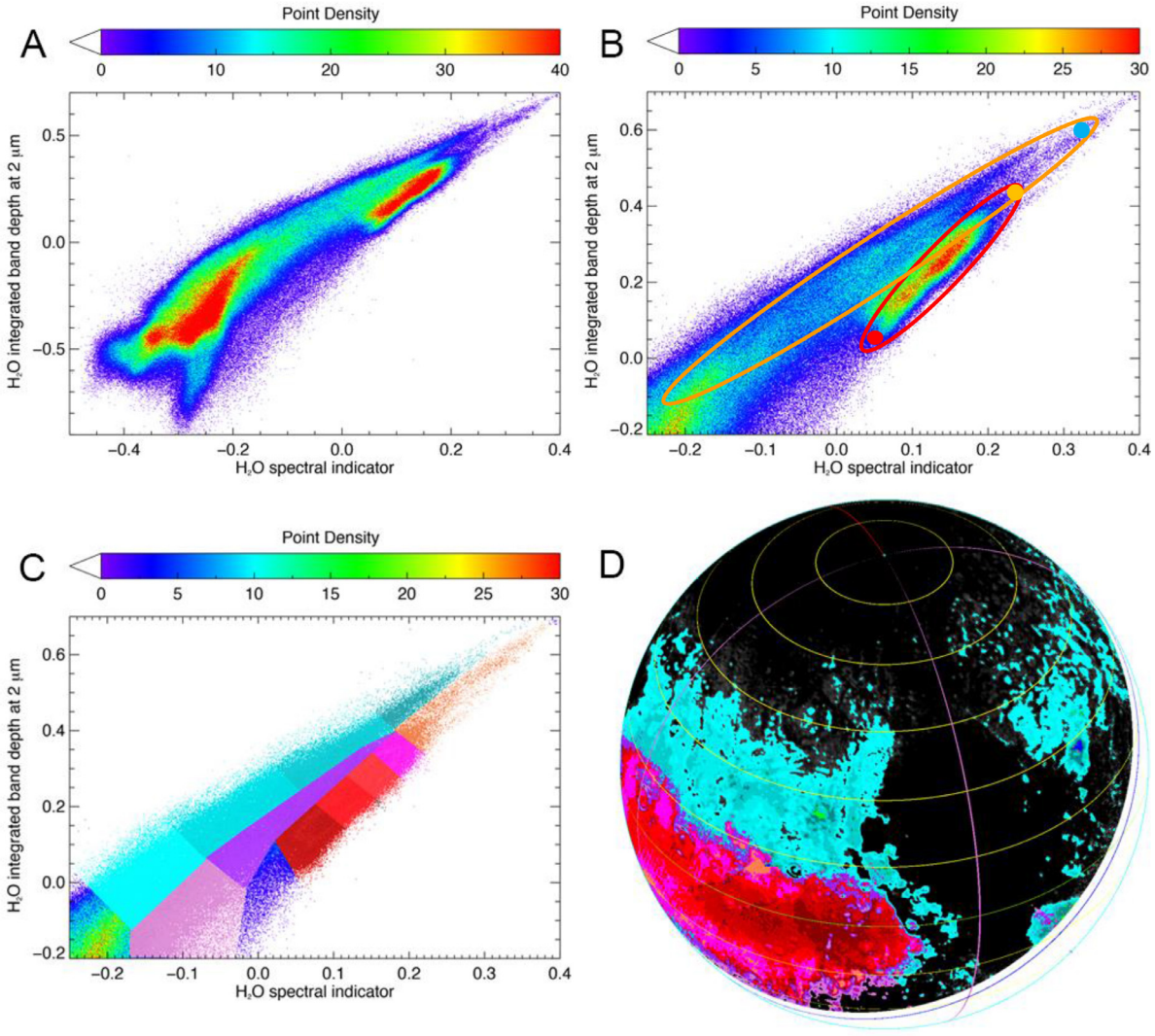

Fig. 31. The H2O end-members and their mixing lines. (A) Scatter plot of the H2O spectral indicator (Fig. 30A) versus the 2 µm H2O band depth (Fig. 28C). (B) Zoom of this scatter plot in the domain of water ice and red material. Orange ellipse: Mixing line 'water ice - CH4-containing ices'. Red ellipse: Mixing line 'water ice – red material'. Red dot: 'central *Cthulhu Regio*' red material end-member. Blue dot: '*Pulfrich crater* area' H2O end-member. Orange dot: '*Virgil Fossa*' intermediate 'dirty H2O' end-member. (C) Map of the distribution of the materials sampled by the classes defined along the mixing lines in the scatter plot (zoom) (D): Blue to Cyan: Mixing line 'water ice - CH4-containing ices'; Orange to dark red: Mixing line 'water ice – red material'. (For interpretation of the references to colour in this figure legend, the reader is referred to the web version of this article.)

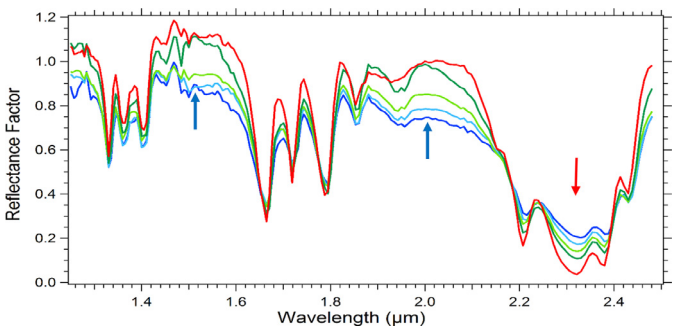

Fig. 32. Series of LEISA spectra with increasing values of REFF at 2.32 µm (red arrow) and corresponding increase of the H2O ice spectral indicator (from dark green to dark blue the indicator varies from −0.25 to −0.05). The spectra clearly display increasing absorptions at 1.5 and 2 µm due to H2O ice (blue arrows). With identical reflectance levels at 1.90 and 2.00 µm the dark green spectrum can be considered as almost H2O ice free. The red spectrum is a 'pure' N2-rich ice reference displaying a typical low reflectance at 2.32 µm (0.035). (For interpretation of the references to colour in this figure legend, the reader is referred to the web version of this article.)

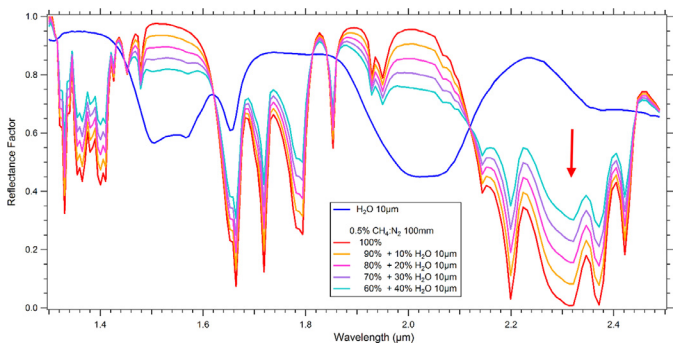

Fig. 33. Radiative transfer simulations (Douté et al., 1999 model), convolved at LEISA spectral resolution and sampling, of very large grained (100 mm) N2-rich ice (with 0.5% CH4) spatially mixed with increasing amounts of fine grained H2O ice (grain size 10 µm, blue spectrum). A strong increase of the reflectance can be obtained at 2.32 µm (red arrow) while keeping the spectral signature of H2O ice undetectable. Similar results are obtained for CH4-rich ices and for H2O ice grain sizes up to 50 µm (but resulting in a weaker reflectance increase at 2.32 µm). (For interpretation of the references to colour in this figure legend, the reader is referred to the web version of this article.)

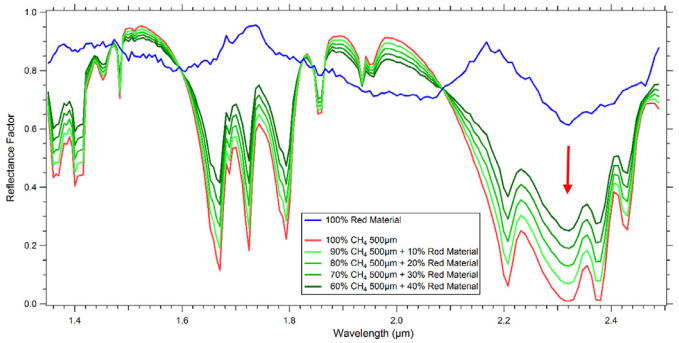

Fig. 34. Same as Fig. 33 but for medium grained (500 μm) CH4 ice spatially mixed with increasing amounts of red material (blue spectrum taken from the center of *Cthulhu Regio*). A strong increase of the reflectance can be obtained at 2.32 μm (red arrow) while keeping the spectral signature of the red material undetectable. Similar results are obtained for N2-rich ices. (For interpretation of the references to colour in this figure legend, the reader is referred to the web version of this article.)

spectral indicator as a function of the visible slope determined from the MVIC channels (Grundy et al., 2016). Fig. 35 displays two trends for moderately negative values of the H2O spectral indicator: one with markedly blue visible slopes (red ellipse) that remotely connect with the H2O end-member of the *Pulfrich Crater* area (dark blue circle), and the second with slightly bluish slope (grey ellipse) along the neutral slope line (vertical black line) that continue down to the highest negative values of the spectral indicator. The first group mostly covers *Hayabusa* and *Pioneer Terra* but also small spots in *Tartarus Dorsa*, while the second is concentrated in *Venera Terra, Burney crater*, Voyager Terra and in part of *Lowell Regio* around 60–80°N Lat. (Fig. 35B).

In Fig. 35A the first connecting line (light blue), that can account for most values with marked blue slope, appears to be a mixing line that connects the purest H2O ice found (around *Pulfrich Crater*) and the purest CH4-containing ice. We can set a conservative minimum threshold (−0.25) to our 'H2O spectral indicator' above which the presence of very fine grained H2O ice mixed with CH4-containing ice is very probable. To be fully conservative we also filtered all the pixels with a MVIC blue slope smaller than 2 (slope > -2), in addition to filtering all the positive (red) slopes (for negative values of the H2O indicator only). The map of distribution of H2O ice filtered with these values is presented in Fig. 30B. It shows a wide contribution of water ice over most of *Hayabusa* and *Pioneer Terra*, with possibly smaller amounts in *Tartarus Dorsa*.

The second line (grey ellipse) with almost constant small bluish slope may be attributed to the intrinsic weakly bluish slope of CH4-containing ices. However to explain the moderately negative values of the spectral indicator within the red ellipse in Fig. 35A, as well as the correlated increase in reflectance at 2.32 μm, some amount of red material and/or H2O ice and/or another material should be needed. This is consistent with the observation that all these area are close to red terrains and display a progressive gradient from red material-free area to contaminated ones.

Fig. 35B, displaying a classification of Pluto's surface according to visible slope and H2O spectral indicator, shows that the terrains containing water ice but no red material (blue tints) are mostly localized E and NE of *Sputnik Planitia*, while the slightly bluish/neutral terrains (yellow-green) composed only by 'clean' CH4-containing ices cover a large part of the N hemisphere above about 40°N as well as the E and S parts of *Sputnik Planitia*. The terrains composed of red material (dark red) and of CH4 or H2O ices strongly-to-moderately contaminated by red material (red-magenta) are mostly located on the west part of the equatorial and tropical regions at latitudes <40°N. Some faintly red, contaminated CH4-rich and N2-rich ices (orange) are located in the N polar region and in the western part of *Sputnik Planitia*, respectively. These two later types of terrain will be addressed in the following section.

The puzzling question is why this water ice only occurs here and with a positive correlation at local scale with the presence of N2-rich ice. However from this spectral indicator study we cannot detect small amount of water ice if mixed with red material. When mixed with red material we are mostly sensitive to large amounts of water ice, i.e. with a water ice spectral indicator larger than 0.4 (Fig. 35A). It is possibly why we detected these small ice amounts only on the East side, far from the red material.

4.7. The red material

One important question about the red material is to understand which type(s) of material is present, where, how and in which amount they are mixed with the ices at the surface of Pluto. The 'dark red material', first evidenced from ground observations in visible spectra (see review by Cruikshank et al., 2015) and now at high spatial resolution in the New Horizons images (Grundy et al., 2016) of the MVIC multispectral imager of the Ralph instrument (Reuter et al., 2008), is not so evidently seen in the near-infrared range. Indeed the areas (like *Cthulhu Regio*) where high concentration of this dark red material is observed in the visible are rather bright at most near infrared wavelengths (reflectance factor around 0.7–0.9) and slightly bluish (Figs. 4A, 27, 29). In addition, contrary to the visible range, there is no near-IR wavelength where this material is brighter or darker than all the other Pluto materials (H2O ice and CH4-containing ices) making it not easy to be detected in this spectral range. Note that in the following we will continue to call it the 'red' material, despite its near-IR spectral properties.

From the series of spectra extracted along the H2O - red material mixing line found in Fig. 31 we defined an optimized 'red material' spectral indicator that best separate it from both H2O and CH4-containing ices (Fig. 27).

The extracted spectra display several broad and moderately deep features, but at this stage of the calibration process of the data these features are still highly uncertain and appear to be significantly different in the alternative flat field calibration available (flat 4x). However for our aim we only need to found two wavelengths at which this material behaves differently, in a relative manner, from H2O ice and CH4-containing ices, so the ratio will be mostly flat field independent. At 1.430 and 1.658 μm the 'dark red' material has similar reflectance levels contrary to water ice and CH4-containing ices which both have a high continuum and a strong absorption band at these wavelengths, respectively.

The spectral indicator (SI) for the red material has thus been defined as:

$$\mathrm{SI(RedMat)} = 1 - \frac{\sum_{1.421\mu m}^{1.447\mu m}(RF)}{\sum_{1.641\mu m}^{1.670\mu m}(RF)} \quad (5)$$

The map of the relative reflectance between these two wavelengths (spectrally averaged over 6 spectels) is plotted in Fig. 36A and compared with the maps of the Visible slope derived from the MVIC BLUE, RED and NIR channels (Grundy et al., 2016).

These maps are globally similar below 45°N and 180°E (lower left of images) but, as for the H2O ice indicator, it was impossible to define a spectral indicator that fully separate H2O ice and the red material. Compared to our previously defined H2O ice indicator the red material indicator mostly inverts the order of these materials, thus clearly separating only the area with the largest abundance of red material. The map in Fig. 36A depicts the presence of red material either as pure material, spatially mixed

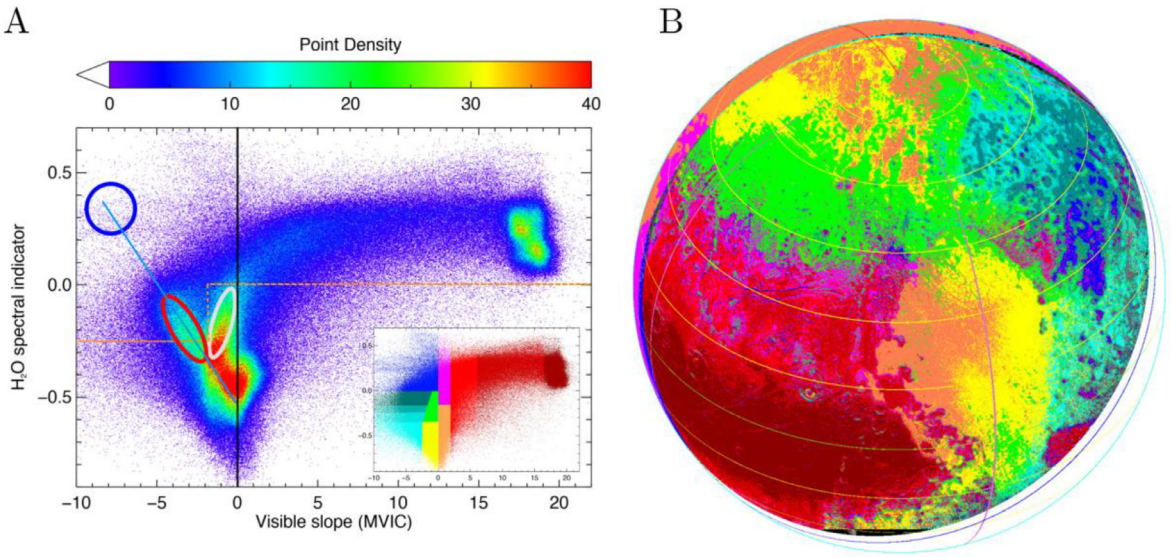

Fig. 35. (a) Correlation plot of our H2O spectral indicator versus the visible slope determined from MVIC channels (Grundy et al., 2016). The black vertical line divides MVIC slopes from blue (left) to red (right). The red ellipse shows the markedly bluish pixels that mostly covers *Hayabusa* and *Pioneer Terra*. The blue circle and light blue line show the location of the H2O *Pulfrich crater* endmember and the mixing line with CH4-containing ices. The orange horizontal and vertical dotted lines respectively mark the conservative sensitivity and slope threshold values set for our H2O spectral indicator (see text). The grey ellipse shows the intrinsic weakly bluish slope of CH4-containing ices. (b) Map of the distribution of the materials sampled by the classes defined in the insert of the scatter plot: orange to red are classes for the red terrains with increasing amount of red material. Dark to light blue are for red material-free H2O-containing terrains, with decreasing water contribution. Yellow and green for the neutral H2O-free and red material-free terrains. (For interpretation of the references to colour in this figure legend, the reader is referred to the web version of this article.)

or included in water or CH4-containing ices. The materials, H2O ices or CH4-containing ices, which did not contain red material should again be separated thanks to the MVIC visible slope.

In Fig. 37 by comparing our red material spectral indicator with the MVIC Visible spectral slope we found a good correlation (red line) over most of the range of the red slope, except for the lowest almost constant positives values. This witness either a change of mixing mode or another type of (less ?) red material as suggested by the two separate mixing lines present in the MVIC NIR/RED versus RED/BLUE color ratios plot (Fig. 4B in Grundy et al., 2016). We set a threshold (−1.3) in our red material indicator that separates the upper range of 'red material' and the lower one that we call the faint 'red material'. The qualitative distribution map of the red and faint red terrains is drawn in Fig. 35B together with the H2O-dominated and H2O-mixed terrains and the 'red material-free and H2O-free' CH4-containing icy terrains. Their classification, based on the H2O indicator, is given in the insert of Fig. 35A.

5. Data interpretation

All the material band depths, and especially the spectral indicators defined in this paper, are mostly qualitative and cannot provide the absolute or relative abundances of each material because, for example, grain size modulates the penetration depth of the light in different ways for each material depending on their absorption coefficient and mixing mode, and thus the effective amount of each material probed. However in some cases they can provide some clear information on the mixing mode, in particular for the state of CH4 and N2 mixed in molecular crystals (see part 4.4), and give additionally some hints on the other levels of mixing (spatial, intimate, layered). Also, in some special cases, the abundance ratio between two molecules is well represented by the band depth ratio, as for the CO/CH4 ratio in N2-rich ice, where they are both mixed at the molecular level within the same grains or crystals.

Radiative transfer modeling within the surface materials is necessary for effectively retrieving the relative amount of each materials and their texture (grain size,...). However, better is the knowledge of the components presents and their probable mixing modes at a given place (i.e. the surface representation), more efficient will be the inversion and more accurate the model results. On the other side a first global modeling, with an unique and simple surface representation for all Pluto, as reported in Protopapa et al. (2017), provides very useful and complementary constraints on the absolute abundances, textures and possible mixing modes of different areas on Pluto. The merging of these information will be the next step towards finer local composition maps of Pluto's surface.

But before it is necessary to further analyze the mixing lines between the various major materials of Pluto in order to better understand their mixing modes and the microphysical process that may produce them.

5.1. The mixing lines

In the previous parts, we presented the analysis of the occurrence of the different principal materials present on the surface of Pluto, i.e. N2-rich:CH4:CO, CH4-rich, and H2O ices as well as the red material(s), using specific spectral indicators and their correlations. These indicators and their combinations provided high Signal-to-Noise qualitative distribution maps of the materials after a number of bias have been understood.

These results will now be combined to assess in more details the state and degree of mixing of all these components using some specific correlations that best display the mixing lines of these materials and their end-members. The most important mixing lines are:

- red material – H2O ice
- CH4-containing ices – red material
- CH4-containing ices – H2O ice
- CH4-rich – N2-rich ices
- CO in N2-rich ice

5.1.1. General view of the mixing lines

The correlation plot in Fig. 31 (SI-H2O versus the 2 μm H2O band depth) very clearly displays both the H2O ice – red material

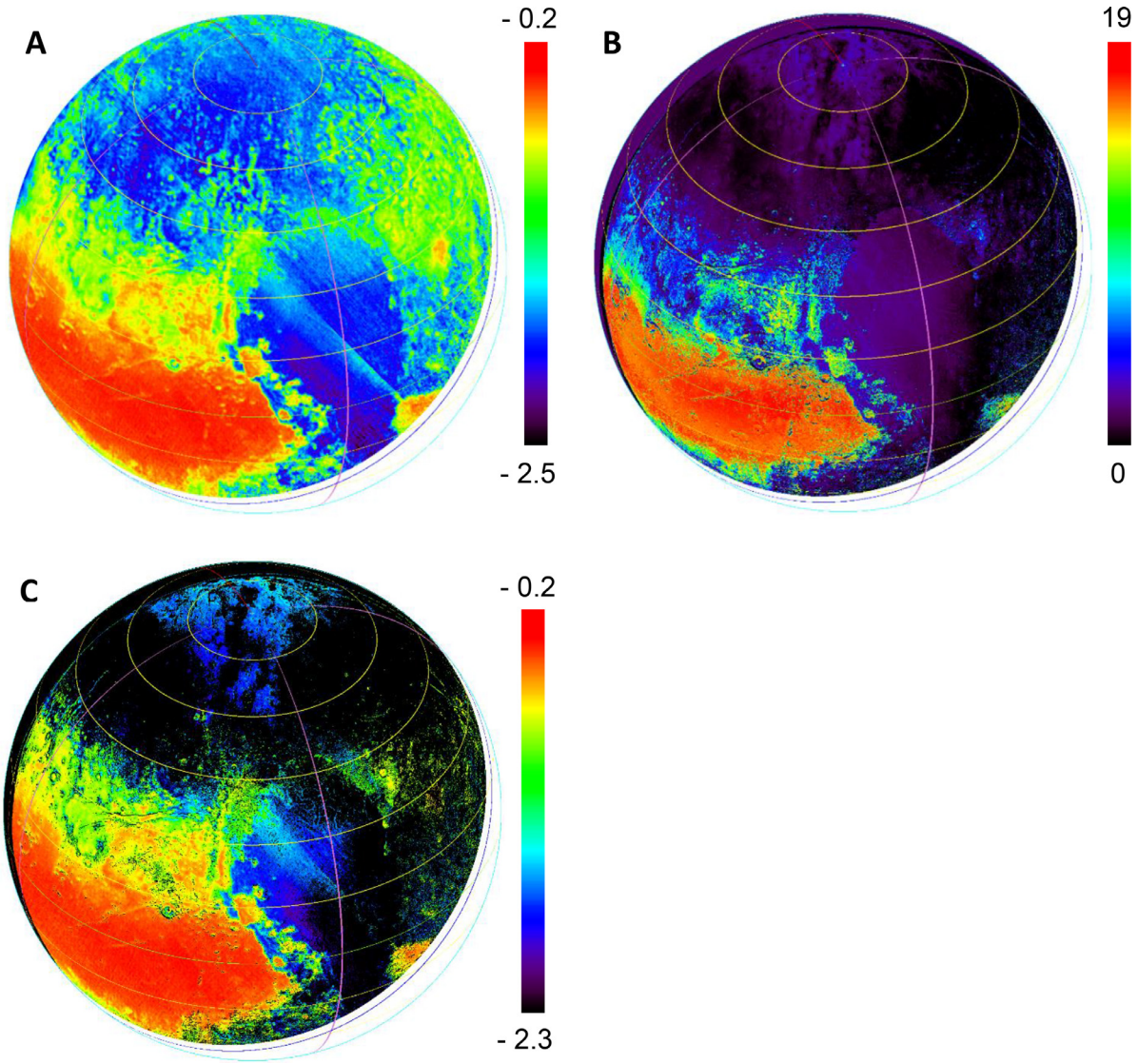

Fig. 36. Red material. Comparison between: (A) the map of the raw spectral indicator of the dark red material, and (B) the distribution of the visible red (positive) slope derived from MVIC channels (adapted from Grundy et al., 2016). (C) Spectral indicator of the red/red materials filtered for positive (red) MVIC visible slope. From low-to-high values: blue tints are for the 'faint red material' (below the threshold, see text) and green-to-red is for the 'red material' (above the threshold). (For interpretation of the references to colour in this figure legend, the reader is referred to the web version of this article.)

and the H2O ice – CH4-containig ices mixing lines and, in addition, separates the purest CH4-rich and N2-rich ices. It also show a weak but clear mixing line between red material and N2-rich ice. The spatial distribution of the classes defined along these mixing lines in the correlation plot (Fig. 38B) are reported on the map in Fig. 38A. This map well complement the one determined from the correlation of this same H2O ice spectral indicator with the MVIC slope (Fig. 35B).

5.1.2. The red material – H2O ice mixing line

This mixing line between the red material and H2O ice (Fig. 31A, Fig. 38A) is progressive and continuous from the red material end-member, that seems to contain no visible trace of water ice (pure end-member), to the '*Pulfrich Crater* H2O ice' end-member that appears to contain no red material (blue visible slope). All the pixels along *Virgil Fossa* are situated on this mixing line on the side close to the H2O end-member. The medium value of the reflectance factor at continuum wavelengths near 1.4 µm (~0.85), similar to the one of the red material (Fig. 27), confirms that this H2O ice 'relative end-member' is partly mixed, possibly intimately or as an optically thin surface layer, with small amount of red material. The close spatial proximity with *Cthulhu Regio* explains this contamination. Grundy et al. (2016) also observed that most of the strong H2O absorptions are associated with a small red coloration, as seen from MVIC blue channel. Radiative transfer modeling seems to confirm this contamination (Protopapa et al., 2017). This mixing line appears as a spatial mixing of two non-volatile components (at the surface temperature of Pluto), probably one, the red material, covering the other, H2O ice, mostly with an optically thick layer as expected from the atmospheric production of this organic material (currently about 2 mm/My; Gladstone et al., 2016). On the other hand the true H2O end-member near *Pulfrich Crater* and its surrounding have no nearby large area of red material. Its greater purity, apparently without noticeable trace of red material can be either explained by the absence of transport of red material at this distance from the main equatorial sources or more probably, by a recent geological process that exposed fresh water ice to the surface (Cook et al., 2017, submitted)

On the other side of the mixing line the occurrence of progressively decreasing amount of H2O ice along the S,W and N fringes of *Cthulhu Regio*, covered with red material, towards its interior and eastern part, where little water ice is detected (Fig. 30), tends

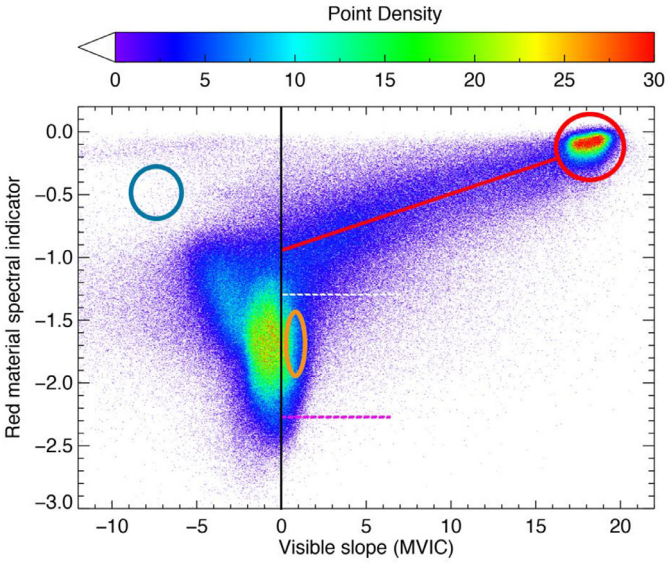

Fig. 37. Correlation plot of our red material spectral indicator with the visible slope determined from MVIC data (Grundy et al., 2016). The black vertical line divide MVIC slopes from blue (left) to red (right). The horizontal dotted line (white) is the threshold set for our red material spectral indicator between 'red material' and faint 'red material'. The red circle and line show the accumulation of red material in *Cthulhu Regio* and its mixing line with ices. Orange ellipse: faint red material in North polar region and NW of *Sputnik Planitia*. Blue circle: *Pulfrich crater* H2O ice. (For interpretation of the references to colour in this figure legend, the reader is referred to the web version of this article.)

to suggest that the thickness of the layer of organic material should not be very large (it reveals water ice at small spatial scale, cm to m, thanks to the micro topography), or that there is a process that need to remove it almost fully at some places almost everywhere on *Cthulhu Regio* and make it patchy at a few kilometers scale or below. The progressive gradient of mixing between H2O ice and the organic material favors a thin homogeneous layer (above km scale) with increasing average thickness from the fringe to the center of *Cthulhu Regio*. A competition between deposition and some burying process (in H2O ice ?) should be at work along this abundance gradient. Higher spatial resolution data such as LORRI and MVIC images, and knowledge of the topography of this region is needed to provide additional clues on the thickness of these deposits.

5.1.3. CH4-containing ice – red material mixing line

Fig. 38 (and Fig. 31) shows only a weak, but clearly separated mixing line (dashed line, pale violet color) between the red material and N2-rich-CH4-containing ices, without water ice. This mixing mostly occurs south of *Cthulhu Regio* at the limit of the southern polar night, and in a limited number of spots of N2-rich ice inside *Cthulhu Regio*, in particular in its E part and along the two giant craters (Oort and Edgeworth) in the W part (Fig. 38A). On the N fringe of *Cthulhu Regio* there is also a mixing line between dirty water ice and CH4-containing ices (purple). On the other hand a very sharp transition between the red non-volatile material and CH4-containing ices, with only very little red material (Fig. 35), is observed in particular at the Eastern boundary of *Viking Terra*. This point out an exclusion process which may originate from the higher temperature reached by the dark-red material (lower visible albedo and non-volatile) that should lead to the fast sublimation of any CH4-rich or N2-rich ices possibly condensed on it during the night or the long polar night (southern polar regions). From the scatter plot in Fig. 38 mixing between CH4 ices and red material seems to occur only when there is already substantial amount of colder H2O ice spatially mixed with the red material, so probably CH4-containing ices only condense on relatively clean water ice and almost never on optically thick layers of dark material.

However red material can be present with N2-rich ice in *Sputnik Planitia* and with CH4-rich ice in the N polar region (*Lowell Regio*) as seen on the correlation plot with MVIC, Fig. 35 (red area (orange) adjacent to zones with neutral slopes (yellow and green)). The shape of the red 'pollution' on *Sputnik Planitia* looks like wind-blown material from *Cthulhu Regio*, so it is most probably a very thin layer of dispersed red material on top of the N2-rich ice. On the other hand in the N polar region the red material has no obvious local source, but its location is very well correlated with

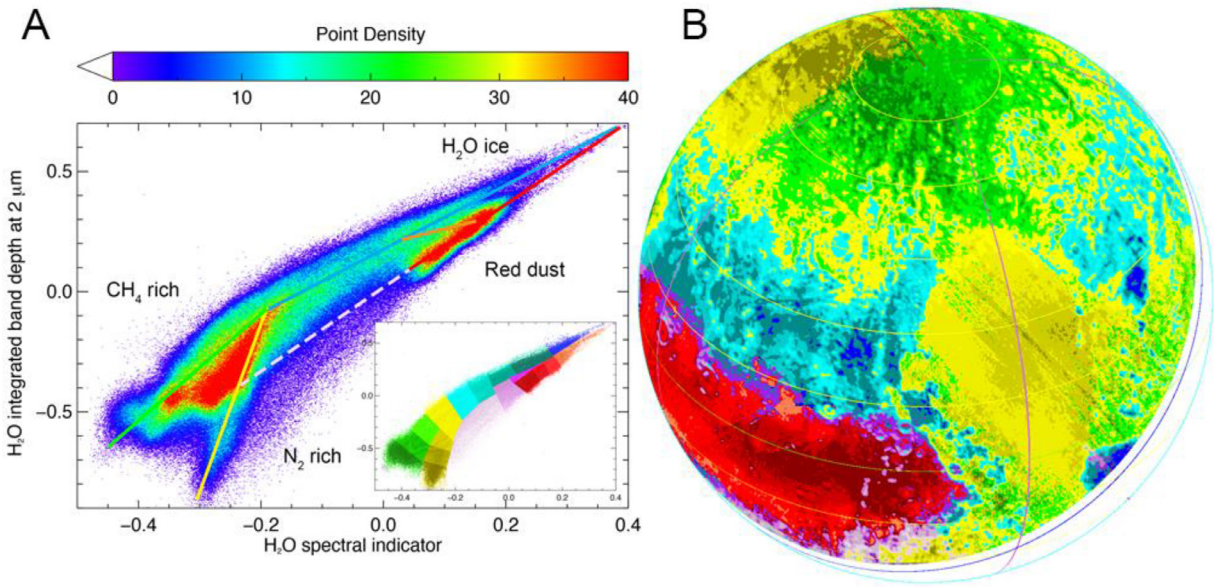

Fig. 38. 'H2O ice - red material' and 'H2O ice - CH4-containing ices' mixing lines. (A) Mixing lines: scatter plot of the H2O spectral indicator versus the integrated depth of the 2 µm H2O band (Fig. 31). See text. B) Distribution map of the classes defined along the mixing lines in the insert of 'A'. (For interpretation of the references to colour in this figure legend, the reader is referred to the web version of this article.)

CH4-rich ice. And is anti-correlated with the presence of N2-rich ice. This raise questions about its origin: is it organic material segregated and concentrated at the surface during sublimation of N2 ice leaving only CH4-rich ice mixed at some level with this material? Or this organic material is formed in-situ in the top layers by irradiation of CH4-rich ice, which can be dissociated (Cruz-Diaz et al., 2014) by the small amount of VUV radiation (in the 130–145 nm range) that may reach the surface through Pluto's atmosphere (Gladstone et al., 2016), in particular at seasons with low atmospheric pressure. On the other hand, the very low concentration of CH4 (<1%) contained in N2-rich ice can preclude its efficient photolysis and reaction with other CH4 molecules. The amount of organic material in the *North Polar Region* should be very small as it induces no detectable change in the reflectance level of the saturated CH4 band at 2.32 µm and no visible change in the near-IR continuum level and slope.

5.1.4. The CH4-containing ices – H2O ice mixing line

A very interesting feature displayed by the correlation plots is that there are two relatively separated mixing lines of CH4-containing ice with H2O ice on two distinct parts of Pluto: The first, with relatively clean H2O ice, is evidenced by the mixing line connecting CH4 ices with the bluish *Pulfrich* end-member (light blue line in Fig. 35) and that, except this end-member, has mostly low H2O fractional abundance of H2O ice (blue ellipse in Fig. 35). This mixing almost exclusively occurs on the eastern part of Pluto. Here the occurrence of H2O ice is partly correlated with the presence of N2-rich ice, at the local scale. But it is generally absent in pixels where CH4-rich ice is present. A possible explanation is that H2O ice is seen through or nearby relatively thin and transparent local deposits of very large grained (>20 cm) and CH4-poor N2-rich ices, as evidenced in Fig. 18. The geology and topography of this area being very complex, strong variations of slopes and altitudes are expected at local scale.

The other type of mixing is with dirty H2O ice occurring principally on the NW part of the encounter face of Pluto. It also contributes to the CH4 side of the main mixing line in Fig. 38 (blue line) but then diverges towards very dirty H2O ice (orange line in Fig. 38B). This last branch mostly occurs along the fringe of *Cthulhu Regio* (violet in Fig. 38A) where mostly CH4-rich ice is present (Figs. 20 and 39).

Given the strong difference in volatility with H2O ice this seems to tell that both CH4-rich ice and N2-rich ices can be spatially segregated at the pixel level with the water ice bedrock. In the area covered with red material these ices probably preferably condense (and/or sublimate more slowly) on slightly dirty water ice than on hotter dirtier area. Correlation with slopes and orientation, coupled with the global albedo of ices should tell more about the thermal conditions necessary to condense CH4-containing ices.

5.1.5. The CH4-rich – N2-rich ices mixing line

The particular transition occurring from N2-rich ice to CH4-rich ice in the correlation plot of the 2.15 µm N2 ice band depth versus the CH4 band positions index (Fig. 22) points to an evolution process that transforms one type of ice to another and involving a progressive change of the relative abundance of N2-rich and CH4-rich ice phases (either intimately mixed, layered or spatially distributed at sub-pixel level) probed by sun light.

The large scale spatial distribution of the materials between these two end-members (Fig. 39) displays progressive transitions but with a quite complex pattern, only partly following a latitude trend. Indeed from N pole to equator the composition globally changes from CH4-rich ice in the *N Polar Region* (down to ~65–70°N) to N2-rich dominated terrains down around about 35°N, but then reverse towards CH4-rich ice (except in *Sputnik Planitia*) until the limit of the large *Cthulhu Regio* area dominated by dark-red material on the W side, and below the *Pulfrich Crater* area on the E side of *Tombaugh Regio*. Finally N2-rich ice, spatially intermixed with CH4-rich ice, reappears south of both these geological terrains. These southernmost areas correspond to places where CH4-rich ice occurs locally (Fig. 20) with very large grains (Protopapa et al., 2017) and with large CO/CH4 ratios (Fig. 26B).

5.1.6. CO molecular mixing in N2-rich ice

A close look at one of these regions shows that the location of the spots with high CO/CH4 band depth ratio (red-yellow-green in Fig. 40B) always corresponds to N2-rich area (dark-to-light brown in Fig. 40A), as determined from the CH4 bands position. They is also generally a gradient of CO from high CO/CH4 in N2-rich area to low CO/CH4 (blue in Fig. 40B) where both N2-rich and CH4-rich phases are mixed (yellow in Fig. 40A), and then to no detectable CO (black in Fig. 40B) in area dominated by CH4-rich ice (green in Fig. 40A).

In fact when the volatile ice change from N2-rich phase to CH4-rich phase the CO/CH4 band depth ratio decreases by at least a factor of 5 (with our conservative CO detection threshold) thus pointing to a massive loss of CO when N2 sublimates.

5.2. The sublimation and differentiation of N2:CO:CH4 ices

Considering the global and local scale transitions of the ices, from N2-rich to CH4-rich (Fig. 39) and from high to low values of CO/CH4 (Fig. 26) it appears that a fractionation of N2, CO and CH4 occurs when the N2-rich: CO: CH4 molecular mixture ice sublimate.

Due to the large difference in volatility between N2, CO and CH4 (vapor pressure ratios: N2/CO/CH4 = 8000/1000/1 at 40 K, Fray and Schmitt, 2009) the most probable process is the progressive sublimation of N2, and to a lower extent CO, from N2-rich: CH4: CO mixtures leading to a concentration of CH4, and also partly of CO, in N2-rich ice up to the saturation of CH4 (5% CH4 in N2 at 40 K). Given the lower average abundance of CO on Pluto, 0.1–0.2%, compared to CH4 (~0.5%) (Douté et al., 1999), its much higher volatility and higher saturation level in beta-N2 ice (12% compared to 5% at 40 K), there is a good probability that CH4 saturates in N2 before CO does, and thus forms a N2-rich:CO:CH4 – CH4-rich:CO:N2 binary phase mixture at the surface of the single phase N2-rich ice layer instead of an alpha-CO-rich:N2: CH4 phase (Prokhvatilov and Yantsevich, 1983; Angwin and Wasserman, 1966; Veter et al., 2007. However the ternary phase diagram of N2:CO:CH4 as well as the binary phase diagram of CO:CH4 are unknown, thus the exact phase changes that may occur in such situations are still very uncertain. In particular upon further sublimation the N2-rich:CO:CH4 ice phase will disappear in favor of the CH4-rich:CO:N2 phase. The amount of N2 that can be trapped in CH4 ice at 40 K is only 3.5% (but higher at higher temperature), but the fraction of CO at saturation in CH4 ice is unknown. However the observations show that CO is rarely detectable when CH4-rich ice dominates the spectral signature of the pixel. Indeed, there is only 2% of the pixels that have both a CH4 band position index >42 (dominant CH4-rich ice) and a CO band depth above its detection threshold (0.005). These pixels are mostly distributed in SW and E *Tombaugh Regio* in area where CH4-rich ice occurs in many small spotty places. As these pixels mostly lies at the border of these small CH4 ice spots, and never in the center of CH4 ice spots larger than a few pixels wide (these pixels oversample by a factor of about 3 the true instrument spatial resolution), a sub-pixel mixing of CH4-rich and N2-rich:CH4:CO ices is strongly suspected. In the center of the CH4-rich ice deposits of the *North Polar Region* the proportion of such pixels drops to 0.6%, mainly located along small patches of N2-rich ice.

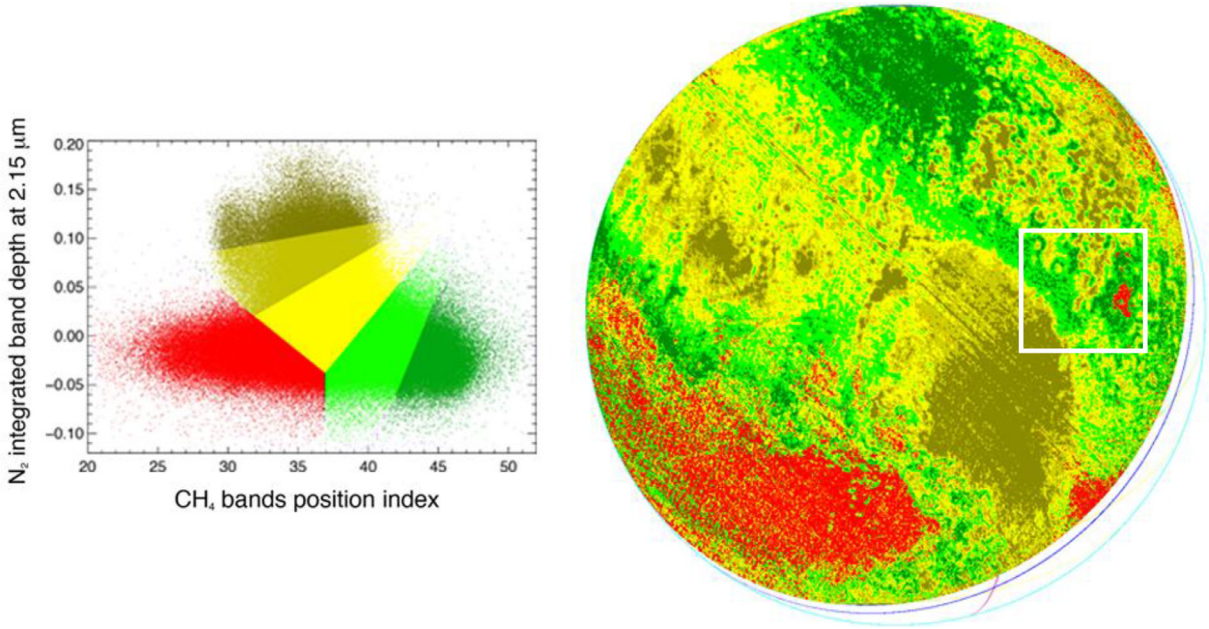

Fig. 39. Spatial distribution of the N2-rich and CH4-rich terrains and their progressive transition based on the correlation plot of the integrated N2 ice band depth at 2.15 µm versus the CH4 band positions index (Fig. 22). The map shows the distribution of the materials sampled by the 6 classes defined in the insert of Fig. 22, and enlarged here: 'brown-yellow-green' for areas with composition ranging from N2-rich ice (brown) to CH4-rich ice (dark green). 'Red' corresponds to area fully devoid in CH4 and N2 ices (red material and H2O ice). The white square box shows the zoom extent displayed in Fig. 40. (For interpretation of the references to colour in this figure legend, the reader is referred to the web version of this article.)

These phases segregated during N2 (+CO) sublimation may either be intimately mixed in the upper layers, or they may form an upper CH4-rich ice crust as we demonstrated experimentally by sublimating N2-rich ice with diluted CH4 (0.2%) at 34 K (Stansberry et al., 1996). Such a segregation process may lead to the formation of a CH4-rich layer that may get optically thick at the wavelengths of the spectral signature (2.15 µm) of the underlying N2-rich ice. The strength of 2.15 µm N2 ice band being quite weak compared to that of CH4 ice at this same wavelength (Grundy et al., 1993, 2002) it is expected that a very thin layer, probably just a few tens of microns thick may hide the N2 ice signature, despite its presence below in large quantity. The existence of such a stratification over a large fraction of the surface (~70%) has been derived as one of the best solution to fit a 1995 ground based (UKIRT) Pluto spectrum with radiative transfer model (Douté et al., 1999). So, the detection of only the CH4-rich phase does not imply that a N2-rich phase is not present just below. If locally the thickness of the layer is not optically thick at all wavelengths then it may be possible to measure positions of the strongest CH4 bands consistent with CH4-rich ice but that of the weakest bands, such as the 1.937 + 1.955 µm doublet probing deeper the surface, closer to the positions of CH4 diluted in N2-rich ice. Otherwise, for thick layers, temperature measurements may witness the presence of remaining N2 ice. A temperature close to the sublimation temperature of N2-rich ice or lower than the equilibrium temperature of the CH4-rich phase should witness the hidden presence of N2-rich ice. A similar situation has been already observed for the northern seasonal condensates of Mars with another couple of volatile ices (at the temperature of Mars): H2O and CO2 (Appéré et al., 2011) with the latter also dominating the atmosphere and thus controlling the temperature of the CO2-rich ices at its equilibrium value. During sublimation of the intimate mixture of CO2-rich+H2O ices a segregation occurs and an upper crust of H2O ice grains develops up to the point to spectrally hide the underlying CO2 ice. But the temperature of the surface remains around 150 K, the equilibrium temperature of CO2 ice under the Martian pressure. This segregation process, as well as the associated spectral evolution in the near-infrared, have been simulated for the Martian conditions in the laboratory (Philippe et al., 2017).

The process is however different due to the fact that in the Martian seasonal condensates the H2O ice grains already exist intimately mixed with CO2 ice. On Pluto the progressive sublimation of N2 ice trigger the formation of a new CH4-rich phase from the progressive saturation of CH4 dissolved in N2-rich phase, evidenced by the CH4 band shifts and the apparition of the 1.69 µm band (Quirico and Schmitt, 1997a). This process thus first creates a two-phases intimate mixture (Prokhvatilov and Yantsevich, 1983) and finally a CH4-rich crust by fully removing the N2-rich phase, as evidenced in our laboratory simulations (Stansberry et al., 1996). For CO it is not possible to demonstrate spectroscopically its dilution state in N2-rich ice on Pluto because the shift upon mixing of the CO 1.58 µm band (0.0002 µm, Quirico and Schmitt, 1997b) is much too weak compared to the spectral resolution of LEISA (0.007 µm). However this shift has been recently observed for Triton using very high spectral resolution spectroscopy, thus confirming that CO is mostly diluted in N2 ice, and not as a CO-rich phase (Lellouch et al., 2014). The determination of the effective CO/CH4 ratio in N2-rich ices on Pluto and its evolution during sublimation will need radiative transfer simulations with relevant optical constants, i.e. for mixtures of CO and CH4 in N2 ice in relevant proportions. The modeling of ground based observations showed that this ratio was globally in the range 0.15–0.4 depending on the surface representation used. But locally we found that this ratio may change by more than a factor of 5 (Fig. 25) Laboratory experiments are clearly needed here. They should also determine the amount of CO that can be diluted in CH4 ice in the 40–60 K range as well as the shift of the CO band in CH4 ice and those of the CH4 bands with diluted CO. The first are probably negligible and the second small compared to the shift of CH4 diluted in N2-ice (relative to pure CH4 ice).

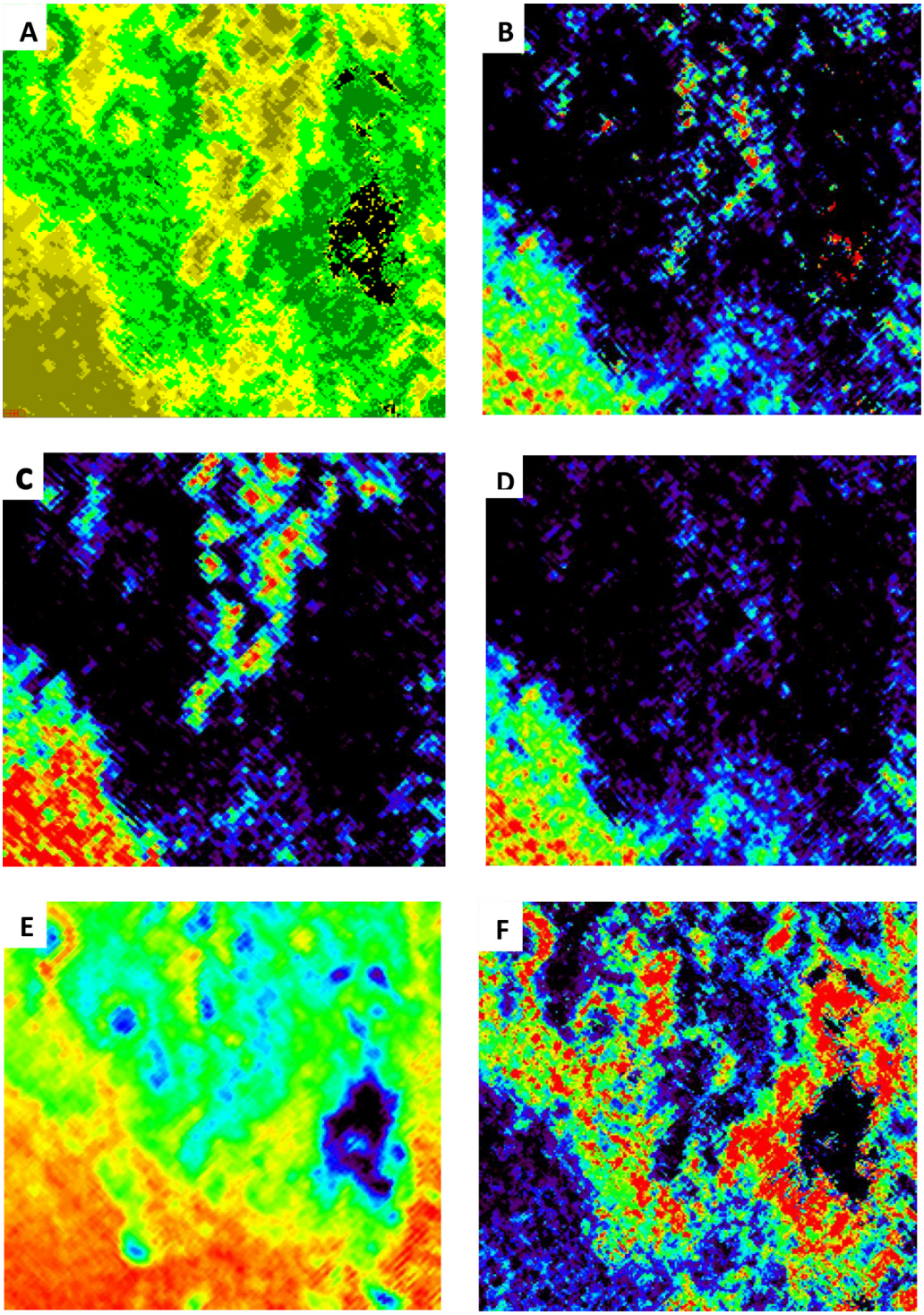

Fig. 40. Local comparison of the distributions of (A) N2-rich ice (brown to yellow) and CH4-rich ice (light to dark green) (Water ice in black, Fig. 39) with (B) the CO/CH4 ratio (Fig. 26A). The zoom area corresponds to the white square box in Fig. 39 East of *Sputnik Planitia* and including the *Pulfrich crater* area (center: ~30°N, 200°E). (C to F): zooms of the volatile maps over the same area: (C) N2 band depth (Fig. 15), (D) CO band depth (Fig. 24), (E) CH4 band depth (Fig. 13.2), and (F) CH4 band position index (Fig. 20). (For interpretation of the references to colour in this figure legend, the reader is referred to the web version of this article.)

5.3. Global sublimation of pluto's ices

The global distribution of the volatile ices on Pluto is peculiar, with two latitude bands of CH4-rich ices surrounding a latitude band of N2-rich ice between about 35 and 65°N, as described in some details in 5.1.5. Two different processes may explain this ices distribution.

At high latitudes the vigorous spring sublimation of N2 in the northern hemisphere is due to strong and constant solar illumination in the last 20 years, as proposed by Protopapa et al. (2017). The total flux received may have sublimated enough N2 ice either to remove all of this volatile molecule from the surface, down to the water ice bedrock or, more probably, to create a homogeneous optically thick upper crust of CH4-rich ice, that we currently

observe over most of the polar region. This crust may hide large expanse of N2-rich ice below, depending on the climatic history and whole inventory of N2 on Pluto. Temperature measurements in the mm range, to probe below this crust, at sufficiently high spatial resolution to resolve the polar region from ground based observations may solve this question.

In the tropical region (i.e. at all latitudes below the maximum sub-solar latitude, currently 57.5°), the increased N2 and CO sublimation may be the result of both the high diurnal illumination, as proposed by Protopapa et al. (2017), but boosted around the dark materials and H2O ice spots, on the W part of Pluto, by the lower albedo of the red material contaminated volatiles ices (or condensed on a darker surface).

So, on Pluto, a lag deposit of CH4-rich ice may form at places where all N2 ice sublimated and the spatial mixing line between CH4-rich ice and the H2O ice bedrock may be due to the final sublimation of this lag deposit. The major exception occurs around 180° longitude where the large and thick expanse of N2 ice of *Sputnik Planitia*, probably accumulated over hundreds of millions of years at the bottom of a large impact crater (Moore et al., 2016; Bertrand and Forget, 2016) interrupt the latitudinal transition.

6. Conclusion

6.1. Surface representation

The detailed analysis performed in this paper, using reduced noise data and various spectral indicators (including band depths and equivalent widths) and their correlations, allowed us to map the distributions and state of the four main materials present at the surface of Pluto:

- N2-rich ices containing CH4 and CO
- CH4-rich ices possibly containing small amounts of CO and N2
- H2O ice, mixed with various amounts of red material
- Dark-red material

It also allowed us to determine the mixing lines between them and their meaning in terms of surface representation and evolution processes that created them:

- *N2:CH4:CO molecular mixture*: CH4 is mixed at the molecular level with N2-rich ice. CO is most probably also mixed with N2 thus forming a ternary mixture that follows its phase diagram with solubility limits. At least a second phase CH4-rich:(CO:N2?) exists.
- *H2O ice – red material mixing line*: The mixing of the red material covering H2O ice mostly occurs on the NW part of the observed hemisphere. It is most probably spatial with possibly small amount intimately mixed.
- *CH4-containing ices – red material mixing line*: Two different area display such mixing with red material. With N2-rich:CH4:CO ice on *Sputnik Planitia*, with surficial red material probably transported by winds from *Cthulhu Regio*. And with CH4-rich:(CO:N2?) ice in the N polar region, possibly formed by photochemistry. Otherwise only very sharp transitions are observed between CH4-containing ices and this non-volatile materiel due to thermal incompatibility.
- *CH4-rich – N2-rich ices mixing line*: Created by differential sublimation, accompanied by a depletion in CO relative to CH4, that transform one type of ice phase to another, with an intermediate stage with both phases presents (as constrained by the CH4 bands index), leading to the formation of either a binary intimate mixture of N2-rich and CH4-rich phases at the surface (thermodynamic constraint) or/and an upper CH4-rich ice crust that may hide the N2-rich ice below (experimental constraint).
- *CH4-rich – H2O mixing line*: due to the sublimation of the CH4-rich:(CO:N2?) ice lag left behind by the sublimation of N2 (spring-summer), or direct condensation of CH4 ice on the cold, H2O ice (late autumn).

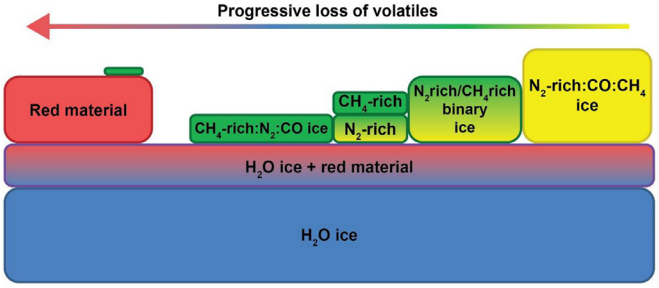

Fig. 41. Schematic representation of the various materials and their possible mixing states at the surface of Pluto upon progressive loss of volatiles. From right to left the materials contain less of the most volatile molecules, starting to lose N2, then CO, then CH4. N2-rich ice thus contains increasing amounts of CH4 (up to saturation) and possibly CO and start to form a binary mixture of N2-rich:CO:CH4 and CH4-rich:N2:CO phases. The CH4-rich ice crust and final lag deposit may still contain some small amount of CO and N2, but undetectable with LEISA.

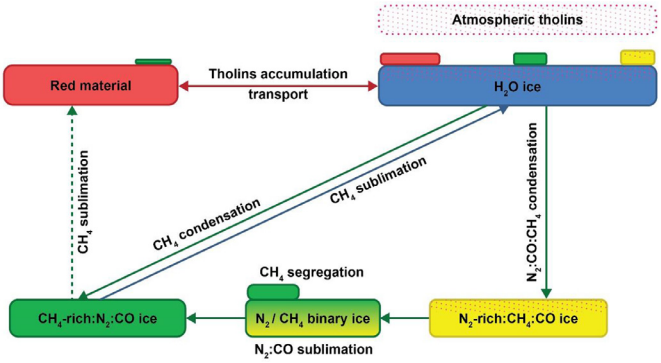

Fig. 42. Schematic representation of the evolution processes of the materials and their possible mixing at the surface of Pluto. See Fig. 41 for description of the ices.

All these mixing lines converge to H2O ice (Fig. 38) which allows us to propose (or confirm) that water ice is the bedrock that is partly covered by the different other constituents (red material, CH4-rich ice, N2-rich ice) in various proportions. It likely makes up the bulk of Pluto's mantle but due to the large amount of volatile material and organic material present at the surface of Pluto it emerges only in limited places, contrary to Triton (Cruikshank et al., 2000).

These results allow us to propose a surface representation (Fig. 41) of Pluto's materials in the current state of the surface, i.e. during spring in southern hemisphere, autumn in northern hemisphere as well as a global evolution scheme (Fig. 42).

A detailed spectral analysis and modeling of these transitions will be necessary when the absolute calibration of the data will be improved. In particular this is requisite to discriminate between the evolution of N2-rich ice toward either a binary intimate mixture of N2-rich and CH4-rich phases or an upper CH4-rich ice crust, or possibly both successively. The determination of the different relative abundances upon mixing will also require radiative transfer modeling of their spectra. A first quantitative analysis of the abundance and texture of the N2-rich: CH4 and CH4-rich:N2 materials by spectral modeling using an unique surface representation for the whole observed hemisphere is the central subject of the companion paper by Protopapa et al. (2017). It also addresses the quantification of H2O ice mixed with the CH4:N2 ices.

Our work will enable this modeling inversion and obtain more accurate abundance maps by providing better regional and local surface representations as well as constraints on the occurrence of the materials.

These results also raise a number of questions about the evolution processes of the surface of Pluto and will certainly help to constrain the climatic models that are trying to reproduce the current distribution and state of the volatiles as a result of sublimation-condensation and transport cycles.

The distribution maps, although still qualitative, will be of great interest for the study of Pluto's surface geomorphology and associated processes, thanks in particular to the noise reduction process we applied on the data that allowed us to obtain most of the composition maps with a spatial definition compatible with MVIC multi-spectral images and even some global LORRI images and their products. In particular global and local correlation of these maps with altitude, latitude, slope, orientation, daily illumination will allow to better understand the parameters that control the processes leading to the current distribution, physical state, mixing state and texture of the materials on Pluto.

Data references

[dataset] Grundy, W., Quirico, E., and Schmitt, B. NIR Optical constants spectra of beta-N2 crystal at 4 different temperatures. GhoSST / SSHADE database. 1992. https://sshade.eu/old-ghosst/experiment/EXPERIMENT_BS_20120925_003.

[dataset] Grundy, W., and Schmitt, B. NIR Optical constants spectrum of H2O liquid at 26 different temperatures (20–270 K). GhoSST / SSHADE database. 1997. https://sshade.eu/old-ghosst/experiment/ EXPERIMENT_BS_20,120,924_011.

[dataset] Grundy, W., Schmitt, B., and Trotta, F. Vis-NIR-MIR optical constants spectrum of crystalline CH4-I at 39 K. GhoSST / SSHADE database. 1995. https://sshade.eu/old-ghosst/experiment/EXPERIMENT_BS_20130219_003.

[dataset] Quirico, E., and Schmitt, B. NIR optical constant spectra of CH4 in solid solution in beta-N2 at 4 different temperatures (36.5 - 41 K). Version 3. GhoSST / SSHADE database. 1998a. https://sshade.eu/old-ghosst/experiment/EXPERIMENT_BS_20130103_003.

Acknowledgments

This work was supported by NASA's New Horizons Project. B. Schmitt, S. Philippe, R. Côte and E. Quirico acknowledge the Centre National d'Etudes Spatiales (CNES) for its financial support through its "Système Solaire" program. S. Protopapa gratefully thanks the NASA Grant and Cooperative Agreement for funding that supported this work (grant #NNX16AC83G). We acknowledge M. Gorbacheva for two illustrations of the paper and E. Lellouch and an anonymous referee for their very constructive reviews.

References

Alvarez-Candal, A., Pinilla-Alonso, N., Licandro, J., et al., 2011. The spectrum of (136199) Eris between 350 and 2350 nm: results with X-Shooter. Astron. Astrophys. 523 (A130), 8.

Angwin, M.J., Wasserman, J., 1966. Nitrogen–carbon monoxide phase diagram. J. Chem. Phys. 44, 417.

Appéré, T., Schmitt, B., Langevin, Y., Douté, S., Pommerol, A., Forget, F., Spiga, A., Gondet, B., Bibring, J.-P, 2011. Winter and spring evolution of Northern seasonal deposits on Mars from OMEGA/Mars Express. J. Geophys. Res. E. 116, E05001. doi:10.1029/2010JE003762.

Barucci, M.A., Dalle Ore, C.M., Perna, D., Cruikshank, D.P., Doressoundiram, A., Alvarez-Candal, A., Dotto, E., Nitschelm, C, 2015. (50000) Quaoar: surface composition variability. Astron. Astrophys. 584, A107.

Bertrand, T., Forget, F., 2016. Observed glacier and volatile distribution on Pluto from atmosphere–topography processes. Nature 540, 86–89.

Buie, M.W., Tholen, D.J., Horne, K., 1992. Albedo maps of Pluto and Charon: initial mutual event results. Icarus 97, 211–227.

Cook, J.C., Dalle Ore, C.M., Protopapa, S., Binzel, R., Cruikshank, D.P., Earle, A., Grundy, W.M., Ennico, K., Howett, C., Jennings, D., Lunsford, A.W., Olkin, C.B., Parker, A.H., Philippe, S., Reuter, D., Schmitt, B., Singer, K., Standsberry, J.A., Stern, S.A., Verbisher, A., Weaver, H.A., Young, L.A., Hanley, J., Alketbi, F., Thompson, G.L., Pearce, L.A., Lindberg, G.E., Tegler, S.C., 2017. The distribution of H2O, CH3OH and hydrocarbon-ices on Pluto: analysis of New Horizons spectral images. Icarus submitted.

Cruikshank, D.P., Pilcher, C.B., Morrison, D., 1976. Pluto: evidence for methane ice. Science 194, 835–837.

Cruikshank, D.P., Roush, T.L., Owen, T.C., Geballe, T.R., de Bergh, C., Schmitt, B., Brown, R.H., Bartholomew, M.J., 1993. Ices on the surface of Triton. Science 261, 742–745. doi:10.1126/science.261.5122.742.

Cruikshank, D.P., De Bergh, C., Douté, S., Geballe, T.R., Owen, T.C., Quirico, E., Roush, T.L., Schmitt, B., 1999. Ethane on Pluto? Science 285, 1355c. doi:10.1126/science.285.5432.1355c.

Cruikshank, D.P., Schmitt, B., Roush, T.L., Owen, T.C., Quirico, E., Geballe, T.R., de Bergh, C., Bartholomew, M.J., Dalle Ore, C., Douté, S., Meier, R., 2000. Water ice on Triton. Icarus 147, 309–316. doi:10.1006/icar.2000.6451.

Cruikshank, D.P., Mason, R.E., Dalle Ore, C.M., Bernstein, M.P., Quirico, E., Mastrapa, R.M., Emery, J.P., Owen, T.C., 2006. Ethane on Pluto and Triton. Bull. Am. Astron. Soc. 38, 518.

Cruikshank, D.P., Grundy, W.M., DeMeo, F.E., Buie, M.W., Binzel, R.P., Jennings, D.E., Olkin, C.B., Parker, J.W., Reuter, D.C., Spencer, J.R., Stern, S.A., Young, L.A., Weaver, H.A., 2015. The surface compositions of Pluto and Charon. Icarus 246, 82–92.

Cruz-Diaz, G.A., Muñoz Caro, G.M., Chen, Y.-J., Yih, T.-S., 2014. Vacuum-UV spectroscopy of interstellar ice analogs. II. Absorption cross-sections of nonpolar ice molecules. Astron. Astrophys. 562, A120.

Dalle Ore, C.Morea, Barucci, M.A., Emery, J.P., Cruikshank, D.P., Dalle Ore, L.V., Merlin, F., Alvarez-Candal, A., de Bergh, C., Trilling, D.E., Perna, D., Fornasier, S., Mastrapa, R.M.E., Dotto, E., 2009. Composition of KBO (50000) Quaoar. Astron. Astrophys. 501, 349–357.

DeMeo, F.E., Dumas, C., de Bergh, C., Protopapa, S., Cruikshank, D.P., Geballe, T.R., Alvarez-Candal, A., Merlin, F., Barucci, M.A., 2010. A search for ethane on Pluto and Triton. Icarus 208, 412–424.

Douté, S., Schmitt, B., 1998. A multi-layer bidirectional reflectance model for the analysis of planetary surface hyperspectral images at visible and near infrared wavelengths. J. Geophys. Res. E 103, 31367–31390. doi:10.1029/98JE01894.

Douté, S., Schmitt, B., Quirico, E., Owen, T.C., Cruikshank, D.P., de Bergh, C., Geballe, T.R., Roush, T.L., 1999. Evidence for methane segregation at the surface of Pluto. Icarus 142, 421–444. doi:10.1006/icar.1999.6226.

Fray, N., Schmitt, B., 2009. Sublimation of molecules of astrophysical interest. A bibliographic review. Planet. Space Sci 57, 2053–2080. doi:10.1016/j.pss.2009.09.011.

Gladstone, G.R., Stern, S.A., Ennico, K., Olkin, C.B., Weaver, HaroldA., Leslie, Young, A., Summers, MichaelE., Strobel, DarrellF., Hinson, DavidP., Kammer, JoshuaA., Parker, AlexH., Steffl, AndrewJ., Linscott, IvanR., Parker, JoelWm., Cheng, AndrewF., Slater†, DavidC., Versteeg, MaartenH., Greathouse, ThomasK., Retherford, KurtD., Throop, Henry, Cunningham, NathanielJ., Woods, WilliamW., Singer, KelsiN., Constantine, Tsang, C.C., Schindhelm, Eric, Lisse, CareyM., Wong, MichaelL., Yung, YukL., Zhu, Xun, Curdt, Werner, Lavvas, Panayotis, Young, EliotF., Tyler, G.Leonardthe New Horizons Science Team, 2016. The atmosphere of Pluto as observed by New Horizons. Science 351, 1280.

Grundy, W., Schmitt, B., Quirico, E., 1993. The temperature dependent spectra of α and β nitrogen ice with application to Triton. Icarus 105, 254–258. doi:10.1006/icar.1993.1122.

Grundy, W., Schmitt, B., 1998. The temperature-dependent near-infrared absorption spectrum of hexagonal H_2O ice. J. Geophys. Res. E 103, 25809–25822. doi:10.1029/98JE00738.

Grundy, W.M., Buie, M.W., 2001. Distribution and evolution of CH4, N2, and CO ices on Pluto's surface: 1995 to 1998. Icarus 153, 248–263.

Grundy, W.M., Buie, M.W., 2002. Spatial and compositional constraints on non-ice components and H2O on Pluto's surface. Icarus 157, 128–138.

Grundy, W., Schmitt, B., Quirico, E., 2002. The temperature-dependent spectrum of methane ice I between 0.7 and 5 μm and opportunities for near-infrared remote thermometry. Icarus 155, 486–496. doi:10.1006/icar.2001.6726.

Grundy, W.M., Young, L.A., Stansberry, J.A., Buie, M.W., Olkin, C.B., Young, E.F., 2010. Near-infrared spectral monitoring of Triton with IRTF/SpeX II: Spatial distribution and evolution of ices. Icarus 205, 594–604.

Grundy, W.M., Olkin, C.B., Young, L.A., Buie, M.W., Young, E.F., 2013. Near-infrared spectral monitoring of Pluto's ices: spatial distribution and secular evolution. Icarus 223, 710–721.

Grundy, W.M., Olkin, C.B., Young, L.A., Holler, B.J., 2014. Near-infrared spectral monitoring of Pluto's ices: recent decline of CO and N2 ice absorptions. Icarus 235, 220–224.

Grundy, W.M., Binzel, R.P., Buratti, B.J., Cook, J.C., Cruikshank, D.P., Dalle Ore, C.M., Earle, A.M., Ennico, K., Howett, C.J.A., Lunsford, A.W., Olkin, C.B., Parker, A.H., Philippe, S., Protopapa, S., Quirico, E., Reuter, D.C., Schmitt, B., Singer, K.N., Verbiscer, A.J., Beyer, R.A., Buie, M.W., Cheng, A.F., Jennings, D.E., Linscott, I.R., Parker, J.Wm., Schenk, P.M., Spencer, J.R., Stansberry, J.A., Stern, S.A., Throop, H.B., Tsang, C.C.C., Weaver, H.A., Weignle II, G.E., Young, L.A.the New Horizons Science Team, 2016. Surface compositions across Pluto and Charon. Science 351, 1283. aae0030 doi: 10.1126/science.aad9189.

Guilbert, A., et al., 2009. ESO-large program on TNOs: near-infrared spectroscopy with SINFONI. Icarus 201, 272–283.

Hapke, 2012. Theory of Reflectance and Emittance Spectroscopy, second ed. Cambridge University Press.

Holler, B.J., Young, L.A., Grundy, W.M., Olkin, C.B., Cook, J.C., 2014. Evidence for longitudinal variability of ethane ice on the surface of Pluto. Icarus 243, 104–110.

Jolliffe, I.T., 1986. Principal Component Analysis. Springer-Verlag, p. 487. ISBN 978-0-387-95442-4.

Krasnopolsky, V.A., Cruikshank, D.P., 1999. Photochemistry of Pluto's atmosphere and ionosphere near perihelion. J. Geophys. Res. 104, 21979–21996.

Lara, L.M., Ip, W.-H., Rodrigo, R., 1997. Photochemical models of Pluto's atmosphere. Icarus 130, 16–35.
Lellouch, E., Merlin, F., de Bergh, C., 2014. The state of CO and the temperature of Triton's surface. EPSC Abstracts, 9 EPSC2014-44.
Licandro, J., Pinilla-Alonso, N., Pedani, M., Oliva, E., Tozzi, G.P., Grundy, W.M., 2006. The methane ice rich surface of large TNO 2005 FY9: a Pluto-twin in the transneptunian belt. Astron. Astrophys. 445, L35–L38.
Lorenzi, V., Pinilla-Alonso, N., Licandro, J., Cruikshank, D.P., Grundy, W.M., Binzel, R.P., Emery, J.P., 2016. The spectrum of Pluto, 0.40–0.93 μm. I. Secular and longitudinal distribution of ices and complex organics. Astron. Astrophys. 585, A131.
Madey, T.E., Johnson, R.E., Orlando, T.M., 2002. Far-out surface science: radiation induced surface processes in the Solar System. Surf. Sci. 500, 838–858.
Merlin, F., Alvarez-Candal, A., Delsanti, A., Fornasier, S., Barucci, M.A., DeMeo, F.E., de Bergh, C., Doressoundiram, A., Quirico, E., Schmitt, B., 2009. Stratification of Methane Ice on Eris' surface. Astron. J. 137, 315–328. doi:10.1088/0004-6256/137/1/315.
Merlin, F., Barucci, M.A., de Bergh, C., DeMeo, F.E., Alvarez-Candal, A., Dumas, C., Cruikshank, D.P., 2010. Chemical and physical properties of the variegated Pluto and Charon surfaces. Icarus 210, 930–943.
Merlin, F., 2015. New constraints on the surface of Pluto. Astron. Astrophys. 582, A39.
Moore, J.M., McKinnon, W.B., Spencer, J.R., et al., 2016. The geology of Pluto and Charon through the eyes of New Horizons. Science submitted.
Moore, M.H., Hudson, R.L., 2003. Infrared study of ion-irradiated N2-dominated ices relevant to Triton and Pluto: formation of HCN and HNC. Icarus 161, 486–500.
Olkin, C.B., Young, E.F., Young, L.A., Grundy, W., Schmitt, B., Tokunaga, A., Owen, T., Roush, T., Terada, H., 2007. Pluto's Spectrum from 1.0 to 4.2 μm: implications for surface properties. Astron. J. 133, 420–431. doi:10.1086/509616.
Owen, T.C., Roush, T.L., Cruikshank, D.P., Elliot, J.L., Young, L.A., de Bergh, C., Schmitt, B., Geballe, T.R., Brown, R.H., Bartholomew, M.J., 1993. Pluto: surface ices and atmospheric composition. Science 261, 745–748. doi:10.1126/science.261.5122.745.
Philippe, S., Schmitt, B., Grundy, W., Protopapa, S., Olkin, C., 2015. 12 years of Pluto surface's evolution investigated with radiative transfer modeling. Am. Astron. Soc. DPS meeting #47, BAAS #210.19.
Philippe, S., Schmitt, B, Beck, P., Brissaud, O., Appéré, Th., 2017. Experimental sublimation of CO2:H2O ice mixture as an analog to Martian seasonal deposits. Icarus to be submitted.
Prokhvatilov, A.I., Yantsevich, L.D., 1983. X-ray investigation of the equilibrium phase diagram of CH4-N2 solid mixtures. Sov. J. Low Temp. Phys. 9, 94–98.
Protopapa, S., Grundy, W.M., Tegler, S.C., Bergonio, J.M., 2015. Absorption coefficients of the methane-nitrogen binary ice system: implications for Pluto. Icarus 253, 179–188.
Protopapa, S., Grundy, W.M., Reuter, D.C., Hamilton, D., Dalle Ore, C.M., Cook, J.C., Cruikshank, D.P., Philippe, S., Quirico, E., Schmitt, B., Binzel, R.P., Earle, A.M., Ennico, K., Howett, C.J.A., Lunsford, A.W., Olkin, C.B., Parker, A., Singer, K.N., Stern, A., Weaver, H., Young, L.A.the New Horizons Science Team, 2017. Pluto's global surface composition through pixel-by-pixel Hapke modeling of New Horizons Ralph/LEISA data. Icarus Pluto special issue.
Quirico, E., Schmitt, B., Bini, R., Salvi, P.R., 1996. Spectroscopy of some ices of astrophysical interest: SO_2, N_2 and N_2:CH_4 mixtures. Planet. Space Sci. 44, 973–986. doi:10.1016/0032-0633(96)00006-2.
Quirico, E., Schmitt, B., 1997a. Near infrared spectroscopy of simple hydrocarbons and carbon oxides diluted in solid N_2 and as pure ices: implication for Triton and Pluto. Icarus 127, 354–378. doi:10.1006/icar.1996.5663.
Quirico, E., Schmitt, B., 1997b. A spectroscopic study of CO diluted in N_2 ice: applications for Triton and Pluto. Icarus 128, 181–188. doi:10.1006/icar.1997.5710.
Quirico, E., Douté, S., Schmitt, B., de Bergh, C., Cruikshank, D.P., Owen, T.C., Geballe, T.R., Roush, T.L., 1999. Composition, physical state and distribution of ices at the surface of Triton. Icarus 139, 159–178. doi:10.1006/icar.1999.6111.
Reuter, D., et al., 2008. Ralph: a Visible/Infrared Imager for the New Horizons Pluto/Kuiper Belt Mission. Space Sci. Rev. 140, 129–154.
Sasaki, T., Kanno, A., Ishiguro, M., Kinoshita, D., Nakamura, R., 2005. Search for non-methane hydrocarbons on Pluto. Astrophys. J. 618, L57–L60.
Spencer, J.R., et al., 1997. In: Stern, S.A., Tholen, D.J. (Eds.), Volatile Transport, Seasonal Cycles, and Atmospheric Dynamics on Pluto, in Pluto and Charon. Univ. of Arizona Press, pp. 435–473. 1997.
Stansberry, J.A., Spencer, J.R., Schmitt, B., Benchkoura, A., Yelle, R.V., Lunine, J.I., 1996. A model for the overabundance of methane in the atmospheres of Pluto and Triton. Planet. Space Sci. 44, 1051–1063. doi:10.1016/0032-0633(96)00084-0.
Stern, S.A., Weaver, H.A., Steffl, A.J., Mutchler, M.J., Merline, W.J., Buie, M.W., Young, E.F., Young, L.A., Spencer, J.R., 2006. A giant impact origin for Pluto's small moons and satellite multiplicity in the Kuiper belt. Nature 439, 946–948.
Stern, S.A., Bagenal, F., Ennico, K., et al., 2015. The Pluto system: initial results from its exploration by New Horizons. Science 350, 292 1-8.
Vetter, M., Jodl, H.-J., Brodyanski, A., 2007. From optical spectra to phase diagrams—the binary mixture N2 – CO. Low Temp. Phys. 33, 1052.